FINAL REPORT

Semi-Passive Oxidation-Based Approaches for Control of Large, Dilute Groundwater Plumes of Chlorinated Ethylenes

SERDP Project ER-1684

April 2014

Frank Schwartz
Eung Seok Lee
Utku Solpuker
Jared Hawkins
Zachary Cotter
Neha Gupta
Pamela Olson
The Ohio State University & Ohio University

Distribution Statement A
This document has been cleared for public release

SERDP
DOD ▪ EPA ▪ DOE

This report was prepared under contract to the Department of Defense Strategic Environmental Research and Development Program (SERDP). The publication of this report does not indicate endorsement by the Department of Defense, nor should the contents be construed as reflecting the official policy or position of the Department of Defense. Reference herein to any specific commercial product, process, or service by trade name, trademark, manufacturer, or otherwise, does not necessarily constitute or imply its endorsement, recommendation, or favoring by the Department of Defense.

REPORT DOCUMENTATION PAGE

Form Approved

OMB No. 0704-0188

Public reporting burden for this collection of information is estimated to average 1 hour per response, including the time for reviewing instructions, searching existing data sources, gathering and maintaining the data needed, and completing and reviewing this collection of information. Send comments regarding this burden estimate or any other aspect of this collection of information, including suggestions for reducing this burden to Department of Defense, Washington Headquarters Services, Directorate for Information Operations and Reports (0704-0188), 1215 Jefferson Davis Highway, Suite 1204, Arlington, VA 22202-4302. Respondents should be aware that notwithstanding any other provision of law, no person shall be subject to any penalty for failing to comply with a collection of information if it does not display a currently valid OMB control number.
PLEASE DO NOT RETURN YOUR FORM TO THE ABOVE ADDRESS.

1. REPORT DATE *(DD-MM-YYYY)* 20-10-2013	**2. REPORT TYPE**	**3. DATES COVERED** *(From - To)*
4. TITLE AND SUBTITLE Semi-Passive Oxidation-Based Approaches for Control of Large, Dilute Groundwater Plumes of Chlorinated Ethylenes		**5a. CONTRACT NUMBER** **5b. GRANT NUMBER** **5c. PROGRAM ELEMENT NUMBER**
6. AUTHOR(S) Frank W. Schwartz, Eung Seok Lee, Utku Solpuker, Jared Hawkins, Zachary Cotter, Neha Gupta and Pamela Olson		**5d. PROJECT NUMBER** ER-1684 **5e. TASK NUMBER** **5f. WORK UNIT NUMBER**
7. PERFORMING ORGANIZATION NAME(S) AND ADDRESS(ES) The Ohio State University, The School of Earth Sciences Ohio University, Geology Department		**8. PERFORMING ORGANIZATION REPORT**
9. SPONSORING / MONITORING AGENCY NAME(S) AND ADDRESS(ES) Strategic Environmental Research and Development Program 4800 Mark Center Drive Suite 17D08 Alexandria, VA 22350		**10. SPONSOR/MONITOR'S ACRONYM(S)** SERDP **11. SPONSOR/MONITOR'S REPORT NUMBER(S)**
12. DISTRIBUTION / AVAILABILITY STATEMENT		
13. SUPPLEMENTARY NOTES		
14. ABSTRACT		
15. SUBJECT TERMS		

16. SECURITY CLASSIFICATION OF:			**17. LIMITATION**	**18. NUMBER**	**19a. NAME OF RESPONSIBLE PERSON**
a. REPORT	**b. ABSTRACT**	**c. THIS PAGE**			**19b. TELEPHONE NUMBER** *(include area code)*

Standard Form 298 (Rev. 8-98)

Table of Contents

List of Acronyms 9
Keywords 9
Acknowledgements 9
1. Abstract 10
1.1. Objectives 10
1.2. Technical approach 10
1.3. Results 10
1.4. Benefits 12
2. Objectives 13
3. Background 15
4. Materials and Methods 17
4.1. Experimental and Theoretical Studies of Convective Mixing 17
4.1.1. Flow tank experiments 17
4.1.2. Mathematical modeling 20
4.2. Permanganate gel (PG) for groundwater remediation: Compatibility, gelation, and release characteristics 22
4.2.1. Materials 22
4.2.2. Sample preparation 23
4.2.3. Flow-through tests 24
4.3. Harnessing the complex behavior of ultra-dense and viscous treatment fluids as a strategy for aquifer remediation 24
4.3.1. Validation modeling 24
4.3.2. Flow tank experiments 25
4.3.2.1. Dense/viscous fluids 25
4.3.2.2. Time-delayed gelling 25
4.3.3. Diffusion coefficient measurements 26
4.4. Development and characterization of slow-release permanganate gel (SRP-G) for groundwater remediation 27
4.4.1. Materials 27
4.4.2. Sample preparation 28

4.4.3. Flow-through tests 28
4.5. Description and verification of a novel flow and transport model for silicate-gel emplacement 29
4.5.1. Materials and experimental setup 29
4.5.2. Numerical methods 31
4.5.3. Numerical modeling 34
4.6. Geopolymers as slow-release materials for potassium permanganate 37
4.6.1. Materials 37
4.6.2. Sample preparation 38
4.6.3. 1-D column experiment 38
4.6.4. X-ray Diffraction (XRD) and Scanning Electron Microscopy (SEM) Imaging 39
5. Results and Discussion 40
5.1. Experimental and theoretical studies of convective mixing 40
5.1.1. Results and discussion 40
5.2. Permanganate gel (PG) for groundwater remediation: Compatibility, gelation, and release characteristics 44
5.2.1. Compatibility and gelation tests 44
5.2.1.1. Chitosan gel 44
5.2.1.2. Aluminosilicate gel 45
5.2.1.3. Silicate gel 47
5.2.1.4. Colloidal silica gel 49
5.2.2. Release tests 49
5.3. Harnessing the complex behavior of ultra-dense and viscous treatment fluids as a strategy for aquifer remediation 51
5.3.1. Results and Discussion 51
5.3.1.1. Saline solutions 51
5.3.1.2. Dense/viscous fluids 52
5.3.1.3. Time-delayed gelling 54
5.3.1.3.1. Small flow tank experiments 54
5.3.1.3.2. Large flow tank experiments 55
5.3.1.4. Permanganate release from silicate gels by diffusion 56

5.4. Development and characterization of slow-release permanganate gel (SRP-G) for groundwater remediation 58
5.4.1. Results and discussion 58
5.4.1.1. Gelation and release characteristics of SRP-G in water 58
5.4.1.2. Gelation and release characteristics of SRP-G in porous media 60
5.5. Description and verification of a novel flow and transport model for silicate-gel emplacement 65
5.5.1. Results 65
5.5.2. Discussion 68
5.6. Geopolymers as slow-release materials for potassium permanganate 69
5.6.1. Results 69
5.6.1.1. XRD analysis 69
5.6.1.2. 1-D column experiment 70
5.6.1.3. SEM imaging 71
5.6.2. Discussion 74
6. Conclusions and implications for future research 81
6.1. Conclusions 81
6.2. Implications for future research 82
7. Literature Cited 84
Appendix A Supporting data 91
Appendix B Publications 92

List of Tables

Table 1. Parameters used in the numerical simulations. 18
Table 2. Parameters used in the simulations; • acquired through experimental measurement, or * determined through model calibration. 36
Table 3. Simulation specific parameters; • acquired through experimental measurement, or * deducted from experimental observation. 36
Table 4. Parameters used in viscosity calculation (all unitless); • deducted from experimental observation, or * determined through model calibration. 36
Table 5. Chemical composition (wt %) and physical characteristics of metakaolin used in geopolymers (Advanced cement technologies, 2013). 38
Table 6. Nominal molar ratio compositions of the geopolymer samples. 38
Table 7. The gelation characteristics of SRP-Gs in porous media. 60

List of Figures

Figure 1. Schematic of the experimental flow tank system. Water was pumped into the inflow chamber through quick-disconnect fittings. The tracer solution was pumped into the sand tank through the sampling ports indicated by the star. 17
Figure 2. Schematic diagram showing the layered medium of the first experiment (a) and the lenticular medium of the second experiment (b). 19
Figure 3. Conceptual models for the MITSU3D simulations of the experiments (grid size of 1x1 cm). (a) the layered medium of the first experiment, (b) the lenticular medium of the second experiment, (c) boundary conditions utilized in the MITSU3D simulations. 22
Figure 4. Lenticular media used by Schincariol and Schwartz (1990) for the flow-tank experiments where the dotted box indicates location of dense fluid injection (a), simulation domain (119x72) (b) and boundary conditions (c) used in MITSU3D simulations. 25
Figure 5. Permanganate release apparatus. 27
Figure 6. Photo showing the column setup and release of MnO_4^- from the gelated CRP-G cylinder in the glass column. 28
Figure 7. Two exemplary parameter combinations for viscosity increase factor f with $e = 1$; grey lines: $\lambda = 5.8 \cdot 10 - 3s - 1$, $\beta_S = 50$, $\beta_{\max} = 1000$; black lines: $\lambda = 2.9 \cdot 10 - 3s - 1$, $\beta_S = 5$, $\beta_{\max} = 750$..... 34
Figure 8. Exemplary parameter combination for reduction factor e; black lines: $\omega 1, \mu \max = 1$, grey lines: $\omega 1, \mu \max = 0.5$..... 34
Figure 9. Conceptual model, initial and boundary conditions. 35
Figure 10. Concentration distribution map experiment-1 (a) day 2, (b) day 4 and (c) day 11. 41
Figure 11. Flow tank experiment with discontinuous high and low hydraulic conductivity lenses. 10,000 mg/L NaCl and 300 mg/L RWT tracer solution was used. (a) Day 2.5, (b) day 8.5 and (c) day 17. 42
Figure 12. MITSU3D modeling results of the experiment 1. (a) Day 2, (b) day 4, (c) day 11. ... 43
Figure 13. MITSU3D modeling results of the experiment-1. (a) Day 2.5, (b) day 8.5, (c) day 17. 44
Figure 14. Permanganate concentrations in chitosan gels. 45
Figure 15. Permanganate concentrations in aluminosilicate gels. 46
Figure 16. Photo showing $KMnO_4$ solutions in aluminosilicate gel. 47
Figure 17. Permanganate concentrations in Kasil 6 silicate gel and colloidal silica gel. 47
Figure 18. Viscosities of (a) Kasil 1 silicate gel with addition of granular $KMnO_4$ and (b) Kasil 6 silicate gel and Ru Na silicate gel with addition of 60 g L^{-1} $KMnO_4$ solution: volume ratios (%) of $KMnO_4$ solution in the total volume of solution (silicate gel + $KMnO_4$ solution)..... 48
Figure 19. Viscosities of colloidal silica with addition of granular $KMnO_4$. 3.75 g, 4 g, and 7.5 g of $KMnO_4$ granules were added to 150 mL of colloidal silica, respectively. 49
Figure 20. Temporal changes in MnO_4^- concentrations in the effluent samples of the glass column containing (a) silicate-based PG gel and (b) colloidal silica-based PG gel. 50

Figure 21. Photo showing the remaining colloidal silica matrix (left column) after MnO_4^- is released. 51
Figure 22. Experimental results (a) with simulation results (b) for 10 g/L after 2 days. Plume concentrations below 0.5 g/L were not plotted for the experimental or the simulated plumes. ... 52
Figure 23. Comparison of dense, viscous fluid experimental (a) and simulated (b) plumes, after 8 hours. Plume concentrations below 60 g/L are not shown for either experimental or simulated plumes. i and ii represent hydraulic conductivities of $1.6 \cdot 10^{-4}$ and $2.9 \cdot 10^{-3}$ m/sec, respectively. 53
Figure 24. Concentration maps for the time-delayed gelling experiments representing the RWT concentrations. The image analyses procedure of McNeil et al. (2006) was followed. (a) Immediately after injection of the solution into 3 cm thick high conductivity layer, (b) 20 days after the injection. i, ii and iii represent hydraulic conductivities $1.6 \cdot 10^{-4}$, $2.9 \cdot 10^{-3}$ and $5.0 \cdot 10^{-5}$ m/sec, respectively. 54
Figure 25. The release of the $KMnO_4$ bearing solution from the gelled silicate solution. (a) 1.5 hour after the injection of the gelling solution over the clay lens, (b) 2 days after the injection, (c) 13 days after the injection, (d) 31 days after the injection. Darker tones (high conductivity media), lighter tones (low conductivity media). 55
Figure 26. The release patterns of RWt dye from the gelled solutions. (a) Right after the injection of 8 L of solution, (b) 3 days after the injection, (c) 11 days after the injection, (d) 38 days after the injection. Dark tones (high conductivity material), light tones (low conductivity material).. 56
Figure 27. Permanganate release from silicate hydrogels with 50 wt % silicate solution. 57
Figure 28. Effects of $KMnO_4$ concentrations upon gelation lag times. 58
Figure 29. Temporal changes in release rates of SRP-G with (a) 9 g L^{-1} (b) 16 g L^{-1} (c) 20 g L^{-1} $KMnO_4$. 59
Figure 30. Column tests with porous media in which (a) gelation did not occur, showing absence of remaining gel at conclusion of first-order mass flux phase, (b) gelation occurred, showing gel present at conclusion of first-order mass flux phase. The glass column was rotated to show SRP-G accumulated at the bottom of the sandy media. 61
Figure 31. Mass flux and cumulative release from gelated SRP-G with (a) 20.0 g L^{-1} (b) 21.8 g L^{-1} (c) 22.5 g L^{-} (d) 22.9 g L^{-1} (e) 23.0 g L^{-1} (f) 25.0 g L^{-1} $KMnO_4$. 62
Figure 32. Photos showing dynamics of SRP-G (22.5 g L^{-1} $KMnO_4$) that did not gelate within the glass column. (A) Immediately after injection, (B) 1.5 h after injection, (C) 24 h after injection, (D) 24 h after injection (column was rotated to show the bottom of the sandy media, (E) 33 h after injection (bottom view), and (F) 48 h after injection (bottom view). 63
Figure 33. Photos showing dynamics of SRP-G (25 g L^{-1} $KMnO_4$) that gelated within the glass column. (A) Immediately after injection, (B) 1 h after injection, (C) 31 h after injection, (D) 51 h after injection (bottom view), and (E) 72 h injection (bottom view). 63
Figure 34. Conceptual model of SRP-G scheme. Note that SRP-G gels are formed upon impermeable layer, release permanganate to over-riding groundwater flow. 64

Figure 35. The temporal evolution of the gelation of silicate solutions. The first, second and third experiments are shown in (a), (b) and (c), respectively. 66
Figure 36. Results of numerical simulation for experimental setups 1 (a), 2 (b), and 3 (c); 67
Figure 37. Detailed section at the boundary of the gelated solute for experiment 1 at time $t = 9\ min$, isolines are mass fraction 1 $\omega 1$, shading is viscosity μ, arrows are velocity vectors. 68
Figure 38. The XRD patterns of the blank (a) and $KMnO_4$ doped (b) geopolymer powders..... 70
Figure 39. Temporal variations in the MnO_4^- concentrations in the column outflow and the measured amount of release MnO_4^-. 71
Figure 40. SEM images (back-scattered electron image) of $KMnO_4$ doped geopolymer samples. (a),(b) Sample 1; (c), (d) sample 2; (e), (f) sample 3. (a), (c) and (e) show low magnification images relative to (b), (d) and (f). 72
Figure 41. SEM images (large-field detector image) of $KMnO_4$ doped geopolymer samples. (a),(b) Sample 1; (c), (d) sample 2; (e), (f) sample 3. (a), (c) and (e) show low magnification images relative to (b), (d) and (f). 73
Figure 42. The first 60% of the fractional release of $KMnO_4$ from geopolymers (solid black curves). Dashed gray curves represent the best fit for data calculated by the nonlinear least squares method. (a), (b) and (c) represent the first, second and third sample, respectively. 75
Figure 43. The first 60% of the fractional release of $KMnO_4$ from the geopolymers (solid black curves). Dashed gray curves represent the best fit for data using equation 2 calculated by the nonlinear least squares method. (a), (b) and (c) represent the first, second and third sample, respectively. Dotted curves represent the 95% confidence intervals..... 77
Figure 44. The first 60% of the fractional release of $KMnO_4$ from the geopolymers (solid black curves). Dotted lines and dashed curves represent the dissolution-related, fast transport and Fickian diffusion processes, respectively using the $k1$ and $k2$values in Figure 43. (a), (b) and (c) represent the first, second and third sample, respectively. 79

List of Acronyms

CRP	Contol-Release Permanganate
DCE	Dichloroethylene
DNAPL	Dense Non-Aqueous Phase Liquid
DoD	Department of Defense
EDS	Energy Dispersive Spectroscopy
FE	Finite Element
ISCO	In-Situ Chemical Oxidation
PCE	Perchloroethylene
PG	Permanganate Gel
PDG	Potassium Permanganate Doped Geopolymer
RWT	Rhodamine Keyacid
RO	Reverse Osmosis
SEM	Scanning Electron Microscope
SRP-G	Slow Release Permanganate Gel
TCE	Trichloroethylene
THMC	Thermal, Hydraulic, Mechanical and Chemical
US DHHS	United States Department of Human and Health Services
UV-VIS	Ultraviolet-Visible
XRD	X-Ray Diffraction

Keywords

Slow-release solids, variable density flow, in-situ oxidation, time-delayed gelling, $KMnO_4$, numerical modeling

Acknowledgements

This research was supported by the Strategic Environmental Research and Development Program (SERDP) under project ER-1684.

1. Abstract

1.1. Objectives

Chlorinated solvents can pose a considerable risk to human health and their presence in groundwater at many DoD sites is a significant problem due to the persistence of these chemicals in the environment. Moreover, plumes of dissolved chlorinated solvents in groundwater may not be efficiently treated in a cost effective manner due to their size, location and in some cases low contaminant concentration. Many studies have studied the possibilities of breaking down chlorinated solvents by chemical oxidation using $KMnO_4$. Yet, the full potential of such oxidation-based approaches has not been realized, especially for those hard to treat plumes just mentioned. This project seeks cost effective ways to utilize in-situ oxidation approach to remediate relatively dilute plumes of chlorinated solvents (e.g., DCE, PCE, TCE) and contaminants in deeper or lower permeability zones relative to more conventional techniques and approaches. In order to reach this goal a number of key research questions were addressed:

1. Can hypersaline $KMnO_4$ fluids effectively invade a heterogeneous medium because of density effects and remain sequestered hydrodynamically?
2. Is it possible to take advantage of time-delayed gelling property of $KMnO_4$ doped engineered solutions to develop solids in-situ capable of slow KMnO4 release?
3. How can we predict the fate of these engineered solutions in groundwater?
4. Are there alternative cost effective materials suitable for use as slow-release solids in reactive barriers?

1.2. Technical approach

The flow of hypersaline and/or viscous solutions in aquifers and time delayed in-situ gelling materials were studied using both flow tank experiments and numerical modeling. In the flow tank experiments, different arrangements of glass beads were used to explore the mixing and flow behavior of concentrated NaCl solutions and Na-silicate solutions. A variable density flow code Mitsu3D was used to simulate the flow tank experiments and to increase the predictability of the flow patterns of saline and viscous solutions. Furthermore, engineered Na-silicate and colloidal silica solutions were used in flow tank experiments and column experiments to demonstrate the potential of using the in-situ time-delayed gelling property of such solutions. A numerical model was developed to simulate the variable density flow/gelation behavior of the Na-silicate solutions.

A variety of materials were tested in column experiments to find a cost effective alternative host material that can be used to support the slow release of $KMnO_4$ in reactive barriers. In particular, slow-release behavior of geopolymers was studied through1-D column experiments.

1.3. Results

One way of utilizing the in-situ oxidation scheme is to inject concentrated treatment fluids into the zone of chlorinated solvents in groundwater. Our initial studies tested if hypersaline solutions mimicking concentrated treatment solutions can invade the heterogeneous medium effectively. Specifically, we explored the mixing and flow behavior of concentrated NaCl solutions (10 g/L) in flow tank experiments using different arrangements of glass beads. The first experiment with

continuous high and low permeability layers showed that some portion of the saline solution flowed away along high permeability layers. Such fast pathways reduce the effectiveness of the delivery of the treatment solutions into the contaminated zone. The other disadvantage of this arrangement was that once injected, highly concentrated solutions sank rapidly to the bottom of the tank without much downward resistance to flow. In the second flow tank experiment, the presence of discontinuous lenses promoted the formation of instabilities to enhance mixing, and slowed down the migration of the tracer plume, thereby increasing the residence time between the potential treatment chemical and the contaminant plume. Another advantage was that solutes that were in contact with clay lens, diffused into the lens and created a slow release system.

The use of controlled-release reactive barriers is another method in the in-situ oxidation scheme. Creating such reactive barriers in-situ requires time-delayed gelling of potential $KMnO_4$ doped solutions. We investigated the possibility of creating a MnO_4^- gel solution by testing compatibility and reactivity of gels, such as chitosan, aluminosilicate, silicate and colloidal silica gels, with MnO_4^-. We specifically focused on studies of the gelation and MnO_4^- release characteristics of two promising gels, i.e., silicate and colloidal-silica gels. Our approach involved a series of batch and flow-through column experiments. Due to their organic character, chitosan gels were found to be incompatible with MnO_4^-. The aluminosilicate gel was also unsatisfactory because it was not miscible with $KMnO_4$ solution. Silicate gels derived from silicate solutions are compatible with MnO_4^- and the viscosity of the resulting silicate gel could be manipulated by the addition of saline MnO_4^- solution or the addition of salts. Colloidal silica contains nanoparticles of amorphous silicon dioxide and sodium hydroxide suspended in water solution. Colloidal silica solutions are chemically also non-reactive with MnO_4^-. The results of gelation batch tests further demonstrated the delayed gelling characteristics of colloidal silica. The gelation lag times of colloidal silica increased as $KMnO_4$ concentrations decreased. In porous media, MnO_4^- release from the gelated SRP-G yielded a similar pattern to that of open water tests, i.e., a rapid initial peak release followed by exponential decay and an asymptotic release phase. The SRP-G solutions that gelated within columns exhibited characteristic transport and release patterns indicating the effects of diffusion in addition to advection and dispersion.

Dense, viscous and oxidant resistant Na-silicate solutions may be used to deliver $KMnO_4$ to the deep contaminated zones of the aquifers. It was assumed that the density difference between the groundwater and silicate solutions would cause the sinking of silicate solutions without significant horizontal spread of the silicate solution. However, through time the density difference would decrease due to mixing. Using such dense and viscous solutions Na-silicate solution (N-Clear) containing $KMnO_4$ could be injected into coarse-grained, high conductivity units but the delivery of this solution had limitations due to its high viscosity. The silicate solutions sank slowly and the concentrations of the viscous solutions decreased significantly over relatively short distances due to the dilution of the solution by mixing. We modelled the experiments involving the viscous solution using MITSU3D. Modelling of the dense viscous fluid was successful in reproducing the shape of experimental plumes, especially at later times. The successful results of these experiments suggest that silicate solutions can be useful in delivering oxidants to the deeper zones of contaminated aquifers.

Time dependent gelling property of silicate solutions can be used to create controlled-release reactive barriers in-situ. Silicate solutions are stable at high pHs (i.e. pH > 11) but once the pH of the solution is lowered, the solubility of the silica is reduced and it polymerizes. The results of

flow tank experiment illustrate the potential of this approach. We prepared a solution by mixing diluted sodium silicate solution (N-clear) with sodium bicarbonate solution that transforms into a soluble silicate gel through time. The initial viscosity of such a mixture is low and the gelation is not immediate (i.e. several hours). These conditions are useful for initial injection of this solution into the targeted layer in the flow tank experiment. The high conductivity layer was flooded with this solution. After 20 days, less than 60% of the initial tracer concentration remained in the gelled silicate material.

Numerical models required to predict the fate of the solutions that have the time-delayed gelation property should simulate the increase in the viscosity depending on the concentration of the silicate solution. The results of the numerical modelling to simulate the time delayed gelling of silica solutions showed that the simulated behavior of the solution resembles the general features of the laboratory experiments. The calculated gelation times of the solutions closely match the observed gelation times. The numerical model captures not only the concentration profiles but also the shape of the sinking silicate plumes reasonably well. Experiments showed that gelation takes place only at zones with relatively higher solute concentrations. The numerical model generated a concentration profile similar to experiments.

Finally, novel cost effective controlled-release geopolymers were investigated to be used as reactive barriers. The MnO_4^- release experiments from $KMnO_4$ doped geopolymer samples showed that permanganate concentrations were initially high due to high solubility of the $KMnO_4$, but then gradually decreased to lower concentrations. It took about 19 days for samples with higher $KMnO_4$ concentrations to get exhausted. Based on the fractional release data from the column experiments, the anomalous diffusion is the mechanism controlling the $KMnO_4$ diffusion from the geopolymers.

1.4. Benefits

In this project, novel cost effective ways to utilize in-situ oxidation approach were investigated as a potential new strategy for remediating relatively dilute plumes of chlorinated solvents and contaminants in deeper or lower permeability zones. This knowledge gathered through this project improved our understanding of different aspects of in-situ oxidation approach such as flow and mixing behavior of saline solutions in fresh water. Furthermore, Na-silicate or colloidal silica solutions were amenable to engineering providing for time delayed gelation. This concept will allow MnO_4^- doped silicate solutions to be injected and to spread over relatively large areas and act as slow-release solids following their gelation. In addition, the numerical method developed to predict the fate of these complex gelling solutions can also be used in other engineering applications. Finally, geopolymers were utilized as alternative cost effective slow-release solids since they are inert for chemical oxidation by $KMnO_4$.

2. Objectives

This project is motivated by the continuing need to remediate chlorinated solvents in groundwater, which are found at many DoD sites. Moreover, some plumes by virtue of their size, location and low contaminant concentrations may not be amenable for active treatment in a cost effective manner. The overarching goal of this project is to develop cost effective techniques to remediate relatively dilute plumes of chlorinated solvents (e.g., PCE, TCE), occurring at depths beyond the practical limits of more conventional techniques and approaches (i.e. >50 feet) to treat contaminants in lower permeability zones.

The basic study concept involves developing different ways for treatment chemicals, like $KMnO_4$, to be retained in a permeable reactive barrier to control further migration of a dilute plume. One approach is to take advantage of the tendency for dense plumes to mix and be mobile in heterogeneous settings. Because of density differences, a dense fluid will be localized in the vicinity of the injection wells without wholesale displacement of the contaminated fluid – effectively the $KMnO_4$ will tend to be localized in pools and low permeability units. Although there is some knowledge of variable density flow in ground water, not much is known about the behavior of hypersaline fluids in fresh ground water and how to take advantage of them. These questions of hypersaline flow behaviors and the persistence of $KMnO_4$ as a slow-release source motivate the first objective.

A second approach involves the slow-release of treatment fluids through time through the creation of slow-release solids in-situ. Such an approach is aimed at controlling the spread of dissolved chlorinated solvents at low concentrations away from potential sources. With this approach, we examine a novel approach for installing, semi-passive reactive barrier systems using wells for emplacement of the $KMnO_4$. It has great potential for application to contamination in deep aquifers. This approach has built on a variety of our previous studies; including advanced oxidation approaches for treating plumes of chlorinated solvents and basic theories of variable-density flow.

The objectives of this project are (1) to understand how hypersaline $KMnO_4$ fluids invade a heterogeneous porous medium and remain in place because of density effects, (2) to examine the possibilities and remedial advantages for creating slow-release solids in-situ, (3) to describe and demonstrate an approach for modeling this variable density flow/gelation problem and (4) to find alternative materials to provide slow release behaviors in the subsurface to create a passive reactive barrier controlling the migration of a ground water plume.

The working hypotheses that support these objectives are:

(1) "A dense fluid will be localized in the vicinity of the injection wells without wholesale displacement of the contaminated fluid – effectively the $KMnO_4$ will tend to be localized in pools and low permeability units."
(2) "The slow-release gels are created in-situ by using the time-delayed gelling property of $KMnO_4$ doped silicate solutions."
(3) "The gelation process can be simulated by defining a "solute 1" with concentration ω_1, which is used to calculate the fluid density and an auxiliary "solute 2" with concentration ω_2 which has no influence on fluid density and experiences a 1st order decay process."
(4) "The slow-release solids are created by embedding $KMnO_4$ in gepolymers which are slowly released by diffusion into the ambient flow."

This study has explored the efficacy of these approaches using a combination of laboratory and flow-tank experiments and numerical modeling. The laboratory and flow tank experiments provided a physically based understanding of processes involved and a basis for calibrating the modeling approach. Numerical models were not only used to enhance the understanding of the underlying key flow and mass transport processes but also the interactions of those processes and the key parameters controlling them. These science innovations combine to create the efficiency in treating deep plumes by (i) using a relatively small number of wells, (ii) taking advantage of the density under-ride to broadly distribute, small, less costly quantities of $KMnO_4$, (iii) producing low cost slow-release solids (iv) reducing treatment costs by sequestering $KMnO_4$ from natural oxidation processes and (v) providing localized opportunities for localized partitioning and sorption of the contaminants.

3. Background

Chlorinated solvents such as DCE, PCE and TCE are currently considered to be the most prevalent organic contaminants in groundwater (Baird and Cann, 2008). They are found at 861 National Priority List hazardous waste sites in the United States. (US DHHS, 1997). In the subsurface, these dense non-aqueous phase liquids (DNAPLs) tend to sink downward through a porous medium to form thick residual DNAPL or DNAPL pools, which can remain in place for hundreds of years under natural conditions. Thus, they are providing long-term sources of direct and indirect contamination (US EPA, 1987; Zhang and Schwartz, 2000; Aulenta et al., 2007; Baird and Cann, 2008). DNAPLs can yield large, dilute (<0.1 mg/L) plumes that can extend for thousands of meters down gradient from a source (Schwartz and Zhang, 2003).

There is a continuing need to remediate relatively dilute plumes of chlorinated solvents in groundwater which are found at many DoD sites. The remediation of large and dilute contaminated plumes occurring at depths and contaminants in lower permeability zones is difficult to address. Some plumes by virtue of their size and low contaminant concentrations may not be actively treated in a cost effective manner. Beyond the well-known problems of mass-removal efficiency associated with a traditional remediation technology, like pump and treat, (Schnarr et al., 1998; McDade et al., 2005), serious limitations also exist with more modern methods like zero-valent iron walls.

As a powerful oxidant (E^o = 1.68 V) $KMnO_4$ works by breaking down various organic contaminants through short-lived intermediates to CO_2, water, Cl^-, and a solid, MnO_2. The reaction stoichiometry, pathways, and reaction kinetics are well understood (Yan and Schwartz, 1999; Siegrist et al., 2001). Numerous studies have reported that chemical oxidation of chlorinated ethylenes in aqueous solution is rapid (e.g. Yan and Schwartz, 1998; Huang et al., 1999; Schnarr et al., 1998; Urynowicz, 2000). In the last 20 years, $KMnO_4$ has been widely used as a strong oxidant for the in situ remediation of sites contaminated by dissolved chlorinated ethylene (Stewart, 1965; Schnarr et al., 1998; Yan and Schwartz, 1999, 2000; Zhang and Schwartz, 2000; Huang et al., 2001; Kao et al., 2008). Specifically, flushing DNAPL sources with highly concentrated $KMnO_4$ solution has received significant attention since 1990s (e.g., Siegrist et al., 2001). For the source-zone flushing schemes involving permanganate (MnO_4^-), it is necessary to deliver adequate amount of the treatment chemicals through the DNAPL source zone.

In-situ oxidation of dissolved chlorinated ethylenes can be done either by injecting dense concentrated permanganate water into target zones or emplacing controlled-release $KMnO_4$ (CRP) reactive barriers in the pathways of contaminated plumes. The former method works when solvent plumes are dilute and aquifer is made up of permeable units. Aquifer heterogeneity and low permeable zones can cause problems in the delivery of oxidants into the target zone. Based on simulations, Ibaraki and Schwartz (2001) showed that high permeability pathways act as hydraulic short circuits and expedite the flow of treatment fluids from the injection to the withdrawal wells. This short circuiting and density under-riding can be problematic, with both acting to reduce flushing efficiency. Furthermore, high oxidant loading and/or reductant levels can lead to the precipitation of MnO_2(s) and reduce the hydraulic conductivity of the media in the treatment zone (Lee et al., 2003; Li and Schwartz, 2004). The latter approach use controlled-release solids developed by mixing potassium permanganate with other matrix materials such as

clay-rich slurry (Siegrist et al., 1999), oxidation resistant waxy polymers (Ross et al., 2005) and resin (Lee and Schwartz, 2007a, b; Lee et al., 2008a, b). Functionally, various MnO_4^- reactive barrier systems can be created by injecting clay-rich slurry into the horizontal hydraulic fractures and vertical trenches or boreholes (Murdoch et al., 1997) or by installing the CRP slurries or pellets, i.e., the cylindrical solid mixtures of $KMnO_4$ granules and paraffin wax or resin, in rows of vertical boreholes across the downstream nose of a plume (Lee and Schwartz, 2007a). The $KMnO_4$ granules in these solids slowly dissolve into groundwater and released at a controlled rate into the ambient groundwater flow to affect the in-situ destruction of organic contaminants. These systems also have constraints on the lifetime, installation depths and frequency (Lee et al, 2008b). While the efficacy of CRP scheme has been verified through a series of column and flow-tank studies of variable scales (Lee and Schwartz, 2007a, b; Lee et al., 2008a, b) and a field application (Christensen et al., 2012), some studies also suggested that facilitating lateral spreading of MnO_4^- would be needed to further enhance the efficiency of the CRP scheme (Lee et al. 2008a, b). For example, when 10 CRP injection wells are emplaced to cover an 8 m wide TCE plume, 10 discrete and narrow zones of MnO_4^- would develop in the direction of groundwater flow, exemplifying the mixing inefficiency in the well-based CRP system (Lee et al., 2008b). Such slow-release systems have constraints on their lifetime, installation depths and spacings.

Our study involves two quite different approaches to deliver oxidants to zones of contamination. The first approach is to use $KMnO_4$ mixed with dense saline water to move and sequester the oxidant, effectively elucidate possibilities of hydraulic containment and slow release. A second approach is to mix $KMnO_4$ with ultra-dense silicate solutions providing slow release through the same physical mechanisms. These methods target dilute deep contaminated plumes and involve MnO_4^- compatible silicate solutions sink deeper parts of a permeable aquifer where conventional methods cannot reach and oxidant rich solutions cannot be hijacked through high permeability pathways during transport. Moreover, vertical flow of the dense fluid will enable MnO_4^- to penetrate less permeable units, which sometimes sequester contaminants from the more active portions of the flow system. Localized reservoirs of $KMnO_4$ sequestered in pools and low permeability lenses would resist advection in the ambient flow and slowly release oxidants in the zone of reaction. To our knowledge, neither of these proposed mechanisms has been studied previously. In addition, time delayed-gelation of $KMnO_4$ doped silicate solutions was also suggested as an alternative approach for slow release mechanisms. In this method, concentrated MnO_4^- solution that sinks through the porous media, slowly gels as it spreads away from the injection wells to form solid MnO_4^- gel, and slowly releases MnO_4^- to groundwater over an extended time periods time. Injection of such a slow-release MnO_4^- gel solution may provide a more cost-effective in situ treatment option for large, dilute, or deep plumes of DNAPL in groundwater because it may facilitate lateral spreading of oxidant, provide controlled level of oxidant within the target area over extended period of time, and reduce costs for well installation and operation.

4. Materials and Methods

4.1. Experimental and Theoretical Studies of Convective Mixing

When a hypersaline solution of $KMnO_4$ is injected at extremely high concentrations at strategic points within a contaminated aquifer using wells, the dense $KMnO_4$ fluid will spread away from the injection wells without wholesale displacement of the contaminated fluid. Effectively, the $KMnO_4$ will under-ride the less saline ground water. Localized reservoirs of $KMnO_4$ sequestered in pools and low permeability lenses would slowly release oxidants in the zone of reaction. The resulting dense pools of $KMnO_4$ should resist advection in the ambient flow. Moreover, the dense fluid would tend to move vertically and cause $KMnO_4$ to penetrate less permeable layers, which often sequester contaminants from the more active portions of the flow system. The premise of this approach is to create efficiency in treating deep plumes by (i) using a relatively small number of wells, and (ii) taking advantage of the density under-ride to broadly distribute, small, less costly quantities of $KMnO_4$. We explored the efficacy of this approach using a combination of flow-tank experiments and computer simulations.

4.1.1. Flow tank experiments

Proof-of-concept experiments were conducted in a flow tank that is 61.0 cm high, 182.9 cm long and 10.2 cm wide (Figure 1). The tank is constructed of 2.5 cm thick clear plexiglass. Injection and withdrawal chambers are located on the left and right side of the tank, respectively. The injection chamber contained 28 separate injection ports to maintain an even distribution of flow into the chamber. Porous stainless steel plates were placed and sealed with silicone caulking along their edges to keep glass beads out of the injection and withdrawal chambers. Various arrangements of the porous media were created from uniform spherical Ballotini industrial glass beads (Potters Industries Inc.) consisting of three different mil sizes from finest to coarsest, Mil-13, Mil-10, and Mil-3 with respective sieve sizes of 170-325 mesh, 100-170 mesh and 20-30 mesh, respectively. Each layer or lens contained one size of glass beads. Table 1 summarizes the hydraulic conductivity values for each mesh size. Additionally, a bentonite-glass beads mixture is used to create very low permeability lenses. 4 % bentonite (Tremco Inc., Ohio), powdered to a sieve size of 230, is added to Mil-13 size glass beads to lower its hydraulic conductivity by about 100 times (Abichou et al., 2002).

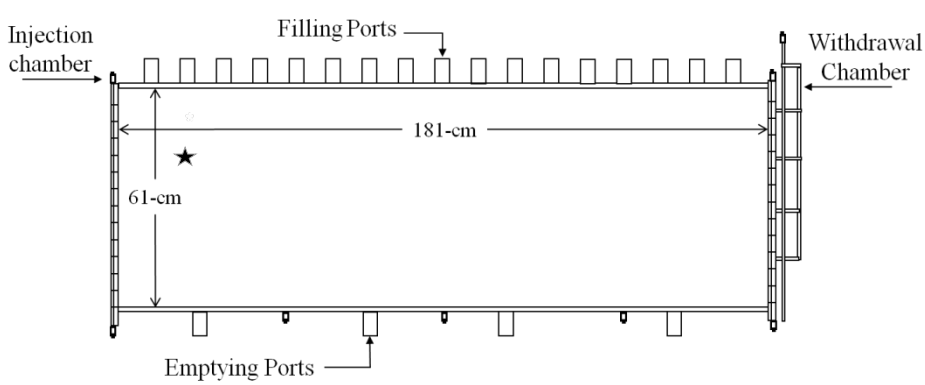

Figure 1. Schematic of the experimental flow tank system. Water was pumped into the inflow chamber through quick-disconnect fittings. The tracer solution was pumped into the sand tank through the sampling ports indicated by the star.

Table 1. Parameters used in the numerical simulations.

Parameter	Value
Hydraulic Conductivity†	
Mil-3	$3.00 \cdot 10^{-1}$ cm/s
Mil-5	$5.60 \cdot 10^{-2}$ cm/s
Mil-7	$2.20 \cdot 10^{-2}$ cm/s
Mil-10	$1.20 \cdot 10^{-2}$ cm/s
Mil-13	$1.90 \cdot 10^{-3}$ cm/s
Porosity	0.38
Free-solution diffusion coefficient	$1.61 \cdot 10^{-9}$ m^2/s
Average linear velocity	$3.00 \cdot 10^{-6}$ m/s
Longitudinal dispersivity	$1.00 \cdot 10^{-3}$ m
Transverse dispersivity	$2.00 \cdot 10^{-4}$ m
Initial concentration	0 g/L
Viscosity	
Water	$1.002 \cdot 10^{-3}$ Pa.s
2 g/L NaCl solution	$1.006 \cdot 10^{-3}$ Pa.s
5 g/L NaCl solution	$1.011 \cdot 10^{-3}$ Pa.s
10g/L NaCl solution	$1.015 \cdot 10^{-3}$ Pa.s
Density	
Water	0.9982 g cm^{-3}
2 g/L NaCl solution	0.9996 g cm^{-3}
5 g/L NaCl solution	1.0018 g cm^{-3}
10 g/L NaCl solution	1.0054 g cm^{-3}

† Schincariol and Schwartz (1990)

The first experiment aimed at studying the flow of dense tracer through horizontally layered media contained less dense pore water. The second experiment explored the mixing and flow behaviors of dense fluids in a lenticular medium and the possibilities of sequestering dense fluids within the system. The first experiment with the flow tank comprised seven horizontal layers (Figure 2a). The first layer (bottom layer) of beads was a 2.5 cm thick and contained Mil-10 beads. The second layer consisted of a 6.4 cm thick layer of Mil-3 beads, which was overlain by a 2.5 cm third layer of Mil-10 beads. On top of this layer, a 5.1 cm thick fourth layer of Mil-13 beads was placed. This layer was overlain by a 33 cm thick fifth layer of Mil-10 beads, followed by a 6.4 cm thick sixth layer of Mil-3 beads. A 2.5 cm thick seventh layer of Mil-10 beads was placed at the top. Each layer of sand was leveled before the addition of the next layer. A porous tube was placed about 10.2 cm from the injection chamber roughly midway up in the second Mil-3 layer.

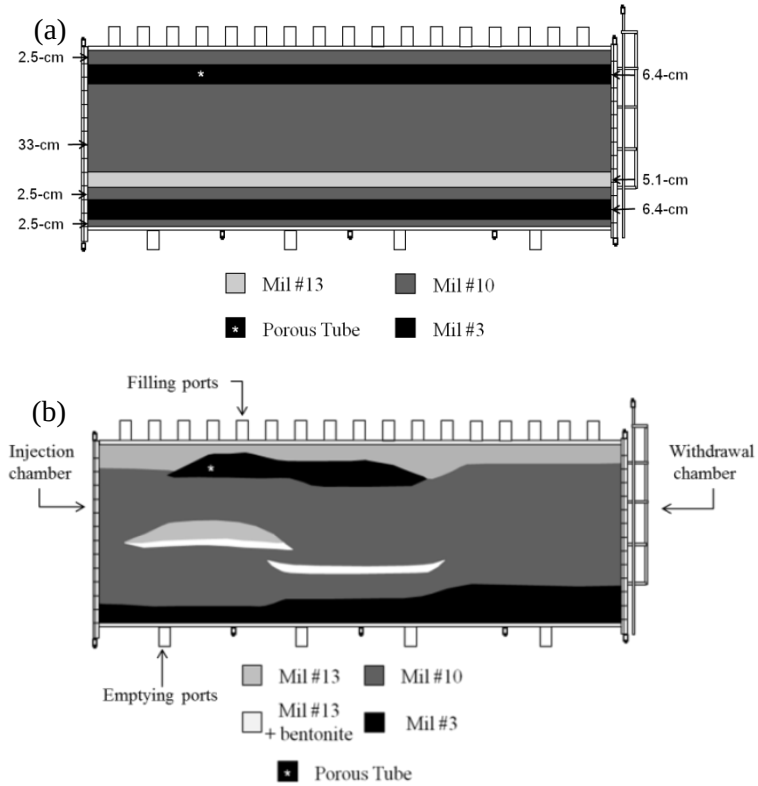

Figure 2. Schematic diagram showing the layered medium of the first experiment (a) and the lenticular medium of the second experiment (b).

The second experiment focused on examining the potential advantages of discontinuous layers of varying hydraulic conductivity imbedded in a background medium (Mil-10), explores the mixing and flow behaviors of dense fluids in lenticular media and the possibilities of sequestering dense fluids within the system (Figure 2b). A 60 cm long discontinuous high conductivity layer (Mil-3) was added as a 7.5 cm thick horizontal layer at about 32.5 cm away from the injection chamber and ended as a concave lens. A continuous Mil-13 layer was placed at the top of the flow tank above the Mil-3 lens. A continuous Mil-3 layer with an increasing in thickness from 5 cm to 12.5 cm was placed at the bottom of the flow tank. Two very low conductivity lenses comprised a mixture of bentonite and glass beads were placed at about 32.5 cm and 40 cm from the top of the flow tank. The first discontinuous layer, which is about 40 cm long and 2.5 cm thick, had a slight convex down structure. It was located about 25 cm away from the injection chamber. This layer was overlain by a 5 cm thick Mil-13 layer with a similar shape. The second discontinuous layer which was 2.5 cm thick and 60 cm long, had a slight concave up shape. It was situated at about 55 cm away from the injection chamber (Figure 2b).

The process of filling the tank with water began by evacuating air from the porous media by injecting CO_2 gas through the injection ports located at the bottom of the tank. Next, the tank was filled from below slowly with deaired water. Additional beads were added to the top layer using the filling ports to account for settling during the filling process. Water was pumped through the injection chamber at a high rate for about two days to dissolve any remaining trapped gas.

During the experiment the background flow was maintained at an average flux of 2.1 ml per minute. We injected a 10 g/L NaCl (Sigma Aldrich, Reagent Grade) solution into the flow tank through the injection port that is close to the injection chamber (Figure 2a,b) at an average flux of 0.75 ml per minute. Water and tracer were pumped into the flow tank with the help of two (Ismatec BV-GE) peristaltic pumps. Rhodamine WT (RWT) (Keyacid Rhodamine 20% active solution, Krompton and Knowles, NC) was added to the saline (Sigma Aldrich, Reagent Grade) solution as a tracer to monitor the migration of dense solution. RWT is generally considered as a conservative tracer but the extent of sorption varies as a function the many parameters such as dye isomer, concentration, solution pHs etc. (McNeil et al. 2006) but no significant sorption onto glass beads was reported by previous investigators (Schincariol, 1998 and Swartz and Schwartz, 1998) and the density of the RWT solution was essentially identical to that of deionized water (Schincariol and Schwartz, 1990). Digital images were taken regularly to record the migration of the tracer solution.

Image analysis techniques provided the means of monitoring the dye concentration within the tank. Black felt was set up around the tank in order to minimize reflections of the surroundings on the front of the flow tank. Two 600 watt halogen work lights were placed about 2 meters away from the tank projecting light at 45 degrees from each side of the tank to create even illumination. A Soligor spotmeter was used to check the lighting across the tank was even. The change in light intensity across the tank was brought to below 1/6 of a f-stop as measured by the spotmeter. A Sony 10 Megapixel Digital Camera was set on a tripod about 4 meters away from the tank. Kodak Gray Scale cards (with known optical density) were placed at the top of the tank. Analysis of the digital data with MATLAB v. 6.5 following the methodology described in McNeil et al. (2006). We started by calibrating the digital images of the experiment to the background images by resizing and rotation. Noise levels in the images were reduced by using a median filter. Monochromatic images were generated from the green spectrum due to its high sensitivity to RWT concentration (McNeil et al., 2006). Images were set to 16-bits/channel. An optical density value for each pixel was calculated by utilizing the relationship between the given optical density values of the Kodak Gray Scale cards and their corresponding intensity values. Because optical densities are additive, the background image could be subtracted from images collected through an experiment to isolate the tracer plume (Schincariol, 1993). We segmented the background image into optically distinct regions using average optical densities (McNeil et al., 2006).

In order to calibrate the concentrations of RWT tracer associated with the optical densities on the Kodak Gray Scale card, two RWT standards of known concentration (50 mg/L, 300 mg/L) were injected into the flow tank from the injection chamber. Digital images were taken once the RWT standards filled the flow tank completely. Optical density values for each calibration run were used to find an equation that defines the relationship between the optical density and concentration for each optically distinct interval. Then these equations were used to map the concentration distributions of saline solutions at different times.

4.1.2. Mathematical modeling

We used the finite element code MITSU3D (Ibaraki, 1998) to model our experimental work to gain insight into variable density flow in horizontal and lenticular media. MITSU3D simultaneously solves the equations describing transient groundwater flow and advective–dispersive transport of the contaminant plume. The transient groundwater flow equation can be

written mathematically as:

$$\frac{\partial}{\partial t}(n\rho) = -\nabla \cdot \{\rho q\} \tag{1}$$

where t is time, n is porosity, ρ is fluid density, and q is groundwater velocity, described by:

$$q = \frac{k}{\mu_f}(\nabla P - \rho g \nabla Z) \tag{2}$$

where k is intrinsic permeability, μ_f is fluid viscosity, P is pressure, g is the gravitational constant and Z is distance from datum. The advection-dispersion equation is written as:

$$\frac{\partial}{\partial t}(nc) = \nabla \cdot (nD_{ij}\nabla c) - \nabla \cdot (cq) \tag{3}$$

where c is solute concentration and D_{ij} is the dispersion coefficient, described by Bear (1972).

MITSU3D solves equations (1) and (3) simultaneously given some simulation domain, associated boundary, initial conditions and a set of parameters, which include intrinsic permeability, porosity, diffusion coefficient, and longitudinal, transverse and vertical transverse dispersivities, initial solute conditions (source location, initial concentration, and release rate), and initial pressure conditions.

The code has been applied in other studies of variable density flow. Ibaraki et al. (2000) studied the development of instabilities in layered media using the experimental results, described by described by Swartz and Schwartz (1998). Ibaraki and Schwartz (2001) used MITSU3D to study the efficiency of $KMnO_4$ flooding in the destruction of DNAPLs in source zones in heterogeneous media. Indications are that the solver in MITSU3D is up to five times faster than other popular codes, such as SUTRA (Voss, 1984) and SWIFT (Ward et al., 1984).

The simulation domain is composed of 1x1 cm nodes and discretized as 192 columns and 62 rows. Three additional columns were added on each side of the domain to represent the influent and effluent reservoirs. The grid-blocks there were assigned values of hydraulic conductivity about 500 times higher than that of the Mil-5 (Figure 3b). The simulation domains and the boundary conditions are shown in Figure 3.

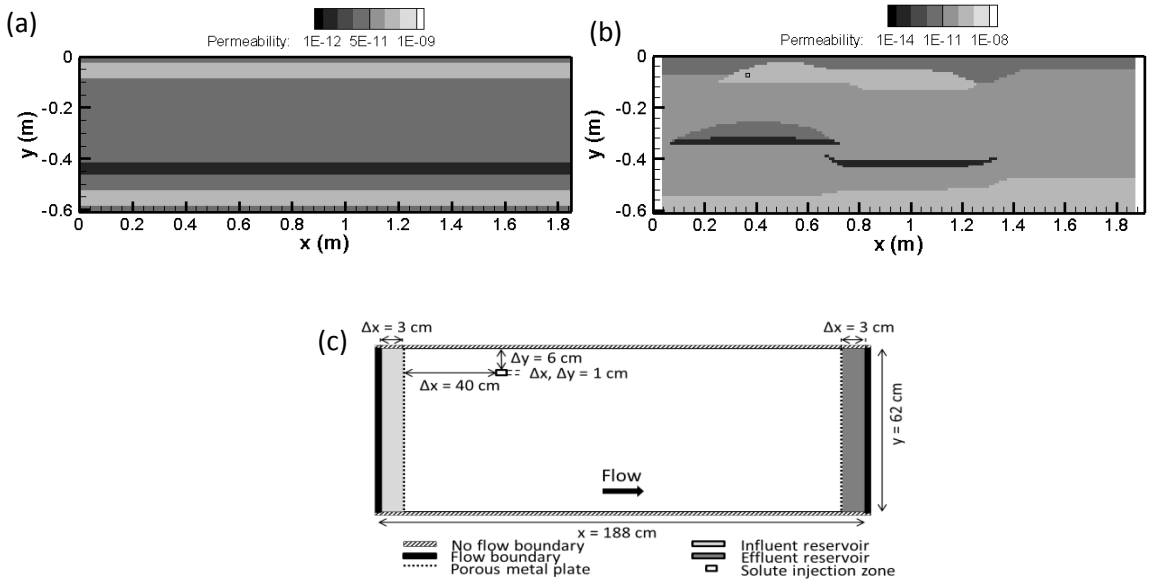

Figure 3. Conceptual models for the MITSU3D simulations of the experiments (grid size of 1x1 cm). (a) the layered medium of the first experiment, (b) the lenticular medium of the second experiment, (c) boundary conditions utilized in the MITSU3D simulations.

4.2. Permanganate gel (PG) for groundwater remediation: Compatibility, gelation, and release characteristics

A new CRP scheme proposed for this study involves the development of highly concentrated MnO_4^- (permanganate) gel (PG) solution that (i) sinks through the porous media, (ii) slowly gels as it spreads away from the injection wells to form a solid MnO_4^- gel, and (iii) slowly releases MnO_4^- to groundwater over an extended time period of months to years. This type of remedial scheme could be cost-effective for treating large, dilute, or deep plumes, because it may facilitate lateral spreading of oxidant, provide controlled level of oxidant within the target area over extended period of time, and reduce costs for well installation and operation.

As the initial step, this study investigated the possibility of creating a MnO_4^- gel solution. The challenge was to find a gel that did not react with MnO_4^-. To this end, we undertook experiments, testing the compatibility and the miscibility of gels, such as chitosan, aluminosilicate, silicate, and colloidal silica gels, with MnO_4^-. In addition, gelation and MnO_4^- release characteristics of two of the promising gels, i.e., silicate and colloidal-silica gels, were investigated through a series of batch and flow-through column tests. Results of this study provide essential knowledge required for further developing the novel remedial scheme using the PG.

4.2.1. Materials

For this study, we tested chitosan, aluminosilicate, silicate, and colloidal silica gels to determine their reactivity and miscibility with $KMnO_4$, and gelation and release characteristics. Other potential biogels such as xanthan and hydrolyzed polyacrylamide were excluded because they

were found to be chemically incompatible with MnO_4^- (Smith et al., 2008). Initial experiments included replicable gel creation and determination of interactions with MnO_4^- over time. Chemical compatibility and miscibility of gels with MnO_4^- were monitored by mixing known amounts of $KMnO_4$ with gels and measuring temporal changes in the concentration of MnO_4^-. Gelation characteristics of PG solution were investigated by a series of batch experiments providing measurements of changes in gel viscosities with time with the addition of saline $KMnO_4$ solutions, and $KMnO_4$. Release rates of MnO_4^- from the gelated PG were measured flow-through column tests. Detailed descriptions about the materials and experimental procedures are as follows (Olson, 2011).

An ACS reagent 99% $KMnO_4$ and high molecular weight chitosan were obtained from Sigma-Aldrich®. The degree of deacetylation of chitosan, as reported by Sigma-Aldrich® was greater than 75%. ACS reagent grade oxalic acid dihydrate was purchased from Acros®. Certified ACS sulfuric acid was obtained from Fisher Scientific®. Sodium metasilicate nonanhydrate was obtained from MP Biomedicals and sodium aluminate nonanhydrate was obtained from Strem Chemicals®. Silicate solutions (KASIL 6, KASIL 1, and Ru Na-silicate) were obtained from PQ Corporation®. Bindzil 1440 colloidal silica was obtained from Wesbond Corporation®. Sodium thiosulfate purchased from Fisher Scientific® was used to treat all MnO_4^- prior to proper disposal.

Permanganate concentrations were analyzed using a UV-VIS spectrophotometer (UV-1800 Shimadzu) at a wavelength of 525 nm, with predetermined time intervals ranging from 10 to 14,400 min. Viscosities were measured using a Thermo Scientific HAAKE Viscotester 2 plus. The pH values were measured using an IQ 150 pH/mV/Temperature System with general purpose round-tip stainless steel probe.

4.2.2. Sample preparation

Compatibility of chitosan gels with MnO_4^- was tested as follows. For chitosan-oxalic acid gel, coarse ground flakes and powder chitosan (3.75 g) was dissolved in oxalic acid (75 mL, 0.2 M) and mixed by stirring at 50°C (Hamdine et al., 2005). Permanganate solution (25 mL, 0.25 g L^{-1} $KMnO_4$) was subsequently added. For chitosan-sulfuric acid gel, coarse ground flakes and powder chitosan (3.75 g) were dissolved in sulfuric acid (75 mL, 0.2 M) and mixed under stirring at 50°C. Permanganate solution (25 mL, 2 g L^{-1} $KMnO_4$) was subsequently added to the mixture.

The reactivity of MnO_4^- and the aluminosilicate gel was tested using the following procedure. Sodium metasilicate (6.98 g) was dissolved in 50 mL of deionized H_2O. Sodium aluminate (2.5 g) was dissolved in 20 mL of Millipore H_2O. The two solutions were then mixed under rapid stirring conditions (e.g., Lairan and Mann, 1936). Ten mL of 1 g L^{-1} $KMnO_4$ was subsequently stirred into the gel. Permanganate concentrations were analyzed periodically up to 120 min.

Compatibility of silicate solutions (potassium silicate solutions: Kasil 1, Kasil 6 and sodium silicate solution: Ru) with $KMnO_4$ was tested by mixing a concentrated solution of $KMnO_4$ with a known volume of silicate solutions. Viscosities of various silicate solutions with $KMnO_4$ granules or concentrated (60 g L^{-1}) $KMnO_4$ solutions were measured with the following procedures. Temperature, pH and viscosity of 150 mL of silicate solution were measured. A given amount of granular $KMnO_4$ was added under mild (~40°C) heating and stirring conditions

to promote the dissolution of the $KMnO_4$. Once all of the $KMnO_4$ was dissolved, the solution was allowed to cool to room temperature.

Compatibility of colloidal silica with MnO_4^- was tested by mixing a concentrated solution of $KMnO_4$ with a known volume of colloidal silica. Colloidal silica (150 mL) was mixed with a given amount of granular $KMnO_4$. The mixture was placed under constant stirring conditions. Viscosity was measured at given time intervals ranging from 0 to 200 min, depending on the mass of $KMnO_4$ used.

4.2.3. Flow-through tests

Permanganate release from the hardened silicate and colloidal silica solutions was measured by flow-through tests. Samples of hardened silicate solutions were prepared using a variety of setting agents including bentonite, $Ca_3(PO_4)_2$, and portlandite. For 20 mL of silicate solution containing 1 g of $KMnO_4$, 2 g, 1.5 g, and 2 g of bentonite, $Ca_3(PO_4)_2$, and portlandite were added, respectively. The mixture was subsequently stirred until a highly viscous gel formed. The gel was allowed to air dry for 12 d, after which it was placed into a container with holes to speed up the drying process. After 4 additional days, the hardened cylinders were solidified and ready to use in a column test. Samples of hardened colloidal silica solutions were prepared by mixing granular $KMnO_4$ (0.75 g) with 25 mL of Bindzil 1440 colloidal silica. The mixture was rapidly stirred until the gel became highly viscous. The viscous gel was poured into a cylindrical mold and allowed to harden overnight. Kontes Chromaflex columns (V = 271 mL, ID = 4.8 cm, L = 15 cm) were used for the flow-through tests. Distilled water was passed through the columns at a rate of 10 mL min^{-1}, using a Masterflex L/S Digital Drive with an L/S Multi-Channel Cartridge Pump Head. Samples were taken at given time intervals and analyzed for MnO_4^- concentration.

4.3. Harnessing the complex behavior of ultra-dense and viscous treatment fluids as a strategy for aquifer remediation

We tested three concepts in our experiments. The first concept was previously described in Section 4.1 and involves the injection of a saline solution that mimics a dense $KMnO_4$ treatment solution into heterogeneous media and examines the flow of dense solutions. The second approach explores the use of much more dense and potentially more viscous silicate solutions in delivering the $KMnO_4$ into the media as a dense and viscous fluid. Finally, the third approach investigates the “time-delayed gelling” concept and slow-release of treatment fluids in-situ.

4.3.1. Validation modeling

Part of our modelling effort was concerned with gaining confidence in the ability of the code to simulate complex variable-density flows. We concentrate illustrative modelling using data from Schincariol and Schwartz (1998). Schincariol and Schwartz (1990) performed a series of experiments on the transport of saline solutions through a lenticular media (Figure 4a). We show model results of the 10 g/L NaCl experiment by using MITSU3D and the grid shown in Figure 4b. The top and bottom boundary conditions were no flow for flow and transport and the left and right boundaries were constant flux for flux and transport (Figure 4c).

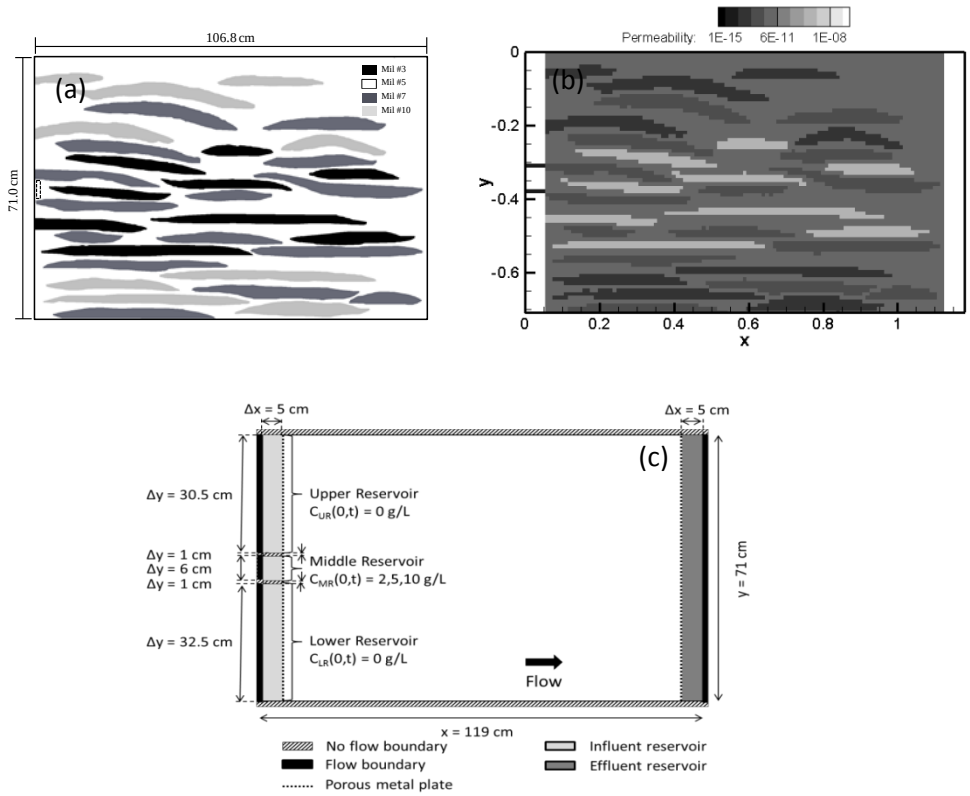

Figure 4. Lenticular media used by Schincariol and Schwartz (1990) for the flow-tank experiments where the dotted box indicates location of dense fluid injection (a), simulation domain (119x72) (b) and boundary conditions (c) used in MITSU3D simulations.

4.3.2. Flow tank experiments

Experiments involving dense, viscous silicate solutions were conducted in a 33 cm tall and 80 cm wide glass flow tank and 61 cm tall and 183 cm wide plexiglass flow tank. Three experiments were performed in the small flow tank two with simple layered set up comprised of high and low conductivity media and one with high and low conductivity lenses. In all experiments uniform flow was created across the tank using a peristaltic pump.

4.3.2.1. Dense/viscous fluids

N-Clear sodium silicate solution (PQ Corp.) was injected slowly into the high conductivity layer. We added 300 mg/L RWt dye to observe the solution in the flow tank. N-clear sodium silicate solution had a viscosity of 180 cp and a high density of 1.38 g/cm^3 with silica to sodium weight ratio of 3.22.

4.3.2.2. Time-delayed gelling

Two small flow tank experiments were done to demonstrate the time-delayed gelling property of silicate solutions and the release of the dye and permanganate from the gelled solution.

In the first small flow tank experiment, we prepared a 90 wt % diluted silicate solution and 70 wt % $NaHCO_3$ (8 g $NaHCO_3$/100 ml H_2O) solution and then we mixed these solutions on a 60- 40 wt % basis, respectively. To facilitate the observation of this solution in the flow tank, we added 300 mg/L RWt dye. We set up a small flow tank with a higher conductivity layer sandwiched between lower conductivity units. The gelling solution was injected into the high conductivity layer and it gelled in 45 minutes. The initial low viscosity of this mixture was useful for easy injection of this solution into the targeted layer.

The second small flow tank experiment differed from the first small flow tank experiment in terms of the concentration and the mixing proportions of the solutions. 1.5 L of gelling solution was injected over the clay lens (4 wt % bentonite powder added to fine grained size Mil-13 glass beads) in two batches. The second batch was injected about 1.5 hours later than the first batch. This gelling solution was a 50-50 wt % mixture of 30 wt % diluted N-clear sodium silicate solution and 30 wt % diluted $NaHCO_3$ solution (8 g $NaHCO_3$/100 ml H_2O). In addition, 20 g $KMnO_4$ was added to 500 g of 30 wt % $NaHCO_3$ solution. The gelling took place approximately in 1 hour. Over 1 L of the third batch was injected into the high conductivity lens. This gelling solution was slightly different than the one injected over the clay lens. It was a 40-60 wt % mixture of 40 wt % N-clear silicate and 30 wt % $NaHCO_3$, respectively. Additionally, 24 g of $KMnO_4$ was added to 600 g of 30 wt % $NaHCO_3$ solution.

The third experiment was done in the big flow tank where the gelling solution was injected over a clay layer (4 wt % bentonite powder added to fine grained size Mil-13 glass beads) and into the high conductivity lens. The gelling solution was a 50-50 wt % mixture of 60 wt % diluted sodium silicate solution (N-Clear, PQ Corp) and 47 wt % diluted sodium bicarbonate solution (8 g $NaHCO_3$/100 ml H_2O). 8 batches of 1 L solution was injected in 5 hours. The gelation occurred in 1 hr and 25 minutes after the solution was prepared. A background flow was maintained by pumping water day into the flow tank at the rate of 0.008 m^3/day.

4.3.3. Diffusion coefficient measurements

We prepared two types of silicate hydrogels which were prepared in a similar way but one of them has higher sodium silicate concentration. 0.06 g of $KMnO_4$ was dissolved in 15 g of 60 wt % $NaHCO_3$ solution which was mixed with 15 g of 50 wt % sodium silicate solution. The mixed solution then was poured into a 60 ml syringe. The tip of the syringe was cut so that after the gel was set, it was pushed out of the syringe and cut into a 0.75 cm thick slab using a razor blade. The weight of the slab was 4.98 g. This slab was put into a 1.0 cm thick ring to keep the diameter of the slab constant during the release experiment. The apparatus used for MnO_4^- release from silicate hydrogel is illustrated in Figure 5. Gel in plastic ring was placed on sample holder which was brought into contact with deionized water (164.1 ml) at room temperature. The deionized water was magnetically stirred. The diffusion layer of this apparatus was very thin. The solution was withdrawn from the reservoir continuously with the help of a peristaltic pump and carried to 1 ml cuvette inside the UV-VIS photospectrometer and analyzed at every 30 seconds for 2 hours at 525 nm. Then they were pumped back into the reservoir.

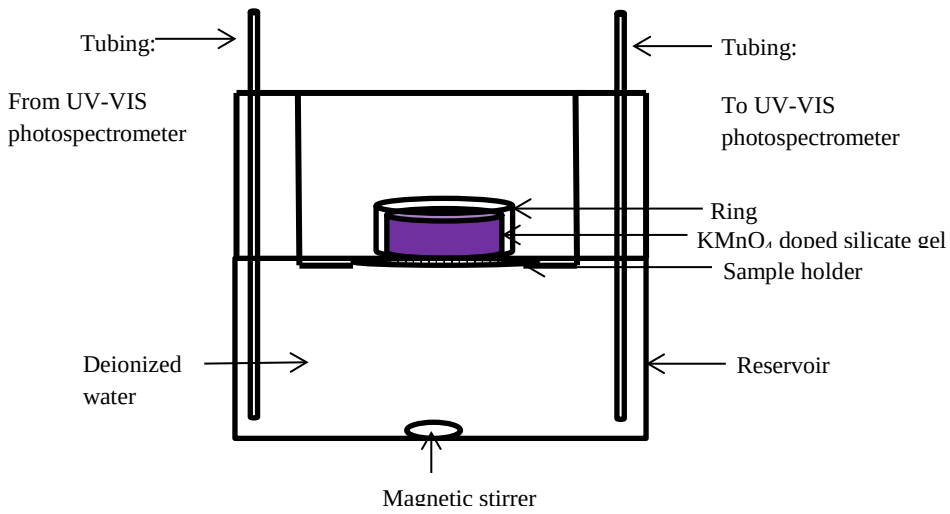

Figure 5. Permanganate release apparatus.

4.4. Development and characterization of slow-release permanganate gel (SRP-G) for groundwater remediation

Colloidal silica is a highly polymerized species of silica that contains amorphous silica particles in suspension in a liquid phase (sol). Through the sol-gel process, the colloidal solution (sol) forms an integrated network in which the solid particles form a continuous solid skeleton that encloses a continuous liquid phase (Iler, 1979).

This study aims to further the development of a novel remedial approach using SRP-G. Specifically, we tested the hypothesis that colloidal silica, through the sol-gel process and its modifiable gelation times, provides a suitable diffusional matrix and adequate gelation and release times for use in SRP-G methodology. The desired SRP-G solution for this study is expected to have an initial viscosity that is low enough (~ 4 cP) to allow for well-based injection and gelation times of more than 3 d, so that the SRP-G solution can flow away from the injection wells before gelation occurs. The key issues investigated were (i) the gelation and release characteristics of SRP-G in water and (ii) the mass transport, gelation, and release dynamics of SRP-G in a flow-through sandy media. The results of this study provide useful information for further developing SRP-G methodology.

4.4.1. Materials

Granular $KMnO_4$ was purchased from Sigma-Aldrich, and Bindzil 1440 Colloidal Silica was purchased from Wesbond Corporation. Bindzil 1440 was chosen for this study due to its low viscosity (15 cP) and relative high silica concentration (40 %). Other physical properties of this solution are listed in supplementary material 3. Glass columns of variable lengths (KONTES Chromaflex L x ID = 15, 60, or 120 cm x 4.8 cm) and a peristaltic pump (Cole-Parmer Masterflex L/S) were used for column tests. The viscosities of select gels were measured using Viscolite 700 equipment (Vindum Engineering; Range 0-10,000 cP). Permanganate concentrations were measured using a UV-Visible Spectrophotometer (UV-1800 Schimadzu) and a wavelength of 525 nm.

4.4.2. Sample preparation

For gelation tests, variable amounts of $KMnO_4$ granules were mixed with 25 mL Bindzil 1440 colloidal silica to yield variable $KMnO_4$ concentrations (6 to 40 g L^{-1}), and subsequent viscosity increases were monitored over time to determine the effect of ionic strength on the gelation rate. These tests also provided insights into the effect of dilution upon gel formation. Dilution is an important consideration when ascertaining gel behavior, because the gel solution is emplaced in conditions where it will encounter dilution through advection-dispersion processes. In batch tests, gelation was assessed qualitatively via resistance to the insertion and movement of a glass rod as well as visual observation of the state of the solution. The use of qualitative methods to measure gelation is common in colloidal silica grouting applications (Persoff et al., 1999).

4.4.3. Flow-through tests

Flow-through tests were conducted using glass columns (L x ID = 15 x 4.8 cm) to measure the net release rates of MnO_4^- from the gelated SRP-G. Using the peristaltic pump, deionized water was pumped vertically through columns at a machine-controlled flow rate of 200 rpm. Water was pumped in through the bottom of the column and out through the top to achieve perfect sink conditions for MnO_4^- immediately around the SRP-G (Figure 6). The column effluent was collected throughout the test, initially at 15-20 min intervals, which were adjusted throughout the course of the experiment. Effluent samples were then monitored for MnO_4^- concentrations using UV-VIS spectroscopy. Ambient flow rates were measured during each sampling event. The mass flux of MnO_4^- from the SRP-G cylinder, calculated from the measured flow rates and concentrations, was used to determine the cumulative mass of MnO_4^- released from the SRP-G cylinder.

Figure 6. Photo showing the column setup and release of MnO_4^- from the gelated CRP-G cylinder in the glass column.

Column flow-through tests were conducted to monitor the spreading, gelation, and MnO_4^- release of the SRP-G in the presence of saturated porous media. Glass columns (L x ID = 120 cm x 4.8

cm) were oriented horizontally and packed with coarse-grained silica sands at an assumed porosity of 0.3. The total volume of the columns was 2.16 L, which provided an estimated residence time of 14 h for water flowing through the column at an estimated average linear flow velocity of 2.1 m d^{-1}. Flow was facilitated in the long column by loosening the output end to allow free flow of water through the sand (due to the pressure differential created between the inlet and the outlet of the column for the duration of each test). Samples were initially collected every 2 h, after which the collection times were adjusted throughout the remainder of the testing period.

SRP-G solutions of varying $KMnO_4$ concentrations were pumped into the column using the peristaltic pump at a flow rate of 50 rpm, yielding a total gel injection time of 24 min. After the SRP-G solution was injected into the column, the pump speed was reduced to an ambient flow rate of 30 rpm. Gelation within the column was monitored via video recordings and photographs during the entire column test. Release of MnO_4^- from the gelated SRP-G was monitored by measuring the MnO_4^- concentrations of the outflow samples using UV-VIS spectroscopy. The objective of these tests was to achieve gelation within the column before progressing to delayed-gelling approaches. Once gelation was achieved in the column, the release of MnO_4^- was monitored.

4.5. Description and verification of a novel flow and transport model for silicate-gel emplacement

We describe a new modeling approach that originates from a need in remediation problems to consider a miscible treatment fluid with a capability of evolving to a gel. More specifically, an aqueous solution with an ordinary viscosity can experience at least a four order-of-magnitude increase in viscosity as gelation occurs. Our basic approach is to use dense fluids and slow-release gels to deliver remediation chemicals to deeper plumes and less permeable units. This approach takes advantage of the unique flow and mixing properties of dense fluids, and the potential of engineered gels as a diffusion-controlled mechanism for releasing the treatment chemical. The essence of this new remediation approach is all about increasing the residence time of oxidants close to the site where they are injected, which will be determined by characteristics of the actual contaminated site.

Our goal with this aspect of the study is to describe and demonstrate an approach for modeling this variable density flow/gelation problem. It also utilizes illustrative data from a series of flow tank experiments to help validate the new simulation concept. In order to diminish data uncertainty, these experiments were designed to be as simple as possible with a (nearly) homogeneous and isotropic medium. Convective dispersion is helpful in mixing the dense fluids.

4.5.1. Materials and experimental setup

Silicate solutions are widely used as chemical grouts and considered to be environmentally safe, economic and stable inorganic solutions (PQ Corp., 2012). They are generally considered to be among the strongest and least toxic of the existing chemical grouts (Karol, 2003).Silicate solutions are not designated as hazardous substances under section 102(a) of the Comprehensive Environmental Response, Compensation, and Liability Act (CERCLA). They are not listed as extremely hazardous substance and toxic chemical under §302 and §313, respectively of the Superfund Amendments and Reauthorization Act (SARA) Title III. All ingredients of these

solutions are listed on the Toxic Substances Control Act (TSCA) inventory. Dilute silicate solutions are relatively dense with added benefits of a relatively low initial viscosity (~ $2 \cdot 10^{-3}$ Pa · s) and the potential for gelling after a predetermined time period (PQ Corp., 2012). When dilute silicate solutions are acidified, silicate anions polymerize to form an amorphous, porous gel, which is a coherent, rigid, three-dimensional network of contiguous particles of colloidal silica (Blankenship, 2002). Temperature, pH, total silica concentration and type of setting agent can affect the degree and timing of polymerization (PQ Corp., 2012; Karol, 2003).

We conducted three experiments with a small flow tank to observe the transport and gelation of three different solutions in a saturated homogeneous porous medium. To produce solutions for injection we used N-Clear sodium silicate solution (PQ Corp., 2012). The quantity of dissolved silica was 28.7 wt. % with a silica to alkali weight ratio of 3.22. The initial density and viscosity of the stock solution were 1380 $kg.m^{-3}$ and ~ 1.8×10^{-1} Pa · s, respectively. The solution was then diluted with deionized water to 30% by weight with diluted sodium bicarbonate solution as the setting agent. A concentrated bicarbonate stock solution (8 g $NaHCO_3$/100 mL H_2O) was diluted with deionized water to 65%, 60%, and 55% by weight. Diluted bicarbonate solutions were mixed with diluted silicate solutions with mixing proportions 50% and 50% by weight, respectively. The first, second, and third gelling solutions incorporated 65%, 60%, and 55% bicarbonate solutions, respectively, to control gelation rates in the three injection experiments (experiments 1, 2, and 3). Dense solutions were colored with 300 mg L^{-1} Rhodamine WT (RWT) to facilitate visual observation of the time-delayed gelling. Density and viscosity of these three solutions were determined using a pycnometer and a u-tube calibrated Ubbelohde glass viscometer following ASTM D445 - 12 (2006) and ASTM D446 - 12 (2008) (see Tables 2 and 3).

To support the modeling studies, we undertook complimentary experiments in a small flow tank. The experiments involved the injection of a viscous silicate solution that was capable of gelling on the order of minutes to several tens of minutes. The small glass flow tank is 0.45 m high, 0.97 m long and 0.17 m wide. Between the inflow and outflow chambers (0.13 m wide each) is a flow chamber filled with uniform, spherical glass beads (Potters Industries, NJ) with hydraulic conductivities ranging from $3.0 \cdot 10^{-3}$ $m.s^{-1}$ (Schincariol and Schwartz, 1990) to $4.2 \cdot 10^{-3}$ $m.s^{-1}$ (Swartz and Schwartz, 1998). Solutions were injected into the saturated porous medium with a syringe immediately after their preparation.

Fluid movement in the flow tank was monitored using a digital high definition video camera recorder (Sony HDR-SR8). The processing of individual scenes involved converting information on light intensity to optical density because optical density is proportional to the concentration of the dye. The optical density was calibrated using a gray scale visible at all times during the experiments. The gray scale has 20 bars with 0.1 optical density increments ranging from 0.0 optical density (white) to 1.9 optical density (black). Zones of higher solute concentrations are exemplified by high normalized light densities and vice-versa. Digital images of the blank flow tank and the evolving fluids at different time steps were converted into light density maps following McNeil et al. (2006). The image analysis used the image processing toolbox of Matlab R2009b. The approach involves the following eight steps: (1) image registration that rotates images from the experiment to provide both the background and experiment images with the same orientation, (2) image cropping to create images of exactly the same size, (3) transformation of the color components, which involves choosing only the green color

component due to its high sensitivity to dye concentration (McNeil et al., 2006), (4) development of an intensity versus density calibration curve assuming light intensity of green component is directly proportional to light transmittance (McNeil et al., 2006), (5) background subtraction to isolate the plume, (6) median filtering to reduce noise, (7) image resizing that facilitates contouring using bicubic interpolation and antialiasing, (8) contour mapping.

4.5.2. Numerical methods

The following sections describe the modeling approach, including the basic equations for density-dependent flow. We also describe the concept and parameters of the approach used to model the gelation process.

To simulate the gelation process, we define a “solute 1" with concentration ω_1, which is used to calculate the fluid density. Additionally, an auxiliary “solute 2" with concentration ω_2 is defined, which has no influence on fluid density. Solute 2 experiences a 1st order decay process. The boundary conditions are the same for both solutes, i.e. when the decay coefficient $\lambda = 0$, both concentrations are the same values. However, when $\lambda > 0$, the difference in the concentrations of the two solutes yields the necessary information about the time of residence within the domain. This information can be used to calculate the viscosity increase due to gelation (see section 3.3). Alternative approaches to calculate residence time for injected solutes would be to use a groundwater age approach (Goode, 1996), or random-walk particle tracking (Kinzelbach, 1988).

Furthermore, Todd et al. (1993) and Gallagher and Finsterle (2004) described mathematical or numerical models to predict the behavior of gelling systems in porous media (e.g. special modules in iTOUGH2), combining transport equations for the various chemical species with models of gelation kinetics, deposition, compaction and filtration of gel aggregates. However, these approaches either require a large number of parameters that are unknown and difficult to determine, or cannot represent special phenomena that we observed during gelation, like concentration dependent viscosity change.

For simulating of density-dependent flow, we follow standard methods for groundwater flow in porous media (e.g. Kolditz et al., 1998). The governing equation can be written as

$$\frac{\partial(S\rho\phi)}{\partial t} + \nabla \cdot (\rho\phi\mathbf{v}) = \rho Q_\rho \tag{4}$$

where S is saturation ratio, ρ is fluid density, ϕ is porosity, t is time, $\mathbf{v}$ is fluid velocity, and ρQ_ρ is source term of fluid mass. The Darcy term can be formulated as

$$q = \phi \mathrm{v} = -\frac{\kappa\rho_0 g}{\mu}(\nabla h + (\frac{\rho-\rho_0}{\rho_0})\mathrm{e} \tag{5}$$

with

$$\boldsymbol{\kappa} = \frac{\mu}{\rho_0 g}\mathbf{K} \tag{6}$$

where q is the Darcy vector, κ is saturated intrinsic permeability tensor, ρ_0 is reference fluid density, μ is dynamic viscosity, g gravity constant, e is the unit vector in gravitational direction,

and K is saturated hydraulic conductivity tensor. The equivalent freshwater hydraulic head h can be derived from Bernoulli's principle of hydraulic potential as $h = \frac{p}{\rho_0 g} + z$ where p is water pressure, and z is elevation.

The mass transport process is governed by

$$\boldsymbol{\phi}\frac{\partial \boldsymbol{\omega_i}}{\partial \boldsymbol{t}} + \boldsymbol{\nabla} \cdot (\boldsymbol{\omega_i}\boldsymbol{\phi}\mathbf{v}) - \boldsymbol{\nabla} \cdot (\boldsymbol{\phi}\mathbf{D} \cdot \boldsymbol{\nabla}\boldsymbol{\omega_i}) = \boldsymbol{Q_{\omega_i}} \tag{7}$$

where $\boldsymbol{\omega_i}$ is concentration of the respective solute $\boldsymbol{i}$ and $\boldsymbol{Q_{\omega_i}}$ are source terms of the respective mass transport process. Following Bear (1979), the dispersion tensor $\mathbf{D}$ is defined by

$$\mathbf{D} = \boldsymbol{\tau}\boldsymbol{D_m}\boldsymbol{\delta} + \boldsymbol{\alpha_l}|\mathbf{v}|\boldsymbol{\delta} + (\boldsymbol{\alpha_l} - \boldsymbol{\alpha_t})\frac{\boldsymbol{v_i}\boldsymbol{v_j}}{|\mathbf{v}|} \tag{8}$$

where $\boldsymbol{\tau}$ is tortuosity of the porous medium, $\boldsymbol{D_m}$ is molecular diffusion coefficient of the solute in water, $\boldsymbol{\delta}$ is Kronecker-delta, and $\boldsymbol{\alpha_{l,t}}$ are longitudinal and transverse dispersivities, respectively. The decay of solute 2 is defined by

$$\frac{\partial \boldsymbol{\omega_2}}{\partial \boldsymbol{t}} = -\boldsymbol{\lambda}\boldsymbol{\omega_2} \tag{9}$$

with $\boldsymbol{\lambda}$ is decay coefficient, that is defined by the time until gelation $\boldsymbol{t}_{\text{gel}}$ through

$$\boldsymbol{\lambda} = -\frac{\mathbf{ln(0.5)}}{\boldsymbol{t}_{\text{gel}}} \tag{10}$$

The equations of state for density and viscosity are defined in (11) and (12), whereas the former solely depends on concentration of solute 1 described through a linear relationship following Kolditz et al. (1998) as

$$\boldsymbol{\rho}(\boldsymbol{\omega_1}) = \boldsymbol{\rho_0}(\mathbf{1} + \boldsymbol{\gamma}\boldsymbol{\omega_1}) \tag{11}$$

with $\rho_0$is density at $\omega_1 = 0$, and is coefficient of expansion resulting from the change of concentration of the solute at constant pressure. Laboratory measurements showed that the viscosity of the initial, non-gelated solution depends on the extent of dilution. Thus, base viscosity is defined as

$$\boldsymbol{\mu}(\boldsymbol{\omega_1}) = \boldsymbol{f} \cdot \boldsymbol{\mu_0^{\alpha\omega_1}} \tag{12}$$

where μ_0 is initial viscosity, α is a factor describing the result of viscosity change due to concentration ω_1, and $f \geq 1$ is the factor for viscosity increase due to gelation.

A mixture of large polydisperse soluble macromolecular chains called a “sol” transforms into a “gel” when the polymer size increases and solubility decreases (Gulrez et al., 2011). The concentration and types of silicate and acid solution can affect the sol-gel process. When a solution is injected into the ground, the quantity of added acid determines whether it gels quickly or more slowly after the injection. Also, the resulting gel can be relatively strong or weak. For example, a concentrated silicate solution can start to gel immediately after the silicate and acidic

solutions mix and rapidly form a strong gel. A dilute solution may start polymerization somewhat later after mixing of the silicate and acidic solutions and would form a weak gel.

In this study, we use dimensionless parameters to model the viscosity variation with time through the gelation process. The values of these parameters are well constrained by the experimental data. By studying the increase of viscosity during the laboratory experiments, the following set of equations was formulated to model the gelation process. The term controlling the viscosity increase f in equation (12) is defined by

$$\boldsymbol{f} = \mathbf{1} + \boldsymbol{d} \cdot \boldsymbol{e} \tag{13}$$

which includes two factors, that describe phenomena observed during the laboratory experiments. The first factor, d, creates a viscosity increase, while the second one, e creates the behavior whereby the solute only forms a gel, when a certain concentration threshold is reached. The factor d defines the viscosity increase following

$$\boldsymbol{d} = (\boldsymbol{\beta}_{\max} - \mathbf{1})(\mathbf{2}\boldsymbol{\omega}_{\mathrm{rel}})^{\boldsymbol{\beta}_{\mathrm{s}}} \tag{14}$$

with $\beta_{\max} \geq 1$ is maximum viscosity increase, $\omega_{\mathrm{rel}} = \frac{\omega_1 - \omega_2}{\omega_1}$ a relation between the two concentrations, and $\beta_{\mathrm{s}} \geq 1$ is a parameter defining the gelation speed. Furthermore, we define a second factor in (13) as

$$\boldsymbol{e} = \left(\frac{\boldsymbol{\omega_1}}{\boldsymbol{\omega_{1,\mu_{\max}}}}\right)^{\boldsymbol{\psi}} \tag{15}$$

with $\omega_{1,\mu_{\max}} \leq 1$ is the concentration of solute 1 when the maximum viscosity increase should be reached, and $\psi \geq 1$ is a factor altering the viscosity increase depending on the present concentration ω_1.

Additionally, we set the following constraints. We consider relative concentrations in the range $0 < \omega_i < 1$. When ω_2 reached half of its initial concentration, maximum viscosity increase is calculated in the factor d, i.e. if $\omega_{\mathrm{rel}} > 0.5 \rightarrow d(\omega_{\mathrm{rel}} = 0.5) = \beta_{\max} - 1$. Furthermore, the value of $e = 1$ if $e > 1$.

When gelation has occurred, viscosity will not decrease in the same way as it increased; rather, the viscosity will remain constant in time. During the experiments, reduction of viscosity of solutions in regions where gelation had occurred was not observed over the initial 6 h. Therefore, if a model cell is a gel and the current calculation of the viscosity μ_t yields a smaller value than in the time step before (μ_{t-1}), the reduction of viscosity μ follows

$$\boldsymbol{\mu} = \frac{\boldsymbol{\epsilon} \cdot \boldsymbol{\mu_{t-1}} + \boldsymbol{\mu_t}}{\boldsymbol{\epsilon} + \mathbf{1}} \tag{16}$$

with $\epsilon \geq 1$ as a factor to decrease reduction of the viscosity.

Figure 7 shows the parameter increases for two parameter combinations. With $e = 1$, the viscosity increase happens early, rapidly, and with a high magnitude (gray lines in Figure 7). With larger values of λ, β_s or $\beta_{\max}$ respectively the increase in viscosity is later, slower, and with a smaller magnitude (black lines).

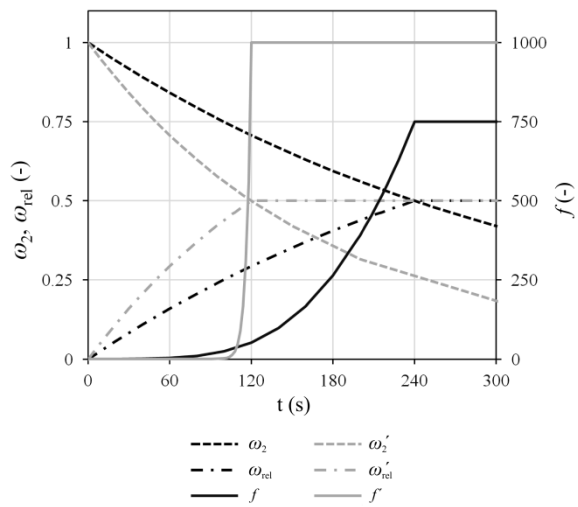

Figure 7. Two exemplary parameter combinations for viscosity increase factor $\boldsymbol{f}$ with $\boldsymbol{e} = \mathbf{1}$; grey lines: $\boldsymbol{\lambda} = \mathbf{5.8 \cdot 10^{-3} s^{-1}}$, $\boldsymbol{\beta_S} = \mathbf{50}$, $\boldsymbol{\beta}_{\max} = \mathbf{1000}$; black lines: $\boldsymbol{\lambda} = \mathbf{2.9 \cdot 10^{-3} s^{-1}}$, $\boldsymbol{\beta_S} = \mathbf{5}$, $\boldsymbol{\beta}_{\max} = \mathbf{750}$.

Figure 8 depicts the influence of e where variations of ψ are shown based on two different values for $\omega_{1,\mu_{\max}}$. The reduction term e provides for gelation to only occur, if a certain minimum concentration is exceeded (compare 1st laboratory experiment). Depending on the fluid mixture used, this boundary may be relatively sharp, or may be observed at different concentrations.

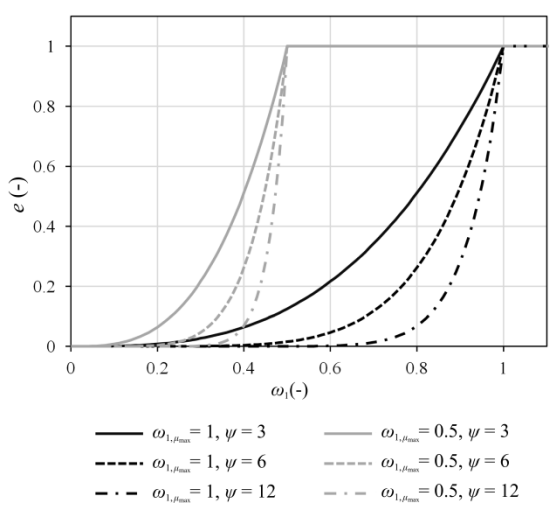

Figure 8. Exemplary parameter combination for reduction factor $\boldsymbol{e}$; black lines: $\boldsymbol{\omega_1}, \boldsymbol{\mu}_{\max} = \mathbf{1}$, grey lines: $\boldsymbol{\omega_1}, \boldsymbol{\mu}_{\max} = \mathbf{0.5}$.

4.5.3. Numerical modeling

We use the open source scientific modeling software package OpenGeoSys (OGS; Kolditz et al., 2012a). This package provides a capability of simulating coupled THMC processes (i.e. thermal, hydraulic, mechanical and chemical). It has been verified for density-dependent flow in various applications (Kolditz et al., 2012b; Walther et al., 2012; Kalbacher et al., 2011; Park and Aral,

2008; Beinhorn et al., 2005). We utilize Oberbeck-Boussinesq approximations which yield sufficiently accurate results for our case, i.e. small expansion coefficients (Kolditz et al., 1998; Johannsen, 2003; Johannsen et al., 2006). OGS is based on the Galerkin finite element method. We use an iterative, sequential scheme for the non-linear coupling of fluid flow and mass transport processes by density and viscosity until convergence (Kalbacher et al., 2011).

Using data acquired through experimental work, the numerical simulations are compared to the laboratory experiments. The conceptual model is depicted in Figure 9; the simulation parameters, including sources, are given in Tables 2-4. The model is set up as a vertical x-z-domain, assuming isotropic and heterogeneous sand. The hydraulic conductivity distribution is assumed uniformly random with a maximum deviation of 15% from the mean conductivity value. Initial conditions are $\omega_i = 0$ and a hydrostatic pressure distribution $p_{\text{ini}}(z) = \rho g z$ with $p_{\text{ini}}(z = 0.28\ \text{m}) = 0$ Pa. At the domain boundaries, we provide no-flow (Neumann type) boundaries for both fluid flow and mass transport, and on the top left corner one Dirichlet type with pressure $p(t) = 0$. At the injection point Pinj, a fluid with constant solute concentrations $\omega_i = 1$ is injected at a constant rate q over the time interval $0 < t < t_{\text{inj}}$ at the beginning of the simulation. When $t > t_{\text{inj}}$, all boundary conditions at P_{inj} are removed. The FE-mesh consists of triangle elements with edge lengths ranging from 5.0×10^{-3} m to 2.5×10^{-3} m due to refinements in the vicinity of the injection point P_{inj}.

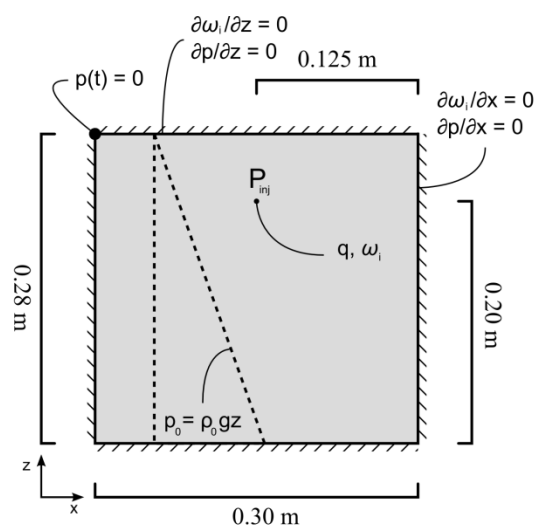

Figure 9. Conceptual model, initial and boundary conditions.

Table 2. Parameters used in the simulations; • acquired through experimental measurement, or * determined through model calibration.

Parameter	Value
Hydraulic conductivity K (m·s^{-1})*	1.5×10^{-3} ($\pm 15\%$)
Porosity ϕ (-)•	0.20
Fresh water density ρ_0 (kg·m^{-3}) •	998.2
Fresh water viscosity μ_0 (Pa·s) •	1×10^{-3}
Viscosity coefficient α (-)•	0.9
Molecular diffusion coefficient D_m (m$^2 \cdot$ s^{-1})*	1×10^{-9}
Longitudinal dispersivity α_l (m) *	1.5×10^{-3}
Transversal dispersivity α_t (m) *	1.5×10^{-4}
Injection time t_{inj} (s) •	60
Injection flow rate q (m$^2 \cdot$ s^{-1}) •	1.5×10^{-5}

Table 3. Simulation specific parameters; • acquired through experimental measurement, or * deducted from experimental observation.

Experiment/simulation number	1	2	3
Decay coefficient γ (-)•	0.06341	0.06541	0.06642
Decay coefficient λ (s^{-1})*	3.85×10^{-3}	7.70×10^{-4}	5.02×10^{-4}
Time till gelation (s)*	180	900	1380

Table 4. Parameters used in viscosity calculation (all unitless); • deducted from experimental observation, or * determined through model calibration.

Parameter	Value
Maximum viscosity increase $\beta_{\max}$ *	1×10^8
Gelation speed β_s •	400
Mass fraction solute 1 for maximum viscosity $\omega_{1,\mu_{\max}}$ •	0.9
Viscosity increase depending on mass fraction ψ •	100
Factor to decrease reduction of the viscosity ϵ •	1×10^4

Yang et al. (2007) measured dynamic shear viscosities at similar solute compositions and found low shear rates (≈ 0.1 s^{-1}). Thus, we assume Newtonian flow behavior for the setups.

Most parameters were determined by measurements or using data from the experiments (porous media and fluid parameters, e.g. porosity, fluid density, initial viscosity of the solutions). However, parameters describing the gelation process are more uncertain. Because the gelation process is rapid, viscosity changed by several orders-of-magnitudes. Thus, certain of the parameters used in our numerical model could only be determined by assuming that generalized viscosity-time functions provided by the PQ Corporation held in the porous media and scaled

dimensionally from observations made during the flow-tank experiments (e.g. gelation speed, viscosity increase depending on concentration, reduction of viscosity after gelation). A few other parameters could not be determined and needed to be estimated through calibration with the numerical model (e.g. maximum viscosity increase, dispersivities). Thus, our calibration strategy was to first constrain the variability with the measured parameters. Then, with the help of observed data, we determined one set of calibration parameters that fitted all three experimental setups. Gelation time and fluid density were used to distinguish between the three different solutions. Literature helped to justify the calibrated parameters. Tables 2 - 4 state how the parameters were acquired.

4.6. Geopolymers as slow-release materials for potassium permanganate

Part of our study involves discovering inorganic polymers able to resist oxidation by permanganate. Families of geopolymers exist that can be created from materials rich in aluminum and silicon oxides such as fly ash, metakaolin, blast furnace slag etc. (Heah et al., 2012). Geopolymerization involves a chemical reaction that integrates aluminosilicate oxides and sodium metasilicate solution at highly alkaline conditions occurring at < 70° C into an amorphous to semi-crystalline three dimensional silico-aluminate structures (Davidovits, 2002; Dimas et al., 2009). The process of creating geopolymer starts with the dissolution of solid aluminosilicate materials in strong alkaline aqueous solution. This step leads to the formation and then polycondensation of Si/Si-Al oligomers in aqueous solution initiating the genesis of the core framework structure. Finally, undissolved particles are integrated into final geopolymeric structure (Khale and Chaudhary, 2007; Dimas et al., 2009). Geopolymeric structure is a function of the molar ratio Si:Al which defines the type of geopolymers such as polysialate (Si:Al = 1, -Si-O-Al-O), polysilate-siloxo (Si:Al = 2, -Si-O-Al-O-Si-O-) and polysialate-disiloxo (Si:Al = 3, -Si-O-Al-O-Si-O-Si-O-) (Davidovits, 2002). This three dimensional network is comprised of SiO_4 and AlO_4 tetrahedron linked alternatively by sharing all oxygen atoms (Davidovits, 1991). The positive ions (Na^+, K^+, Li^+, Ca^{+2}, Ba^{+2}, NH_4^+, H_3O^+) act as a charge balancing species for the net negative charge created by AlO_4 (Davidovits, 1991).

The rate of polymer formation is influenced by curing temperature, activator concentration, initial solid content, chemical composition and type of the source material, particle size etc. (Rowles and O'Conner, 2003; Kong et al., 2007; Criado et al., 2007; Dimas et al., 2009). Rowles and O'Conner (2003) quantified the effect the bulk chemical composition of the starting materials on the compressive strength of the geopolymers and observed that the compressive strength maximizes when (i) there is slight excess of Na beyond the assumed Na:Al molar ration of unity required for charge balancing and (ii) when the Si:Al molar ratio is approximately 2.5. Dimas et al. (2009) found that the solubility of geopolymers is a function of SiO_2/Na_2O and Si/Al molar ratios. The solubility of the geopolymer decreases as the SiO_2/Na_2O ratio increases but when Si/Al molar ratio is below 5 then the resulting material is practically insoluble. In this study, we described the preparation of $KMnO_4$ (potassium permanganate) doped geopolymer (PDG) samples and examined the use of geopolymers as controlled-release materials for permanganate through column experiments.

4.6.1. Materials

Metakaolin (PowerPozz white, Advanced Cement Technologies) was produced by the calcination of purified kaolin. The chemical composition and physical characteristics of

metakaolin are given in Table 5. Sodium silicate solution (Na_2SiO_3) (N-Clear, PQ Corporation) had 37.5 weight % solids with SiO_2/Na_2O weight ratio of 3.22. The pH, the specific gravity and viscosity of the N-Clear sodium silicate solution were 11.3, 1.39 g/cm^3 and 180 centipoise at 20ºC, respectively. NaOH pellets with 98.5% purity (Acros Organics) were used in the preparation of alkali activated silicate solutions. Potassium permanganate granules (Cairox-Cr) were supplied by Carus Corporation.

Table 5. Chemical composition (wt %) and physical characteristics of metakaolin used in geopolymers (Advanced cement technologies, 2013).

SiO_2	TiO_2	Al_2O_3	Fe_2O_3	MgO	CaO	Na_2O	K_2O	SO_4	P_2O_5	LOI
51-53	< 3.0	42-44	< 2.2	< 0.1	< 0.2	< 0.05	< 0.4	<0.5	< 0.2	< 0.5

4.6.2. Sample preparation

Three geopolymer samples were prepared with varying $KMnO_4$ concentrations. The alkali activated solutions with the SiO_2/Na_2O molar ratio of 2.8 were prepared by mixing the NaOH pellets with sodium silicate solutions. Metakaolin was added to alkali activated solutions with solids/liquids weight ratio of 0.42 and then the mixtures were stirred manually until no visible lumps of metakaolin remained in the mixtures. Three geopolymer samples (samples 1,2 and 3) with varying $KMnO_4$ concentrations were prepared by adding granular $KMnO_4$ to geopolymer batches in varying amounts and mixed further manually until a visually homogeneous mixture formed. A $KMnO_4$ free geopolymer sample was also prepared by adding 5 g of KCl into the fresh geopolymer batch (sample 4). Fresh pastes were then poured into 3.9 x 6.3 cm (diameter x length) cylindrical molds. The molds were tapped on the counter top until no visible air bubbles left in the samples and were closed on top with plastic caps. The sample was cured at 75° C for 48 hours. Hardened samples were kept at room temperature for 24 hours in their molds. The $KMnO_4$ concentration of the samples used in the column experiments are given in Table 6. The $SiO_2/(Na_2O+K_2O)$, Si/Al and (Na+K)/Al molar ratios as calculated from the starting chemistry are also given in Table 6.

Table 6. Nominal molar ratio compositions of the geopolymer samples.

Sample #	$KMnO_4$ concentration (g/cm^3)	$SiO_2/(Na_2O+K_2O)$	Si/Al	(Na+K)/Al
1	$1.40 \times 10 - 1$	3.95	2.35	1.20
2	$4.63 \times 10 - 1$	2.61	2.35	1.83
3	$6.07 \times 10 - 1$	2.16	2.35	2.21
4	-	4.03	2.35	1.17

4.6.3. 1-D column experiment

Column leaching experiments with these samples were performed to monitor the release of MnO_4^- from the PDG samples. Glass columns (Chromaflex, Kontes) with 4.8 cm inner diameter and 15 cm length were used in the experiments. The lengths of the samples ranged from 5.1 cm to 5.6 cm with an average diameter of 3.65 cm. In order to provide “perfect sink conditions” an ambient flow rate of 22 ml min^{-1} was maintained using Ismatec Ecoline peristaltic pumps.

Reverse osmosis (RO) water used in the experiments. The degree of the ionic rejection, organic rejection and bacteria and particulates rejection of the RO water were > 96%, >99% and > 99%, respectively. The outlet of the glass column was connected to an UV-VIS photospectrometer (Shimadzu UVmini-1240) and the absorbance of the effluent was measured continuously at every 60 seconds at 525 nm wavelength. A five point calibration equation was used to convert measured absorbance data to permanganate concentration.

4.6.4. X-ray Diffraction (XRD) and Scanning Electron Microscopy (SEM) Imaging

SEM and Energy dispersive spectroscopy (EDS) analysis were conducted using the Bruker QUANTAX SEM in the School of Earth Sciences of The Ohio State University. Samples were vacuum dried for one day at 75º C before the SEM imaging. Vacuum drying caused shrinkage cracks on the surface of the samples. Samples were mounted on sample holder using a carbon adhesive tape. The samples were imaged in the low vacuum mode with the chamber pressure at 0.6 mbar and a spot size of 4.5 μm. XRD diffraction analyses of samples involved a PANalytical X'Pert Pro with CuKα radiation also in the School of Earth Sciences of The Ohio State University.

5. Results and Discussion

5.1. Experimental and theoretical studies of convective mixing

This section describes the results of experimental and model studies designed to assess the possibilities of providing slow release of $KMnO_4$ within a zone of reaction using the characteristic behavior of a dense fluid. In effect, if $KMnO_4$ is provided as a dense aqueous solution, its tendency to sink vertically will facilitate mixing with contaminants moving laterally. In the presence of complex heterogeneity, these dense solutions can be sequestered in low permeability units, which could provide a “slow-release” capability.

5.1.1. Results and discussion

The set-up for the two experiments discussed in this section is described in section 4.1. In the first experiment, shortly after the start of the injection the saline water injected to the tank moved downward and accumulated at the interface between the fifth and sixth layer (Mil-10 and Mil-3, respectively).Fingering was manifested a series of small instabilities. As the dense solution moved along this interface toward the withdrawal chamber, the number of these small instabilities increased. These instabilities tended to start up at the small concave structures (i.e. small depressions) that occurred along the interface between the sixth and fifth layer. The accumulation of the dense solution in these micro-depressions created a density difference between the solution and the underlying fresh water promoting downward fluid flow and growth of these instabilities.

The short wave-length instabilities that developed at the beginning of the experiment below the porous injection tube grew and coalesced reducing the number of fingers to one. At the end of the second day, this instability extended downward approximately 6.5 cm (Figure 10a). Secondary fingers developed and grew at the leading face of this major instability while it continued to grow downwards within the fifth layer (Mil-10). As before continued flow within the sixth layer created additional small (~1 cm) instabilities developed along the interface between the fifth and sixth layer.

The density of the dense body of water regulates the downward growth rate of these instabilities. For example, at the end of the fourth day (Figure 10b) the major instability propagated downward to the fourth layer (Mil-13), while the small downstream instabilities coalesced and wavelength grew up to 4 cm. The major instability became wider and sank downward through the Mil-13 and Mil-10 layers at the beginning of the sixth day without hindrance along the interfaces between these layers and reached to the top of the second layer (Mil-3), which had a higher hydraulic conductivity. The dense fluid mixed within this layer and moved laterally and reached the withdrawal chamber at the end of the eleventh day (Figure 10c).

The major instability tended to grow wider in the fifth layer (Mil-10) through time with a less saline leading face. A small instability grew along the leading face of the major instability and moved along the interface between the fifth and fourth (Mil-10 and Mil-13, respectively) layers without sinking downwards into the fourth layer due to its lower salinity. Through time, the number of instabilities that developed at the interface between the fifth and sixth layer decreased as they coalesced, and they became wider and with a maximum amplitude of 10 cm.

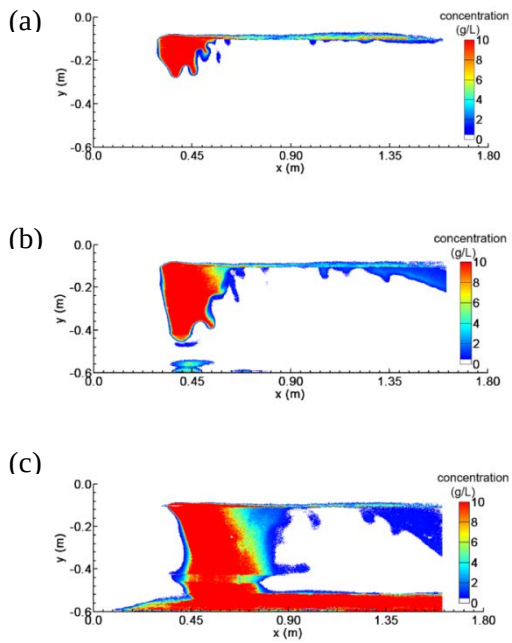

Figure 10. Concentration distribution map experiment-1 (a) day 2, (b) day 4 and (c) day 11.

The results from the first experiment with continuous high and low permeability layers showed that some portion of the saline solution injected into the high permeability continuous layer ended up flowing along that layer without sinking downward into deeper layers. This bypassing reduces the effectiveness of the delivery of the treatment solutions into the contaminated zone. The other disadvantage of this experimental design was that once injected, highly concentrated solutions sank quickly to the bottom of the tank without having much downward resistance to flow. However, the contrast in permeability was not particularly large in this experiment.

The second experiment examined flow behavior in a more complex lenticular media experiment. This porous medium structure was designed to promote convective mixing while slowing down the vertical migration of the tracer plume, thereby increasing the residence time of the treatment chemical in the zone of reaction. Specifically, it focuses on the examination of the flow behavior developed due to discontinuous layers with varying hydraulic conductivity imbedded in a background, low permeability medium (Figure 2b). This medium features a discontinuous high conductivity layer including the injection porous tube, which starts as a horizontal layer and ends as a slightly concave up lens. This concavity possibly could serve as a trap for less saline solutions so that they could accumulate and finally sink to create more pronounced and larger fingers. Additionally, discontinuous lenses of much lower hydraulic conductivity were also included in the system. These lenses were designed to potentially disrupt the sinking dense saline solutions, keeping them in contact as long as possible with the ambient flow in the zone of reaction.

Figure 11 shows the concentration distribution maps at 2.5, 8.5 and 17 days after the injection had started. Concentration distribution map shows that initially the dense solution (i.e. >7.5 g/L) was distributed around the source zone and next to the dipping slope of the discontinuous lens along the Mil-3 and Mil-10 boundary layer. As seen in Figure 11a, at 2.5 days, 3 fingers are evident: 2 larger fingers close to the source zone with concentrations around 5-7.5 g/L and a

wider one further away from the source zone closer to the high concentrated area with concentrations mostly below 5 g/L. After 8.5 days (Figure 11b), the fingers mostly merged, flowing downward until they hit the low permeability lens and moved laterally along and finally around this lens to continue sinking. Beneath the injection zone, concentrations are about 7.5 g/L but when the fluid entered the Mil-13 zone above low permeability lens the concentration had decreased below 5 g/L. This is due to fluid mixing as the dense fluid moves downward and sideways. Away from the source zone, the concentration of the dense plume decreases from about 6 to 0 g/L. At 17 days (Figure 11c), the instabilities merged totally to create a single body fluid whose concentrations decrease from about 9 to 0 g/L in Mil-10 zone with higher concentrations seen under the injection area. Eventually, the dense fluid sank down to the lower Mil-3 layer and moved laterally towards the withdrawal chamber with concentrations below 3 g/L. When they sank, plumes moved laterally along the clay lenses and sank down through the Mil-10 zone.

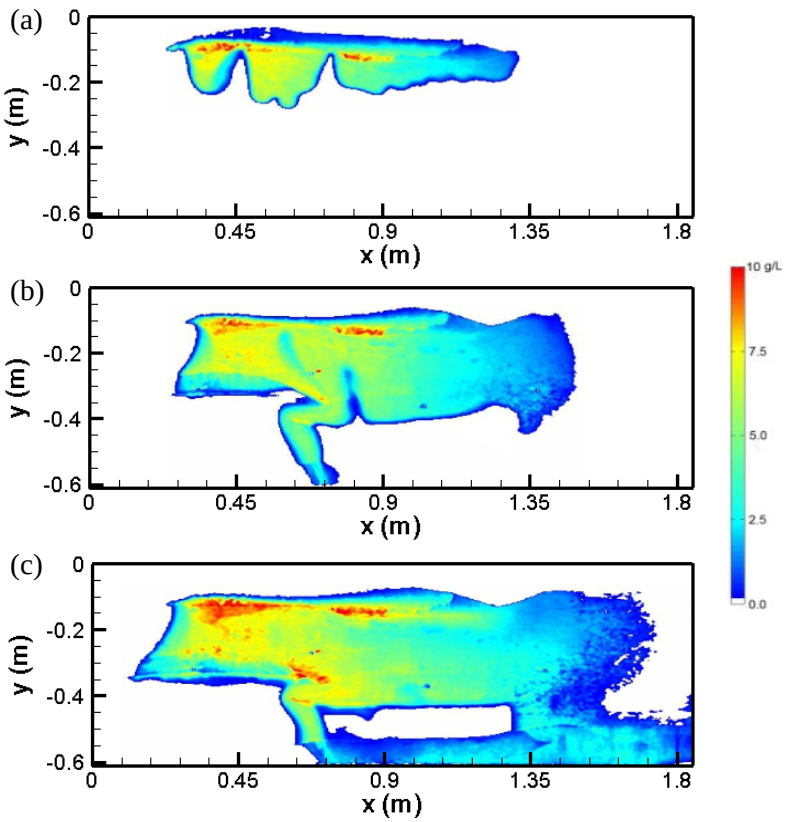

Figure 11. Flow tank experiment with discontinuous high and low hydraulic conductivity lenses. 10,000 mg/L NaCl and 300 mg/L RWT tracer solution was used. (a) Day 2.5, (b) day 8.5 and (c) day 17.

In the second experiment, the delivery of the treatment solutions into the contaminated zone is more efficient due to the discontinuous high permeability lens at the inlet pipe. One advantage of this hydraulic conductivity field is that low permeability clay lenses inhibit the downward sinking of the dense fluid, keeping it in the reaction zone for a longer time. The other advantage is that solutes that are in contact with the clay lens, diffused into the clay lens and created a slow

release system. After several weeks of water injection, the clay lenses were still releasing the tracer.

We modeled these experiments to help interpret and generalize the results of the experiments. Figure 12 shows the simulated concentration distribution for the first experiment at times coinciding with the experimental data presented in Figure 10. Comparison of the experimental data with the simulation results shows that the model satisfactorily simulated the broad character of the variable density flow in terms of the growth of the major finger through time and its internal concentration distribution. However, the simulation did not capture the growth of the small fingers that tended to form along the bottom of the injection layer and the leading front of the large finger. Nevertheless, the shape and the concentration distribution of the simulated plume closely match the experimental dense plume.

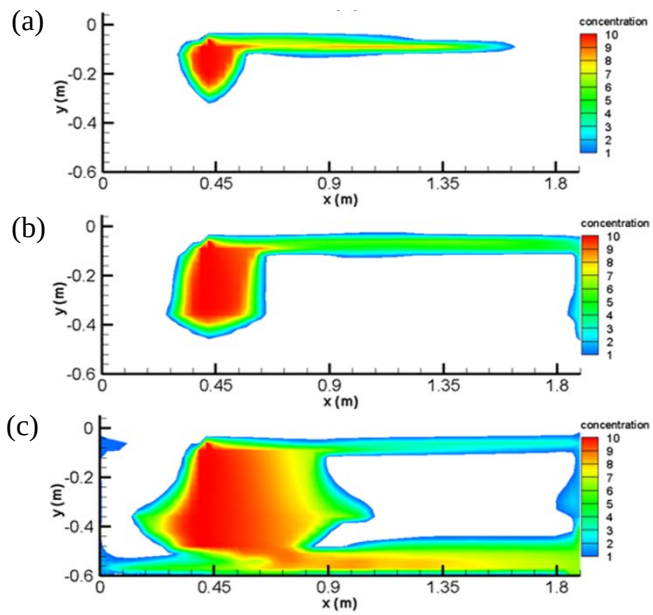

Figure 12. MITSU3D modeling results of the experiment 1. (a) Day 2, (b) day 4, (c) day 11.

In the second experiment, MITSU3D predicted the formation of a finger immediately under the injection zone at day 2.5. The low concentration solution was spread along the discontinuous high hydraulic conductivity lens and created a second small finger (Figure 13a). The experiment showed the development of two broad fingers under the injection zone (Figure 11a). This difference may be due to the non-uniformities in the interface between the Mil-10 and Mil-3 media. Additionally, a broader finger developed at the downstream end of the discontinuous Mil-3 lens which was not quite observed in MITSU3D simulation result at day 2.5 (Figure 13a). At day 8.5 the major plume reached to the bottom high hydraulic conductivity Mil-3 layer. When the plume reached the low conductivity lenses it stopped moving downward and it moved around these lenses to go downward (Figure 11b, Figure 13b). Furthermore, MITSU3d predicted that more dilute smaller finger grew heterogeneously and moved diagonally (Figure 13b). However, this secondary less dense plume grew vertically and merged with the major denser plume (Figure 11b). At the end of the experiment (day 17), MITSU3D showed that the major instability moved laterally and merged with the less dense secondary plume. The secondary less dense plume did not grow vertically as much as it did in the experiment therefore it did not reached to low

conductivity clay lens but it passed the lens and reached to high hydraulic conductivity layer at the bottom of the tank (Figure 13c). These differences may be related to the homogeneous isotropic coarse grid system.

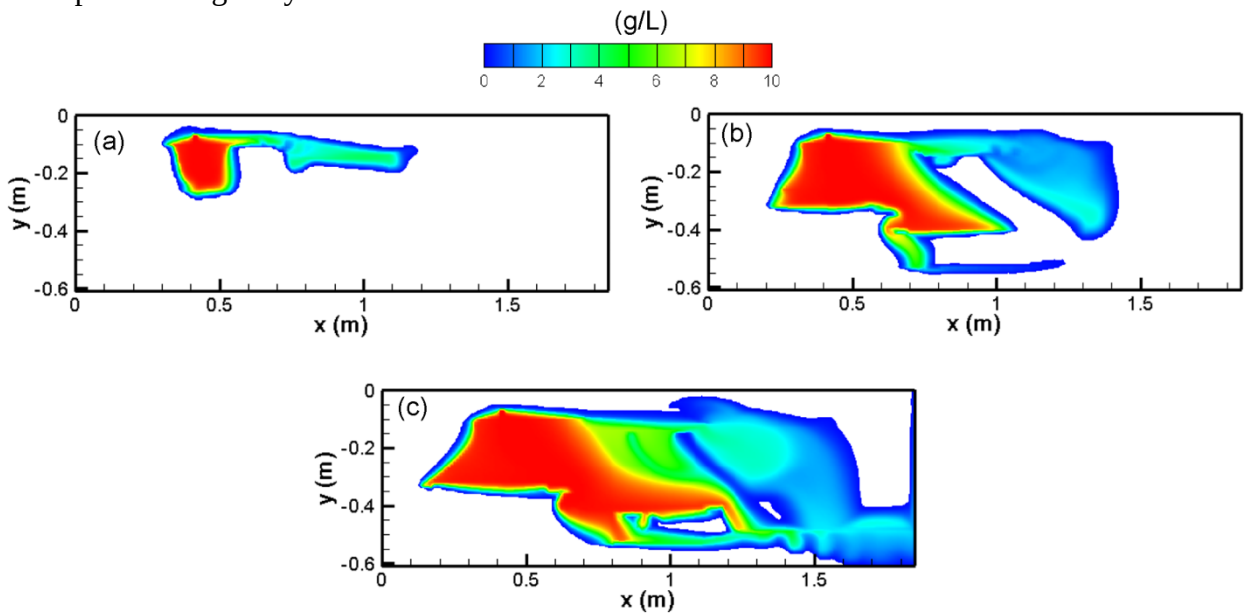

Figure 13. MITSU3D modeling results of the experiment-1. (a) Day 2.5, (b) day 8.5, (c) day 17.

5.2. Permanganate gel (PG) for groundwater remediation: Compatibility, gelation, and release characteristics

Initially, we examined the possibility of using an inexpensive biopolymer, chitosan, as a material to contain the $KMnO_4$. Given the organic character of this material there is always a possibility that the $KMnO_4$ would react with the chitosan, which is not desirable. Thus, in addition to gelation experiments we examined issues of compatibility.

5.2.1. Compatibility and gelation tests

5.2.1.1. Chitosan gel

Chitosan is a 2-amino-2-deoxy(1-4)β-D-glucopyranan obtained from the alkaline deacetylation of chitin in crab and shrimp shells. These are the second most abundant polysaccharide on Earth next to cellulose. Chitosan is water insoluble, but readily dissolves in oxalic, sulfuric and phosphoric acids to form an ionic cross-linked gel (Hamdine et al., 2005). Reactivity of chitosan with KMnO4 was tested. As shown in Figure 14, the experiments showed that MnO_4^- concentrations rapidly decreased in the chitosan gel with essentially negligible concentration after 30 min (Figure 14). The sharp decrease in MnO_4^- concentration may be attributed to an interaction between chitosan and MnO_4^- (Khairou, 2001). Because gelation of chitosan required acidic condition, the proposed mechanism for MnO_4^- reduction may not be directly applicable to the observed decay of MnO_4^- in the acidic chitosan gel. Oxidation of chitosan by MnO_4^- in a perchlorate solution has also been reported in the literature and could provide a useful analogy (Ahmed et al., 2003):

$$5C_6H_{11}O_4N + 8MnO_4^- + 24H^+ \leftrightarrow 5C_6H_4O_6 + 5NH_3 + 8Mn^{2+} + 22H_2O \quad (17)$$

where $C_6H_{11}O_4N$ and $C_6H_4O_6$ represent chitosan and diketo-acid derivatives, respectively. While this reaction could be similar to the reaction observed in the acidic chitosan gel of this study, reaction between MnO_4^- and oxalic acid has also been reported and could explain the MnO_4^- reaction observed in this study (Launer, 1932):

$$5C_2H_2O_4 + 2MnO_4^- + 6H^+ \leftrightarrow 2Mn^{2+} + 10CO_2 + 8H_2O \quad (18)$$

Figure 14. Permanganate concentrations in chitosan gels.

It is difficult to determine the overall rate of this reaction, due to the creation of numerous intermediate products. However, an initial rapid decrease in MnO_4^- concentrations was observed during the first 20 min, followed by slower rate of decrease in concentrations. This observation is in keeping with observations of Lidwell and Bell (1935), which showed a significant initial decrease in concentrations by a rapid reaction, which was followed by subsequent slower concentration decrease by slower reaction. Permanganate concentrations in the chitosan-sulfuric acid gel rapidly decreased from 2,000 to 610 mg L^{-1} within 3 min, and then gradually decreased to 410 mg L^{-1} over the next 57 min (Figure 14). There is no documented reaction between MnO_4^- and low concentration sulfuric acid in the literature, thus the rapid loss of MnO_4^- was attributed to an interaction between MnO_4^- and chitosan gel. Due to the organic nature of chitosan and the significant oxidizing capacity of MnO_4^-, rapid loss of the MnO_4^- ion, and thus chitosan gel, is not really surprising. Similar results have also been observed between MnO_4^- and other organic gels such as alginates and pectates (Khairou, 2001; Abdel-Hamid et al., 2003). These data suggest that chitosan gels, and also other organic gels, are not compatible with MnO_4^-, and thus cannot be used for the proposed PG scheme.

5.2.1.2. Aluminosilicate gel

The poor performance of chitosan as gel-matrix for $KMnO_4$ and an examination of the literature on the similar reactivity of other biopolymers prompted us to more to geopolymers.

Aluminosilicate gels, also known as zeolite gels, are formed through a sol-gel process in which an initial colloidal precursor or sol is mixed and allowed to set until it bonds to form a gel. The sol-gel processing of aluminosilicates occurs through a hydrolysis and a subsequent condensation reaction. Aluminosilicate gels have variable compositions depending on types and amounts of precursors used. Properties such as acid resistance, thermal stability, hydrophobicity and pore size can be altered by precursors (Hamdine et al., 2005).

When $KMnO_4$ was mixed with aluminosilicate gel there was much less interaction. While there was a small initial decrease, MnO_4^- concentrations remained fairly constant during the 2-h testing period (Figure 15) suggesting its compatibility with MnO_4^-. The initial decrease in MnO_4^- concentrations was attributed to the alkaline nature of the aluminosilicate gels, and the resulting speciation of manganese. During long-term monitoring of the aluminosilicate/MnO_4^- mixture, however, it was noted that the MnO_4^- was immiscible with the aluminosilicate gel. The permanganate solution apparently stayed on top of the gel media (Figure 16). This was attributed to the unique molecular structure of aluminosilicate gel. The aluminosilicate gel formed with the precursors used in this study was Linde Type A (LTA) or zeolite A. This type of aluminosilicate typically has an extremely small cell volume of 1693.24 $Å^3$ (1.69×10^{-21} cm^3) (Subhash, 1990) created by the gel network, which would provide little space for mixing with $KMnO_4$.It was found that the gel was only able to contain a small quantity of $KMnO_4$. These observations suggested that aluminosilicate gels cannot be applied to the proposed permanganate gel scheme.

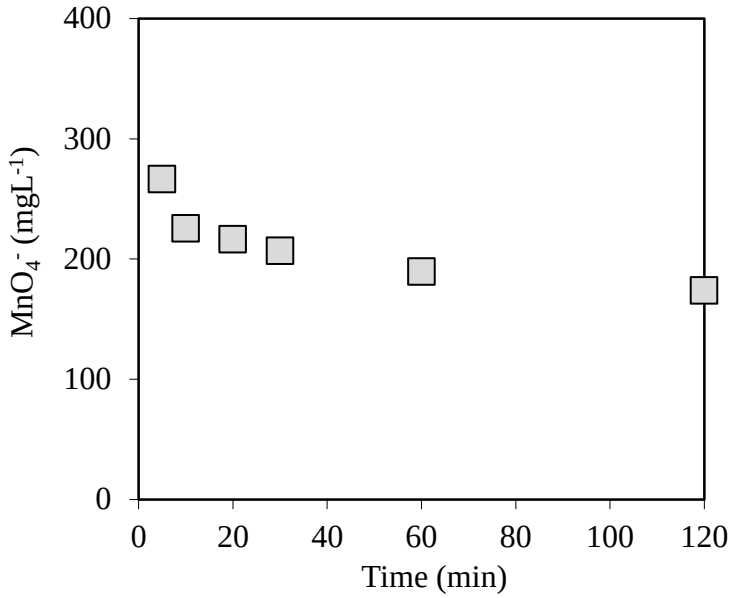

Figure 15. Permanganate concentrations in aluminosilicate gels.

Figure 16. Photo showing $KMnO_4$ solutions in aluminosilicate gel.

5.2.1.3. Silicate gel

Silicate gels are derived from soluble silicate glasses. The anionic structure of silicate gels ranges from monomers to cubic octamers, and depends on silica to alkali ratio and ion concentrations. Similar to aluminosilicate gels, there was a slight initial decrease in MnO_4^- concentrations in the Kasil 6 silicate gel/$KMnO_4$ mixture (Figure 17). This was attributed to the alkaline nature of the silicate gels, and the resulting speciation of manganese. However, the decrease in MnO_4^- concentration was not substantial and remained generally constant over the entire testing period of 240 hours (10 d), suggesting that silicate gels are unreactive with MnO_4^-.

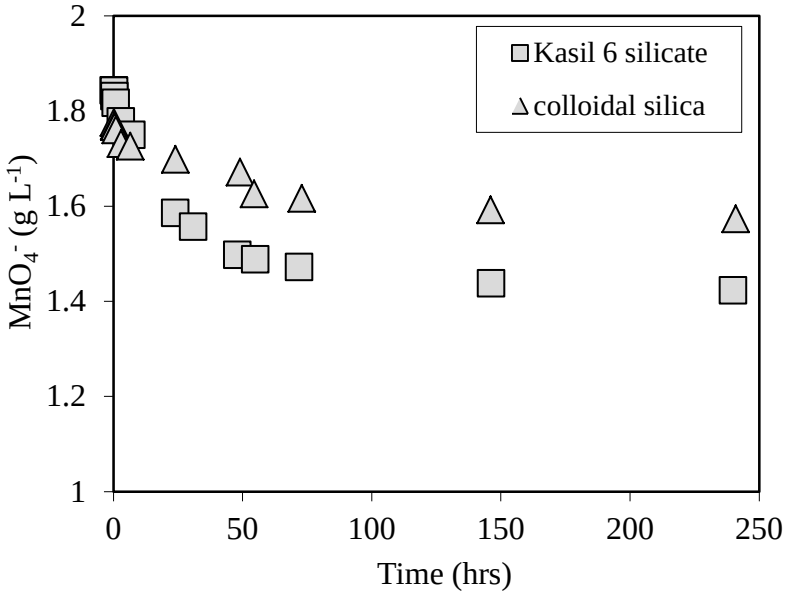

Figure 17. Permanganate concentrations in Kasil 6 silicate gel and colloidal silica gel.

Silicate solutions are created with a special initial viscosity, ranging from 40 to 2,100 cP. The viscosity can be altered with the addition of salts or acids (PQ, 2003). To monitor effects of addition of salts on silicate viscosity, $KMnO_4$ granules were added to silicate solution with low viscosity (44 cP). Viscosities gradually increased with increasing amount of $KMnO_4$ granules,

reaching 69 cP with addition of 2 g $KMnO_4$ (Figure 18a). However, when a saline solution of $KMnO_4$ (60 g L^{-1}) was added to the silicate solution with a high initial viscosity, the viscosity decreased with increasing volume of $KMnO_4$ solution (Figure 18b). For Kasil 6, the initial viscosity of 1,068 cP was rapidly lowered to 97 cP when the volume of the added $KMnO_4$ solution comprised 5% of the total volume. Afterwards, viscosity gradually decreased to 61 and 46 cP when the $KMnO_4$ solution comprised 7.5% and 10%, respectively (Figure 18b). Unlike Kasil 6 silicate, Ru Na silicate showed more attenuated decrease in viscosity. The initial viscosity of 2,800 cP gradually decreased with increased volume of $KMnO_4$ solution. The viscosity reached a minimum value of 43 cP when the volume of $KMnO_4$ solution comprised 50% of the mixture (Figure 18b). These observations suggested that the addition of $KMnO_4$ solution resulted in the dilution of the viscous silicate gel, lowering the viscosity.

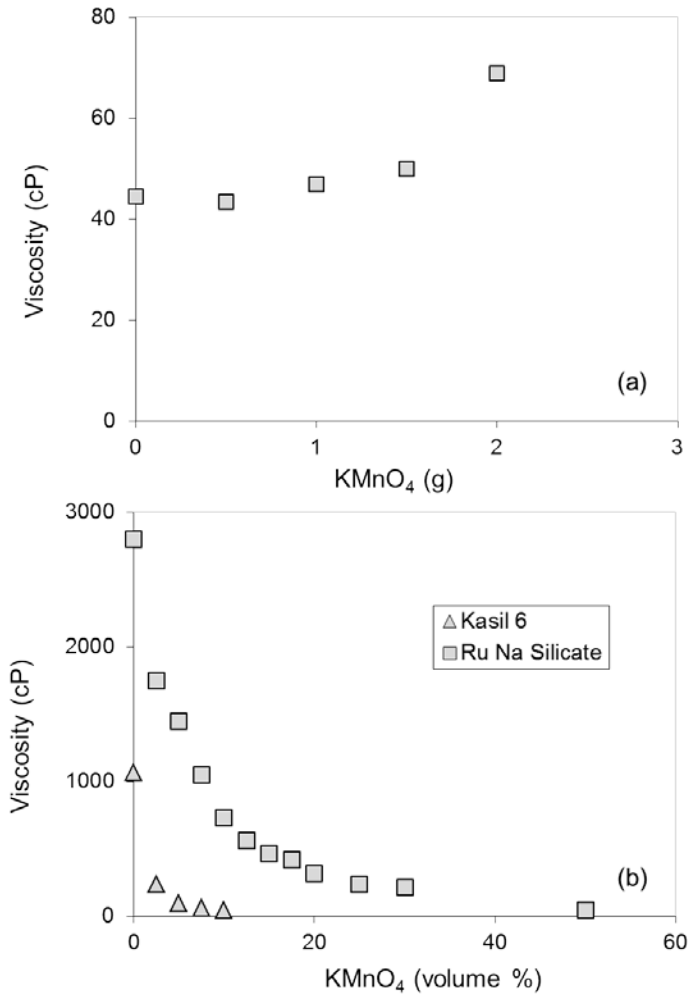

Figure 18. Viscosities of (a) Kasil 1 silicate gel with addition of granular $KMnO_4$ and (b) Kasil 6 silicate gel and Ru Na silicate gel with addition of 60 g L^{-1} $KMnO_4$ solution: volume ratios (%) of $KMnO_4$ solution in the total volume of solution (silicate gel + $KMnO_4$ solution).

The initial viscosity of the permanganate gel solution is desired to be low, because the proposed permanganate gel scheme would use well-based injection to facilitate spreading of the solution. The exact range of silicate viscosities appropriate for well-based injection is unknown, but soil

liquefaction studies suggested that a viscosity below 4 cP would be desired for low-pressure injection into a purely sandy medium (Gallangher and Lin, 2009).The viscosity of the silicate gel was lowered by addition of saline MnO_4^- solution (60 g L^{-1}) or increased by addition of salts (Figure 18). These data suggested that silicate can be used to develop permanganate gel if setting agents able to delay the gelation of silicate-based MnO_4^- solution are available.

5.2.1.4. Colloidal silica gel

Colloidal silica contains nanoparticles of amorphous silicon dioxide and sodium hydroxide suspended in an aqueous solution. The gelation of colloidal silica is constrained by pH, solid contents, or ionic strength of the solution. Colloidal silica has been commonly used as a stabilizing agent in areas that have high risk of soil liquefaction due its capability to gel (e.g., Gallagher et al., 2007b).

When $KMnO_4$ is mixed with an aqueous solution of colloidal silica concentrations of MnO_4^- did not change significantly over 240 hours (10 d). This result indicates that colloidal silica is chemically compatible with MnO_4^- (Figure 17). Subsequent, viscosity tests yielded promising results in terms of delaying gelation, which is desired for the proposed PG scheme (Figure 19). When 3.75 g $KMnO_4$ granules were added to 150 mL of colloidal silica, viscosity did not increase until after 200 min, when it exponentially increased to 2,000 cP. Addition of 4 g $KMnO_4$ produced a less marked delay in gelation, with no increase in the viscosity until after 100 min when viscosity increased to 54 cP. Viscosities then exponentially increased to 773 cP at 135 min, before reaching a maximum of 4,000 cP over the next 5 min. The addition of 7.5 g $KMnO_4$ provided an almost immediate increase in viscosity. These data suggest that colloidal silica may possess the delayed-gelling properties necessary for development of a in-situ, slow-release material. Release tests were performed with the two promising gels, silicate and colloidal silica gels.

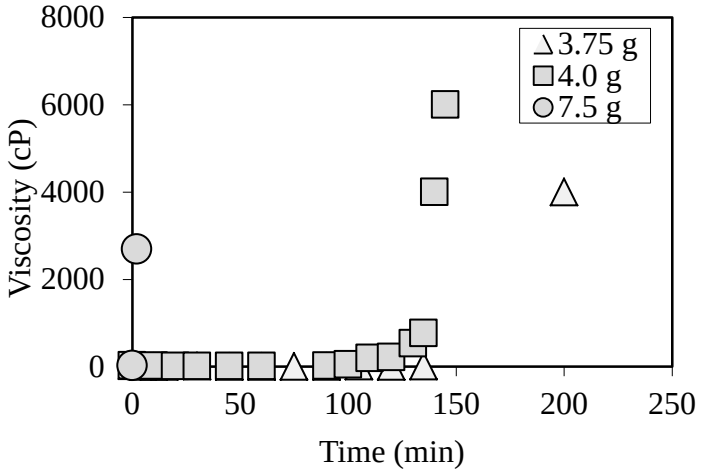

Figure 19. Viscosities of colloidal silica with addition of granular $KMnO_4$. 3.75 g, 4 g, and 7.5 g of $KMnO_4$ granules were added to 150 mL of colloidal silica, respectively.

5.2.2. Release tests

Release data for silicate gels with bentonite, $Ca_3(PO_4)_2$ and portlandite as setting agents are presented in Figure 20. All three silicate gels yielded similar release patterns, with maximum concentrations evident after 2 h followed by exponential decline in concentration. These results suggest that using different chemical hardeners had little effect on the MnO_4^- release behaviour of the silicate gels. In addition, MnO_4^- concentrations in the effluent water became negligible after 8 h, with no residual material remaining in the column. These data suggested that silicate gel may not provide an appropriately low release rate due to its solubility in water.

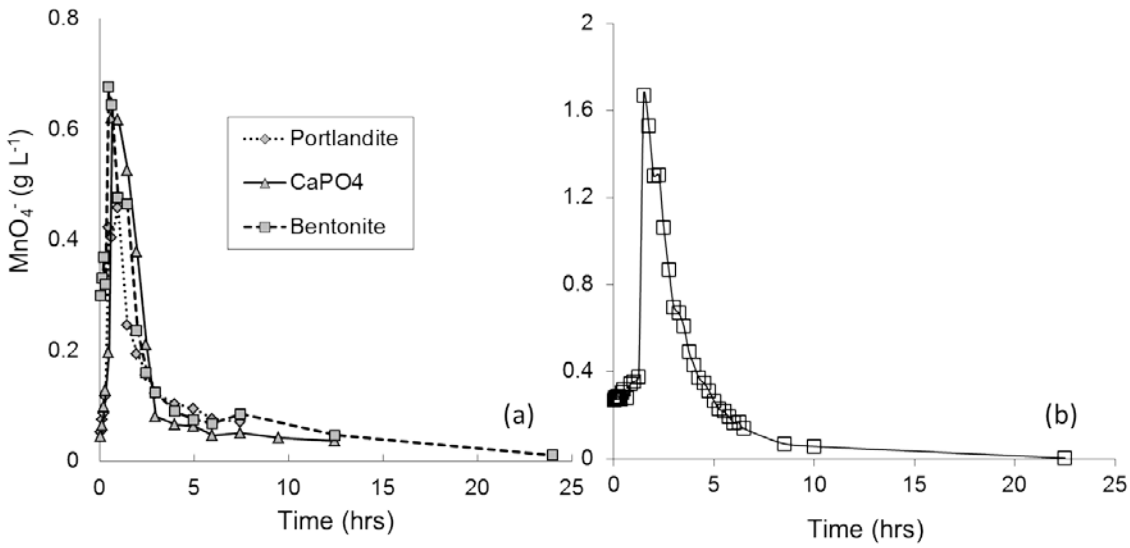

Figure 20. Temporal changes in MnO_4^- concentrations in the effluent samples of the glass column containing (a) silicate-based PG gel and (b) colloidal silica-based PG gel.

The addition of salts can alter the ionic strength of the colloidal silica solution and promote gelation (Gallagher et al., 2007a). For this study, $KMnO_4$ was added to colloidal silica as such a salt. A smooth, glass-like surface was observed once the colloidal silica/$KMnO_4$ solution solidified. Temporal changes in MnO_4^- concentrations in the effluent samples of the glass column were observed (Figure 20). An initial concentration spike (1.67 g L^{-1}) was reached after 90 min. The delay in concentration spike is an indicative of diffusion-controlled release of MnO_4^- from the colloidal silica matrix material. The concentration of MnO_4^-, however, became negligibly small after 24 h, with the majority of the mass being released by 10 hours. The slightly extended release duration compared to silicate gel was attributed to the lack of matrix solubility. Thus, a large portion of the matrix material remained after the cylinder was depleted of MnO_4^- (Figure 21). The short duration of release was attributed to the small amount of $KMnO_4$ (1 g) in the gel.

Figure 21. Photo showing the remaining colloidal silica matrix (left column) after MnO_4^- is released.

5.3. Harnessing the complex behavior of ultra-dense and viscous treatment fluids as a strategy for aquifer remediation

5.3.1. Results and Discussion

We present illustrative results that show how modelling is being used to understand processes, to interpret the results of laboratory experiments, and to shed light on the three remedial concepts. Much is known both experimentally and theoretically concerning the migration of dense plumes in unstable configurations that lead to instability development. As will be evident, most of our experimental results are manifested by the formation of instabilities. In modelling practice, such instabilities are difficult to create in a realistic manner (Schincariol et al., 1994; Ibaraki et al., 2000). Previous studies (Schincariol et al., 1994) suggest that explicit creation of instabilities is unnecessary in heterogeneous media because the heterogeneity disrupts their formation. We explore this behaviour using experimental results from Schincariol and Schwartz (1990). In addition to the saline solutions used in the experiments of Schincariol et al. (1993), experiments were done utilizing dense and viscous silicate solutions and the gelling silicate solutions. The goals of these experiments were to illustrate and understand the flow and the release behaviour of these solutions. Finally, the release of permanganate from the silicate gels by the diffusion mechanism was discussed.

5.3.1.1. Saline solutions

A photograph of 10 g/L experiment was processed using the method described by Schincariol et al. (1993). The results of the image analysis provided the concentration distribution (Figure 22a) that was used as the calibration target for the simulations (Figure 22b). The experimental plume was simulated reasonably well with the prominent features similar. For the most part, the lateral extent of both plumes matched well.

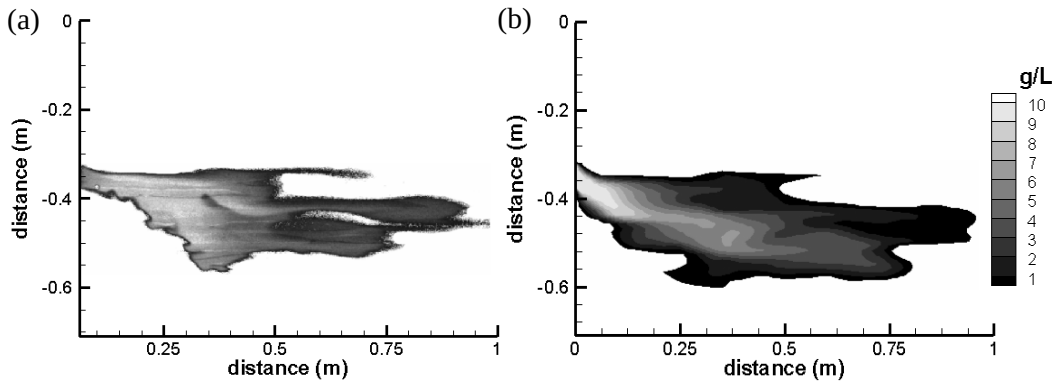

Figure 22. Experimental results (a) with simulation results (b) for 10 g/L after 2 days. Plume concentrations below 0.5 g/L were not plotted for the experimental or the simulated plumes.

The experimental plume sank 7.3 cm further than the simulated plume. Moreover, the experimental plume began sinking about 14 cm sooner than the modelled plume. These problems might be attributed to 3D effects within the experiment flow tank. These 3D effects could either be caused by the solute plume moving differently in the unobservable middle of the tank or slight imperfections in lens construction (i.e. the lenses may not be the same shape throughout).

The pattern of heterogeneity clearly influences the pattern of migration of the dense plume. Much of the transport was through lenses with high intrinsic permeability and a relatively high hydraulic conductivity background matrix. The lower conductivity lenses tended to divert or partition the flow. This phenomenon produced the obvious patterning of concentrations in the plume and the tendency for preferential migration along certain axes of spreading (Figure 22). When dense solutions were evident in the lower conductivity lenses, it is likely that density-driving forces rather than advection alone were responsible. This result is significant in the context of a remediation system because it suggests that dense fluid can be sequestered in low permeability lenses, which could potentially provide a long-term source of remediation chemicals.

Indications in the simulation results are that no obvious instabilities developed in time. Nothing special was done to trigger their growth, nor did they generate spontaneously because of the porous medium structure. This result is in keeping with the results of the experiment. It appears that this heterogeneous structure of the porous medium tended to severely minimize the growth of instabilities. This result suggests that in some cases this process is a second order effect.

5.3.1.2. Dense/viscous fluids

Silicate solutions are inorganic, non-toxic chemical grouts that have been used for geotechnical applications such as soil stabilization. They are considered to be free of health hazards and environmental effects (PQ Corp., 2011). We postulate that the use of silicate solutions can help remediation in two ways. First, they can be used as a delivery medium for transporting oxidants into deeper portions of the aquifer due to their high density. Also, the aquifer heterogeneity provides an in-situ long term source of oxidants. Second, the silicate permanganate solution would create a viscosity much greater than water. This could effectively reduce the hydraulic conductivity aiding in sequestration.

The silicate solution could be injected into the uppermost high conductivity layer but the delivery of this solution had limitations due to its high viscosity. Once it was delivered, pooling occurred. This is due to the high viscosity of the silicate solution close to the injection zone. The silicate solutions then sank slowly and the concentrations of the viscous solutions decreased significantly in relatively short distances due to the dilution of the solution. There were small undulations at this boundary between the high conductivity layer and the low conductivity layer below, which caused pooling of the solutions and their subsequent sinking. The presence of such undulations triggered the development of instabilities. As instabilities grew and sank further down, their concentrations decreased due to dilution. After 6 hours, the plume entered the lower high conductivity layer. Then, diluted solutions spread laterally in this layer (Figure 23a).

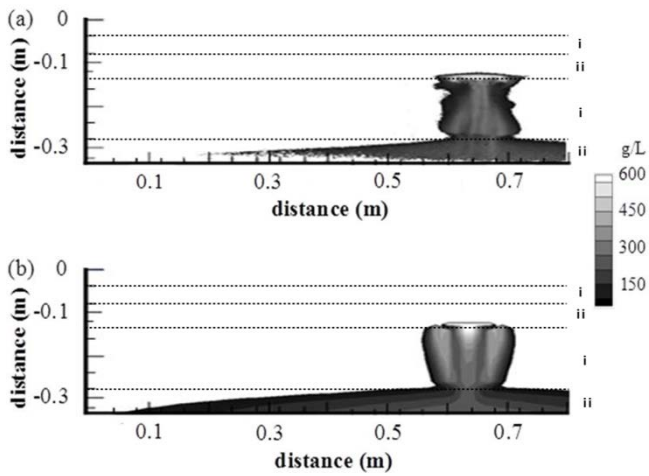

Figure 23. Comparison of dense, viscous fluid experimental (a) and simulated (b) plumes, after 8 hours. Plume concentrations below 60 g/L are not shown for either experimental or simulated plumes. i and ii represent hydraulic conductivities of $1.6 \cdot 10^{-4}$ and $2.9 \cdot 10^{-3}$ m/sec, respectively.

We modelled the experiments involving the viscous solution using MITSU3D, which requires new equations to represent the density and viscosity of the silicate solutions. Published properties of sodium silicate solutions (PQ Corp., 2011) with a SiO_2 to Na_2O weight ratio equals to 3.22 yielded the following concentration-dependent equations developed for solving viscosity and density in order to model viscous fluid experimental results:

$$\rho = 0.7463c + 998.2 \tag{19}$$

$$\mu = 0.001 \cdot e^{0.003481c} + 2.383x10^{-6} \cdot e^{0.02149c} \tag{20}$$

where ρ is the density (kg/m^3), μ is the dynamic viscosity (Pa sec) and *c* is the concentration (kg/m^3) of the sodium silicate solution.

Modelling of the dense viscous fluid was successful in reproducing the shape of experimental plumes, especially in later times. For instance, the modelled plumes at 8 h had only slight and negligible differences in shape from the corresponding experimental plumes (Figure 23b). This experiment suggests that silicate solutions can be useful in delivering oxidants to the deeper zones of contaminated aquifers.

5.3.1.3. Time-delayed gelling

Silicate solutions are stable at high pHs (i.e. pH > 11) but once the pH of the solution is lowered, the solubility of the silica is reduced and it polymerizes. Many chemical compounds modify the pH and can be used as setting agents. However, most of these compounds result in permanent gels, with the exception of bicarbonate (PQ Corp., 2011). We used this idea to prepare a time-delayed gel that serves as a slow-release material in-situ for delivering oxidants such as permanganate. This concept, in theory, would facilitate the initial emplacement of the treatment chemicals in wells to ultimately provide a slow release, reactive barrier. The results of preliminary experiments illustrate the potential of this approach and the modelling challenges involved.

5.3.1.3.1. Small flow tank experiments

In the first experiment, a high conductivity layer which was sandwiched between two lower conductivity layers (Figure 24). The high conductivity layer was flooded with the gelling solution with 300 mg/L RWt dye and parts of the higher conductivity layer had a solution capable of gelling (Figure 24a). Because this solution was more viscous than water, downward flow into the lower layers was slow. Some portions of this solution sank below before gelling. The diffusion of the tracer from the gel was slow. After 20 days, less than 60% of the initial tracer concentration left in the gelled zone (Figure 24b). This experiment showed the potential for creating a slow-release material that releases the necessary oxidants into the reaction zone through time. There is a transition in the behaviour of the gelled material that behaves more like a solid than a liquid.

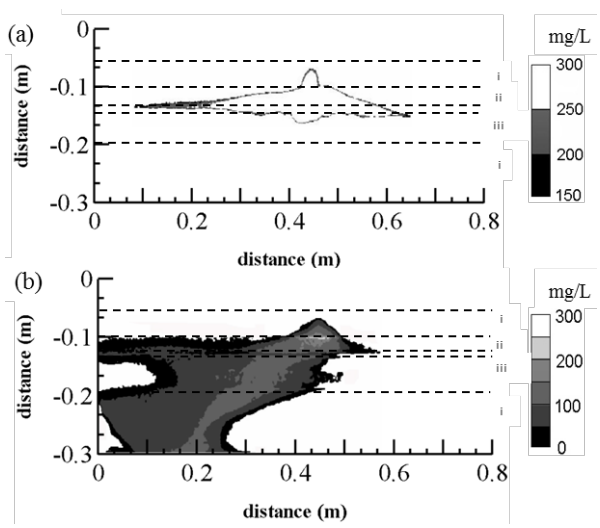

Figure 24. Concentration maps for the time-delayed gelling experiments representing the RWT concentrations. The image analyses procedure of McNeil et al. (2006) was followed. (a) Immediately after injection of the solution into 3 cm thick high conductivity layer, (b) 20 days after the injection. i, ii and iii represent hydraulic conductivities $1.6 \cdot 10^{-4}$, $2.9 \cdot 10^{-3}$ and $5.0 \cdot 10^{-5}$ m/sec, respectively.

In the second experiment, the gelling solution with $KMnO_4$ was injected both over the clay lens and into the high conductivity lens. The $KMnO_4$ solution sank downward due to its high density before the gelling was complete and penetrated into the clay lens along a micro crack (Figure 25a). Initially, there was a slight oxidation of the media above the gelling solution indicated by the light brown color. 2 days after the injection, the solution diffused into the clay layer changing its color and the oxidation rim within the high conductivity layer became extensive (Figure 25b). The amount of $KMnO_4$ in the gel above the clay lens got lower. The $KMnO_4$ solution released from the high conductivity lens sank further downward but the lateral spreading of the solution within the low conductivity unit was not extensive. There was a significant discoloration of the high conductivity unit below the sinking $KMnO_4$ plume (Figure 25b). 13 days after the injection, the gel above the clay lens got almost depleted with $KMnO_4$ but the outline of the gel was still visible. An extensive discoloration of the high conductivity media and clay lens was the result of the oxidation of the glass beads with $KMnO_4$ (Figure 25c). The $KMnO_4$ depletion from the gel within the high conductivity lens became more extensive and the light colored rim around the gel was visible. The intensity of the KMnO4 plume under the gel got lower as the pink color of the solution became lighter. The extensive light brown color of the high conductivity media was extensive (Figure 25c). After a month, almost all of the $KMnO_4$ got released from the gel leaving behind a whitish gel residue in the high conductivity lens and the significant discoloration of the high conductivity unit (Figure 25d).

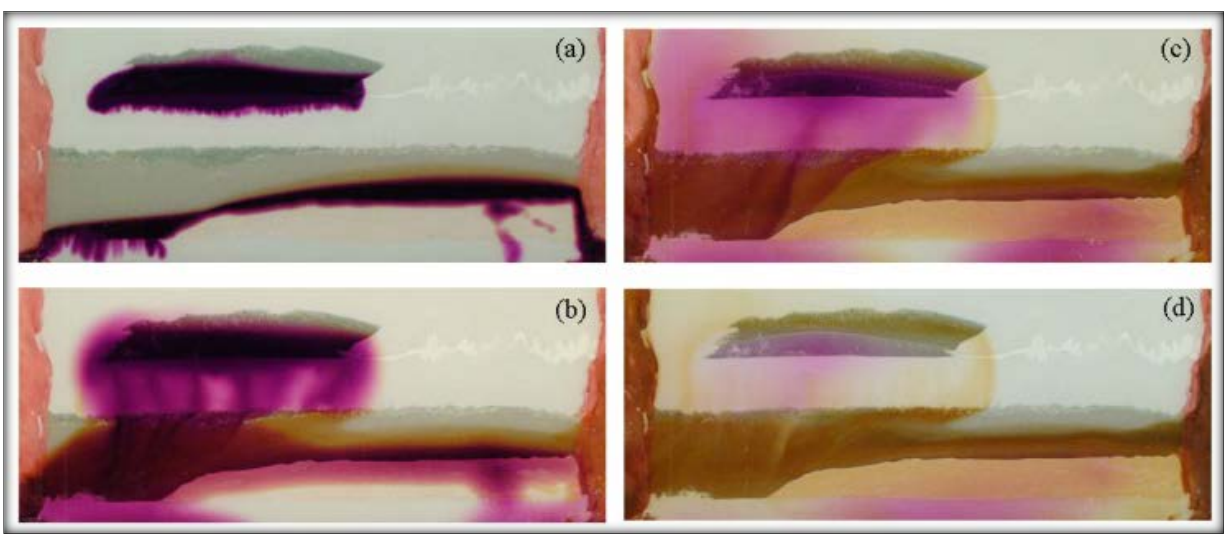

Figure 25. The release of the $KMnO_4$ bearing solution from the gelled silicate solution. (a) 1.5 hour after the injection of the gelling solution over the clay lens, (b) 2 days after the injection, (c) 13 days after the injection, (d) 31 days after the injection. Darker tones (high conductivity media), lighter tones (low conductivity media).

5.3.1.3.2. Large flow tank experiments

In the big flow tank experiment, a heterogeneous set up was constructed. This set up was a combination of a high conductivity lens and high and low conductivity layers. Low conductivity

layers included a clay rich layer. The gelling solution including 300 mg/L RWt was injected into the high conductivity lens first and then into the high conductivity layer above the clay rich layer. As a test, a small portion of the solution was injected into the low conductivity unit below the high conductivity lens shown as a pink circle (Figure 26a).The injection of the solution was easy into the low conductivity unit. The ungelled portion of the solution sank downward creating numerous fingers (Figure 26a). Fingers got bigger as they sank further downward and they reached to the high conductivity layer at the bottom of the tank. A small portion of the solution diffused into the clay layer and released into the low conductivity layer above the gelled solution (Figure 26b). 11 days after the injection most of the dye was released upwards from the gel invading both the low and high conductivity layers (Figure 26c). The remaining blank gel could be observed as a light colored residue. The concentration of the dye got lower in the bottom gel and the dye solution invaded the layers under the bottom gel. It was still possible to observe fingers developing beneath the bottom gel (Figure 26c). Almost no dye left in the upper layers except the right hand side of the flow tank 38 days after the injection and the outline of the remaining blank gel was visible (Figure 26d). The dye concentration of the lower gel got further down and the remaining gel got smaller compared to the initial gel. Finally, the number and the size of the fingers developed under the bottom gel got smaller (Figure 26d).

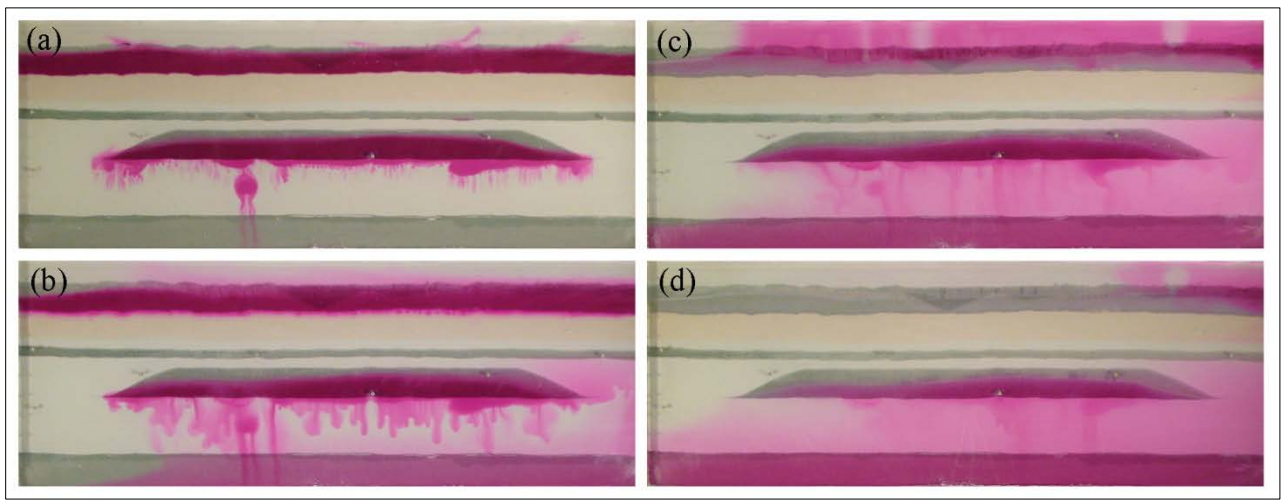

Figure 26. The release patterns of RWt dye from the gelled solutions. (a) Right after the injection of 8 L of solution, (b) 3 days after the injection, (c) 11 days after the injection, (d) 38 days after the injection. Dark tones (high conductivity material), light tones (low conductivity material).

5.3.1.4. Permanganate release from silicate gels by diffusion

We consider one dimensional, diffusional release from a thin slab of the silicate hydrogel of thickness 0.8 cm. The gel had uniform permanganate concentration and its radius didn't change during the experiment. Assuming constant diffusion coefficient with one-dimensional diffusion in the x direction, Fick's second law, along with the appropriate initial and boundary conditions, is written as:

$$\frac{\partial c}{\partial t} = D\frac{\partial^2 c}{\partial x^2} \tag{21}$$

where

$$t = 0 \quad -\frac{L}{2} < x < \frac{L}{2} \quad c = c_0 \tag{22}$$

$$t > 0 \quad x = \pm\frac{L}{2} \quad c = 0 \tag{23}$$

The solution to Fick's law in the form of a trigonometric series under the above specified conditions is (Crank, 1975):

$$\frac{M_t}{M_\infty} = 1 - \sum_{n=0}^{\infty} \frac{8}{(2n+1)} \times \exp\left(-\frac{(2n+1)^2.\pi}{L^2} \times D \times t\right) \tag{24}$$

where M_t is the amount of permanganate released at time t and $M_\infty$is the amount of permanganate released as time approaches infinity. For small time steps, this equation is reduced to:

$$\frac{M_t}{M_\infty} = 4\left(\frac{Dt}{\pi L^2}\right)^{0.5} \tag{25}$$

The short time approximation is valid for the first 60% of the total release. For diffusion from one surface the above equation changes to:

$$\frac{M_t}{M_\infty} = 2\left(\frac{Dt}{\pi L^2}\right)^{0.5} \tag{26}$$

Figure 27 shows the percent release for 50 wt % silicate hydrogels with respect to square root of time. The model estimates the diffusion coefficient as 2.53 x 10^{-6} cm^2/sec for 50 wt % silicate hydrogels. The diffusion coefficient of permanganate in dilute aqueous solution is 1.632 x 10^{-5} cm^2/sec (Vanýsek, 2014) which is about 85 % higher than the calculated diffusion coefficient.

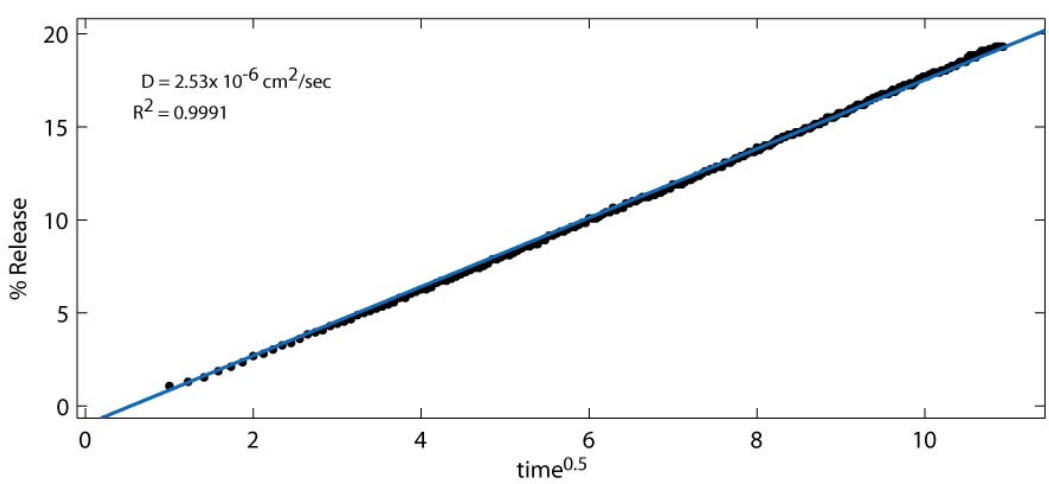

Figure 27. Permanganate release from silicate hydrogels with 50 wt % silicate solution.

5.4. Development and characterization of slow-release permanganate gel (SRP-G) for groundwater remediation

5.4.1. Results and discussion

5.4.1.1. Gelation and release characteristics of SRP-G in water

In a recent study, Lee et al. (2013, under review) demonstrated that SRP-G gelation exhibits a characteristic two-phase increase in viscosity: a lag phase characterized by a small increase in viscosity followed by a gelation phase during which the viscosity increases rapidly to gel solidification. The results of gelation batch tests further demonstrated the delayed gelling characteristics of colloidal silica. In addition, the gelation lag times increased from 0.5 h to 13 d when $KMnO_4$ concentrations were decreased from 25 g L^{-1} to 8 g L^{-1} (Figure 28). Gelation of colloidal silica is primarily governed by the kinetics of the sol-gel process, and these kinetics are affected by a number of factors, predominantly ionic strength and pH and, to a lesser extent, silica concentration, particle size, and temperature (Iler, 1979). Gelation test results indicated that gelation lag times can be modified by manipulating ionic strength. In particular, gelation lag times exponentially increased from 5.5 d to 8.5 d when $KMnO_4$ concentrations were decreased from 9 to 8 g L^{-1}, suggesting the existence of a 'threshold' concentration below which small changes in ionic strength can result in large changes in gelation lag times. The 'threshold' concentration for the gelation test of the current study appears to be ~16 g L^{-1}.

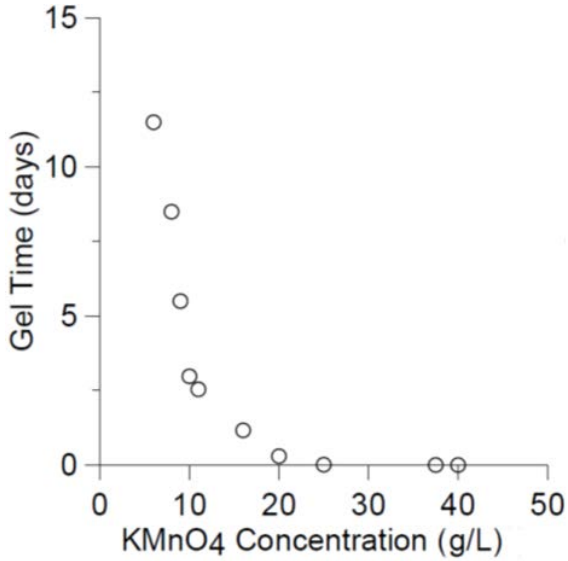

Figure 28. Effects of $KMnO_4$ concentrations upon gelation lag times.

Silica sols bear a slightly negative charge when stabilized at high pH and a slightly positive charge when stabilized at low pH. Therefore, sols are stabilized at high pH (9 - 10) and at low pH (1 - 2) and exhibit maximum gelation rates at neutral pH or on the slightly acidic side of neutrality (e.g., Carman, 1940). Gelation rates occurring from pH 2-6 are considered maximum (slightly acidic side of neutrality). The colloidal silica solution used in the present study was stabilized at pH 10.4 and, thus, bears a slightly negative charge. Stabilization at pH 10.4 was considered ideal because injecting a highly acidic SRP-G solution (pH = 1 - 2) into natural water

is not considered optimal, and high pH on can cause a localized effect on aquifer constituents due to the high density of the hypersaline SRP-G solution and the limited dilution afforded by ambient groundwater flow.

The cation of the salt of interest, K^+ for $KMnO_4$, is considered primarily responsible for the colloidal solution's gelation. This mechanism is expected to be modified in the presence of natural water due to the presence of additional naturally occurring cations (Na, Ca, Mg). The effects of other cations on gelation were not investigated in the present study. However, groundwater salinity has been reported to have no "detrimental" effects on the gelation of colloidal silica grout, though gelation times must be assessed using site water (Allen and Matijevic, 1969; Gallagher et al., 2007b).

A study by Lee et al. (2013, under review) reported that the duration of MnO_4^- release from gelated SRP-G was less than 24 h, with most MnO_4^- release occurring within the first 10 h. This short duration of release was attributed to the small amount of $KMnO_4$ (1 g) in the gel. In the present study, release rates of gelated SRP-G cylinders containing variable $KMnO_4$ concentrations (9 - 20 g L^{-1}) were monitored. Release was characterized by an initial peak release (0.9 - 2.2 mg min^{-1}) during the first 60 – 105 min, which was followed by an exponential decay in release rate throughout the remainder of the testing periods (Figure 29). The observed slight fluctuations in mass flux data were attributed to heterogeneity within the amorphous gel structure. Overall, release rates increased with increasing $KMnO_4$ concentrations. For gelated SRP-Gs containing 9 g, 16 g, and 20 g $KMnO_4$, the maximum release rates were 0.9, 1.7, and 2.2 mg min^{-1}, respectively. However, the durations of release from the gelated SRP-G cylinders remained short (less than 21 h), despite the increased amount of $KMnO_4$ in the gel. These data suggested that the release kinetics and durations of gelated SRP-Gs are constrained by the permeability of the colloidal-silica sol matrix.

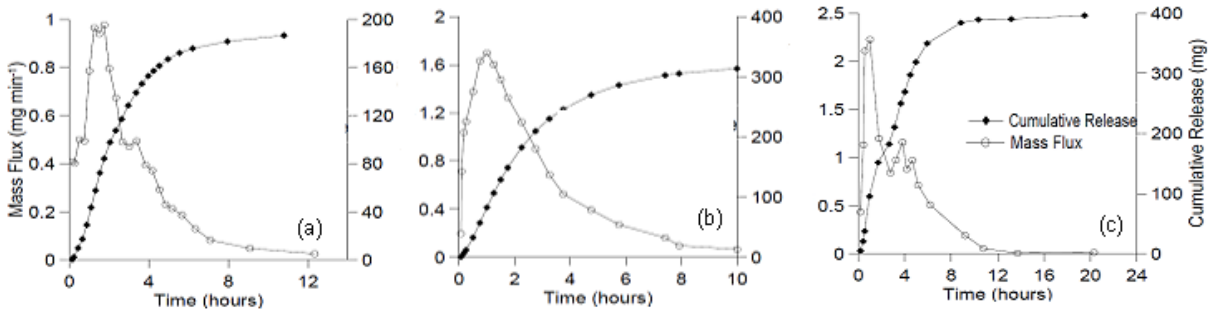

Figure 29. Temporal changes in release rates of SRP-G with (a) 9 g L^{-1} (b) 16 g L^{-1} (c) 20 g L^{-1} $KMnO_4$.

Studies have demonstrated a relationship between the silica concentration and the permeability of the colloidal silica gel (e.g., Persoff et al., 1999), and this relationship will affect release rates and durations. Iler (1979) described the gelated colloidal silica as a network of particle chains. Flow can occur within the space between gelated silica particles, and the size of these micropores depends on the silica concentration. The low permeability observed in colloidal silica should, therefore, result from a highly divided flow path consisting of many small pores. Decreasing the silica concentration should increase the space between these chains, which can be considered as a

measure of the effective micropore radius within the gel. The flux has been said to be proportional to the square of this radius. Therefore, it has been suggested that increasing the silica concentration in the colloidal silica should decrease the separation between chains of silica particles. This effect is similar to decreasing the pore diameter, thereby decreasing release rates and increasing the durations of gelated SRP-Gs.

5.4.1.2. Gelation and release characteristics of SRP-G in porous media

SRP-G solutions of variable $KMnO_4$ concentrations (20 - 25 g L^{-1}) were injected into a horizontally oriented, sand-filled glass column (L x ID = 120 cm x 4.8 cm). The flow velocity was maintained at ~2.1 m d^{-1}, giving the injected solutions a residence time of 14 h within the column.

SRP-G solutions with lower $KMnO_4$ concentrations (20.0, 21.8, and 22.5 g L^{-1}) did not gelate within the column. The gelation lag times of SRP-G solutions with higher $KMnO_4$ concentrations, 22.9, 23, and 25 g L^{-1}, were estimated to be 6, 3, and 1 h, respectively. This observation correlated well with the results of gelation batch tests, in which gelation lag times increased as the $KMnO_4$ concentrations (ionic strengths) decreased in the SRP-G solutions (Figure 28). Based on the presumed relationship between gelation lag times and concentrations (Figure 28), these data suggested that the gelation of the SRP-G solution was attenuated by dilution of the solution due to hydrodynamic dispersion. For example, in the sandy media, dilution by dispersion of the SRP-G solution containing 25 g L^{-1} $KMnO_4$ was estimated to be less than 10 %. Previously published studies used the effects of dilution on gelation lag times to achieve gelation over 75 d in batch tests (Persoff et al., 1999; Gallagher and Lin, 2009). More details regarding the gelation characteristics of SRP-Gs in porous media are summarized in Table 7.

Table 7. The gelation characteristics of SRP-Gs in porous media.

$KMnO_4$ Concentration (g/L)	Initial Spread Distance (cm)	Time of Gelation (hr)	Strength of Gel after 26-31 hours	Strength of Gel after 51-53 hours	Strength of Gel after 72 hours
22.5	12	--	strong	not visible	not visible
22.9	10	1	strong	weak	not visible
23.0	10	3	strong	moderate	not visible
25.0	10	6	strong	moderate	weak

In porous media, MnO_4^- release from the gelated SRP-G yielded a similar pattern to that of open water tests, i.e., a rapid initial peak release of up to 850 μg min^{-1}, followed by exponential decay and an asymptotic release phase (Figure 30). Compared to the release rates for the SRP-G that gelated in the column (Figure 30b), the asymptotic release phase is lacking in the SRP-G that did not gel (Figure 30a). The asymptotic release phase lasted between 20 and 70 h, demonstrating the possibility of providing a long-lasting method of MnO_4^- release into groundwater once the SRP-G gel is emplaced. Similar to the results of open-water tests, the release rates exhibited fluctuations that are attributable to the amorphous structure of the silica gel.

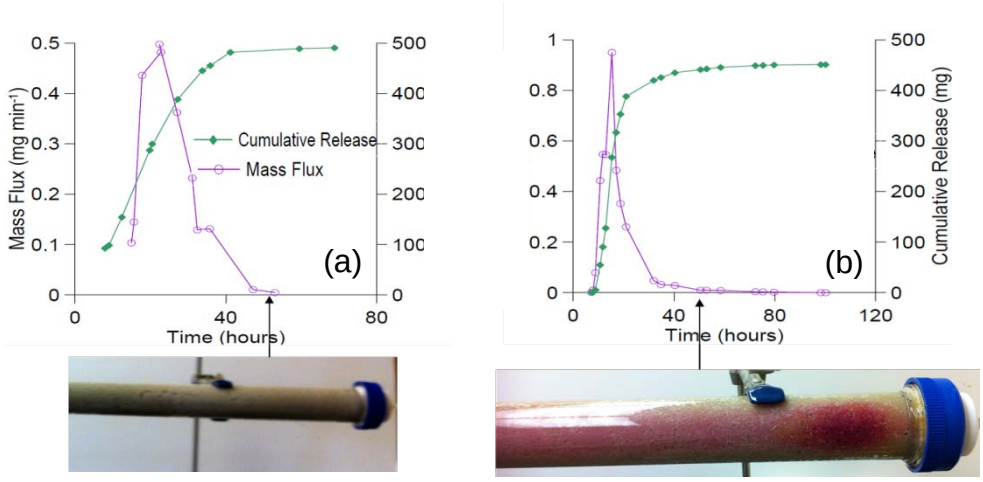

Figure 30. Column tests with porous media in which (a) gelation did not occur, showing absence of remaining gel at conclusion of first-order mass flux phase, (b) gelation occurred, showing gel present at conclusion of first-order mass flux phase. The glass column was rotated to show SRP-G accumulated at the bottom of the sandy media.

Relative concentrations of MnO_4^- down the length of the column were optically monitored to investigate the migration, gelation, and release of SRP-G in porous media. In columns with SRP-G solutions that did not gelate, such as those that contained 20.0, 21.8, and 22.5 g L^{-1} $KMnO_4$, transport of the SRP-G solution appeared to be constrained by advection and dispersion Figure 31). However, the SRP-G solutions that gelated within columns, such as solutions containing 22.9, 23, and 25 g L^{-1} $KMnO_4$, exhibited characteristic transport and release patterns indicating the effects of diffusion in addition to advection and dispersion (Figure 31). It was noted that the SRP-G solution was initially concentrated in a small area before being advectively transported down the column during the peak and exponential-decay periods of release. Once the SRP-G solidified, the mass flux of MnO_4^- appeared to diminish, indicating attenuated release of MnO_4^- from the gelated SRP-G. The transport of SRP-G after solidification also appeared to have an additional attenuating component and was linked to the asymptotic mass-flux phase. This observation is evident in Figure 30, which shows the effects of in-situ gelation upon extended mass flux.

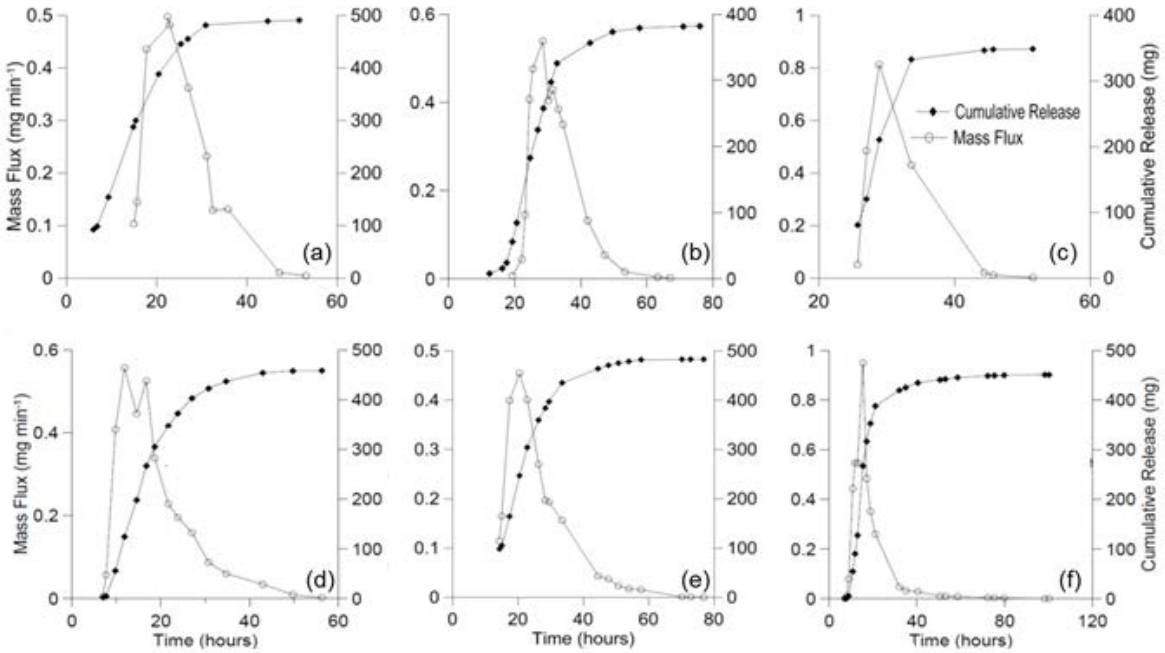

Figure 31. Mass flux and cumulative release from gelated SRP-G with (a) 20.0 g L^{-1} (b) 21.8 g L^{-1} (c) 22.5 g L^{-} (d) 22.9 g L^{-1} (e) 23.0 g L^{-1} (f) 25.0 g L^{-1} $KMnO_4$.

Gelation of the SRP-G solution was determined visually through assessment of the relative changes in the position of the SRP-G over time. Gelation was pronounced when the SRP-G appeared as a concentrated region of MnO_4^- that did not flow any further down the column. The existence of a gel was confirmed upon excavation of sand from the column. Optical data (in the form of photographs and videos) was obtained throughout the span of column tests to monitor the spreading, gelation and release of the SRP-G in the saturated sand-filled column. Data are shown from select column tests in which gelation within the column was not observed (Figure 32: 22.5 mg L^{-1} $KMnO_4$) as well as when gelation occurred (Figure 33: 25.0 mg L^{-1} $KMnO_4$). The optical data indicated that, when gelation did occur, it tended to occur within the first 10 cm of column or near the gel injection point. For SRP-G concentrations that did not gel, no remnant SRP-G solution remained near the injection point following advective mass transport. In tests in which gelation occurred, the general concentrations tended to decrease throughout the span of the test, as evidenced by the degree of saturation of the purple color correlating to MnO_4^-, until asymptotic release was attained (as reflected in the mass flux data collected via sampling of the effluent). Another notable feature of SRP-G dynamics in porous media was that the solution initially sank through the pores to form a dense plume at the bottom of the media before being displaced by the ambient flow. Much is understood, both experimentally and theoretically, with regard to the migration of dense plumes in unstable configurations and the consequent development of instability (e.g., Schincariol and Schwartz, 1990; Schincariol et al., 1993; Schincariol et al., 1994; Solpuker et al., 2012). This observation correlates with the assumption that the SRP-G under-rides the groundwater and is release from the gelated SRP-G into the over-riding groundwater flow (Figure 34).

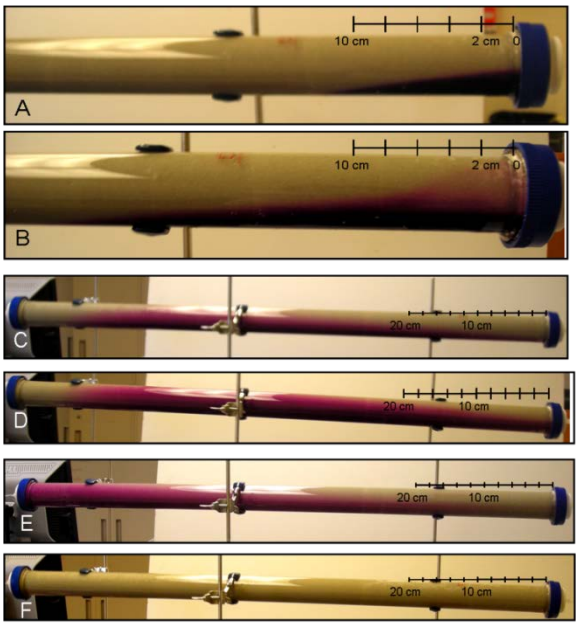

Figure 32. Photos showing dynamics of SRP-G (22.5 g L^{-1} $KMnO_4$) that did not gel within the glass column. (A) Immediately after injection, (B) 1.5 h after injection, (C) 24 h after injection, (D) 24 h after injection (column was rotated to show the bottom of the sandy media, (E) 33 h after injection (bottom view), and (F) 48 h after injection (bottom view).

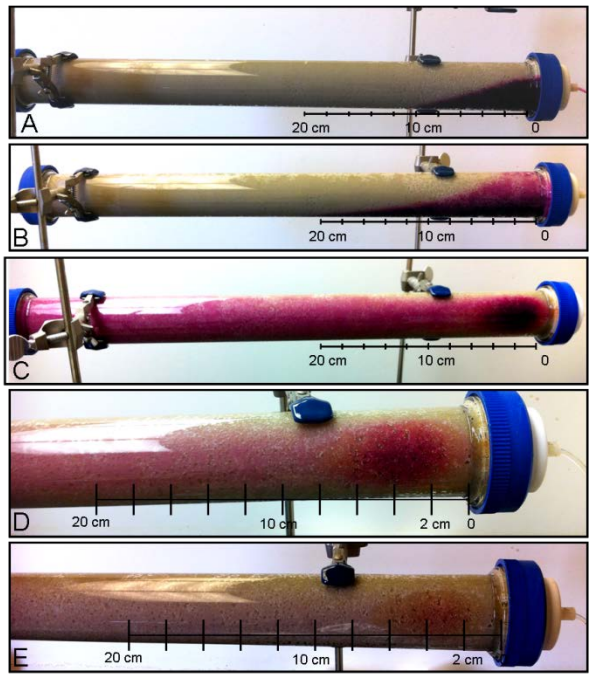

Figure 33. Photos showing dynamics of SRP-G (25 g L^{-1} $KMnO_4$) that gelled within the glass column. (A) Immediately after injection, (B) 1 h after injection, (C) 31 h after injection, (D) 51 h after injection (bottom view), and (E) 72 h injection (bottom view).

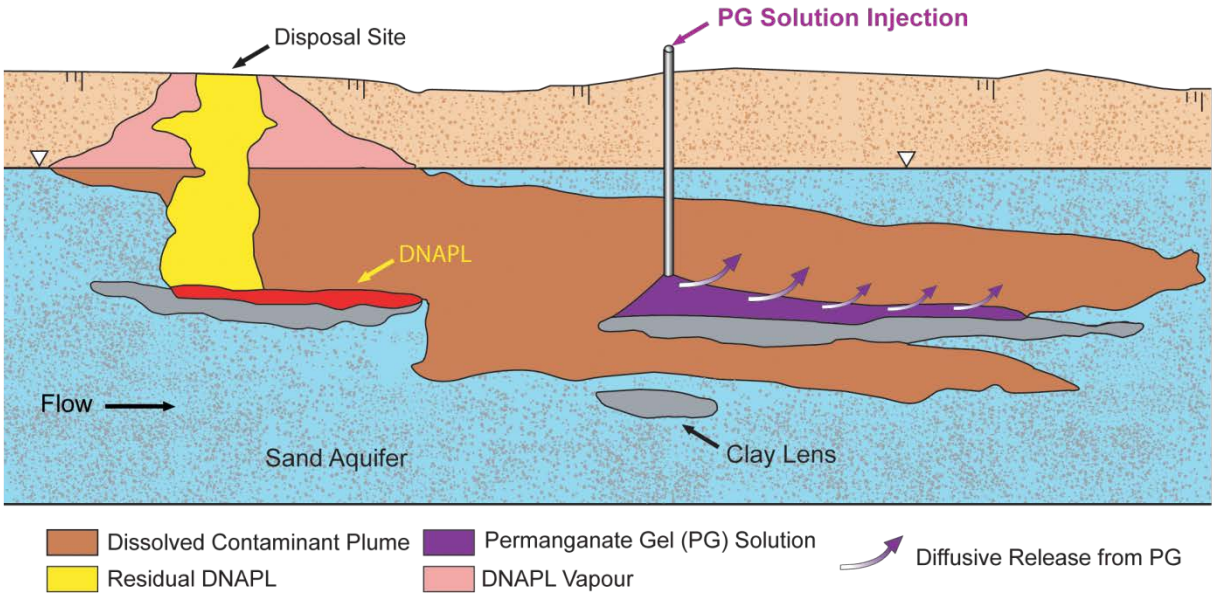

Figure 34. Conceptual model of SRP-G scheme. Note that SRP-G gels are formed upon impermeable layer, release permanganate to over-riding groundwater flow.

During the column tests, it was noted that gelation within a saturated sand-packed column occurred in a relatively short period of time (< 8 h). Otherwise, gelation did not occur at all. This is attributed to continual dilution of the SRP-G as the solution is transported over time. Column-test data in open water yielded relatively rapid release of MnO_4^- from the cylinder, an observation that was not shown to be an accurate representation of how the same SRP-G gel would behave within saturated porous media under ambient groundwater flow. This discrepancy is thought to be attributed to the following two factors: 1) a stronger concentration gradient (between the gel and the water) due to the higher flow rate and larger contact area between the gel and the water in the open-flow column test, and 2) a differing release mechanism. The proposed method of release of MnO_4^- from solid SRP-G in flowing water is swelling-driven release, in which the membrane undergoes a transition from a glassy to a gel state due to hydration of the surface layer. Polymer chains in the gel state are more mobile and, thus, would allow for the active agent to diffuse more rapidly than in the glassy state (e.g., Pothamkury, 1995). Because the boundary of the SRP-G plume injected into porous media may not reach the glassy state due to dispersion, the method of release is likely to differ from release through solidified SRP-G and may be affected by an attenuated concentration gradient along the dispersed plume boundary.

Although measuring the space between silica-particle chains was beyond the scope of the present study, it is useful to understand the effects of concentration upon both the flow of the SRP-G solution through porous media as well as the release rate. Release is observed to occur more quickly in the presence of a diluted SRP-G solution due to the larger spaces available for water to flow through. Therefore, the effect of diluting the SRP-G solution is thought to be two-fold, in that 1) it decreases the gel's ability to form within saturated media and 2) it quickens release from the gel matrix once it has formed. The issue of rapid release from gelated SRP-Gs can be

addressed through the use of colloidal silica solutions with higher initial silica concentrations. Release from SRP-Gs was also noted to be affected by an attenuated concentration gradient within porous media due to the restricted interface between water and the SRP-G as well as the reduced flow rate through pores. Overall, SRP-Gs constructed with colloidal silica demonstrated strong potential as a long-term source of MnO_4^- release.

5.5. Description and verification of a novel flow and transport model for silicate-gel emplacement

5.5.1. Results

Figure 35a shows the flow and gelation behavior of the first sodium silicate solution. The solution took on a circular shape within the injection zone 3 minutes after injection. Small instabilities developed around the rims of this fluid mass and continued to grow through time (Figure 35a; 11 minutes to 29 minutes). This solution gelled quickly in 5 minutes due to high bicarbonate concentration. Most of the mass of injected solution gelled within the injection zone as indicated by dark colored contour lines and was still there until the end of the experiment (~ 90 minutes).

Compared to silicate solution in the first experiment, the silicate solution in the second experiment was created to be more mobile (Figure 35b). Most of the injected solution sank slowly and at the same time the viscosity started to increase. The front end of the instability reached the bottom of the flow tank in 12 minutes with gelation of the solution in 15 minutes (Figure 35b). The second solution has a 5% (by weight) lower bicarbonate concentration than the first experiment so it gels more slowly. Only some of the silicate solution actually gelled close to the injection zone, as indicated by the light colored contour lines (15 minutes). Darker colored contour lines mark the inner and lower zones of the instability. These zones are associated with relatively stronger gels. Eventually, the solution stopped moving after 15 minutes and remained in place.

As the third solution started sinking, small instabilities developed at the front end (Figure 35c). These instabilities grew as sinking continued until the solution reached the bottom of the flow tank after 15 minutes. The third solution has the lowest bicarbonate concentration so gelation required 23 minutes, the longest among the three experiments. Only a small volume of this solution eventually gelled and remained in place at least 90 minutes after the injection. The lighter colored contour lines at 90 minutes indicate that the gel is weaker than the previous marked by darker colored contour lines.

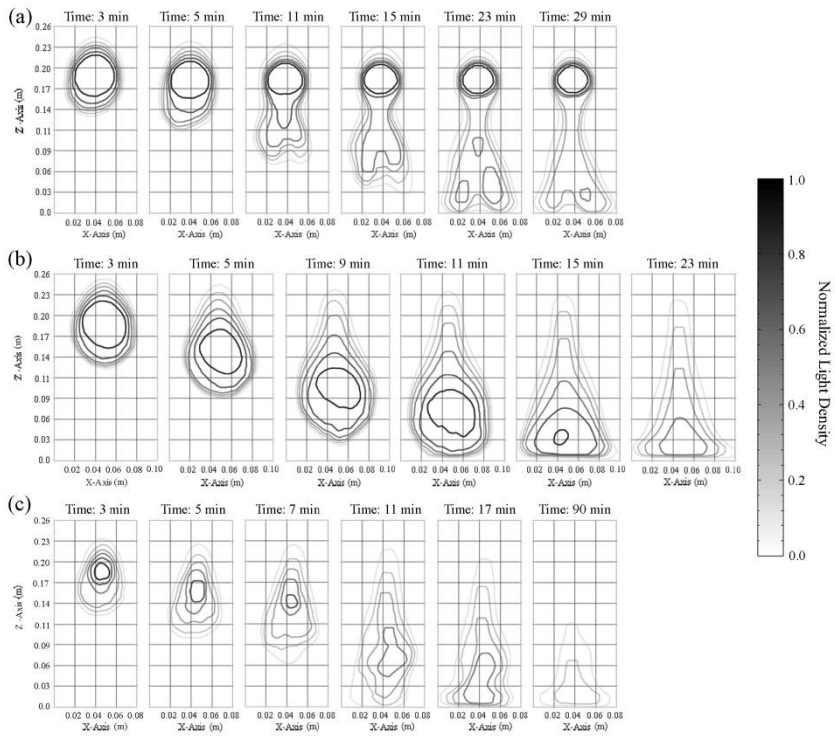

Figure 35. The temporal evolution of the gelation of silicate solutions. The first, second and third experiments are shown in (a), (b) and (c), respectively.

Figure 36a - c show the modeling results for the three laboratory setups after injection of the solute. The simulation output is illustrated for concentration ω_1 (isolines) and viscosity μ (background coloring).

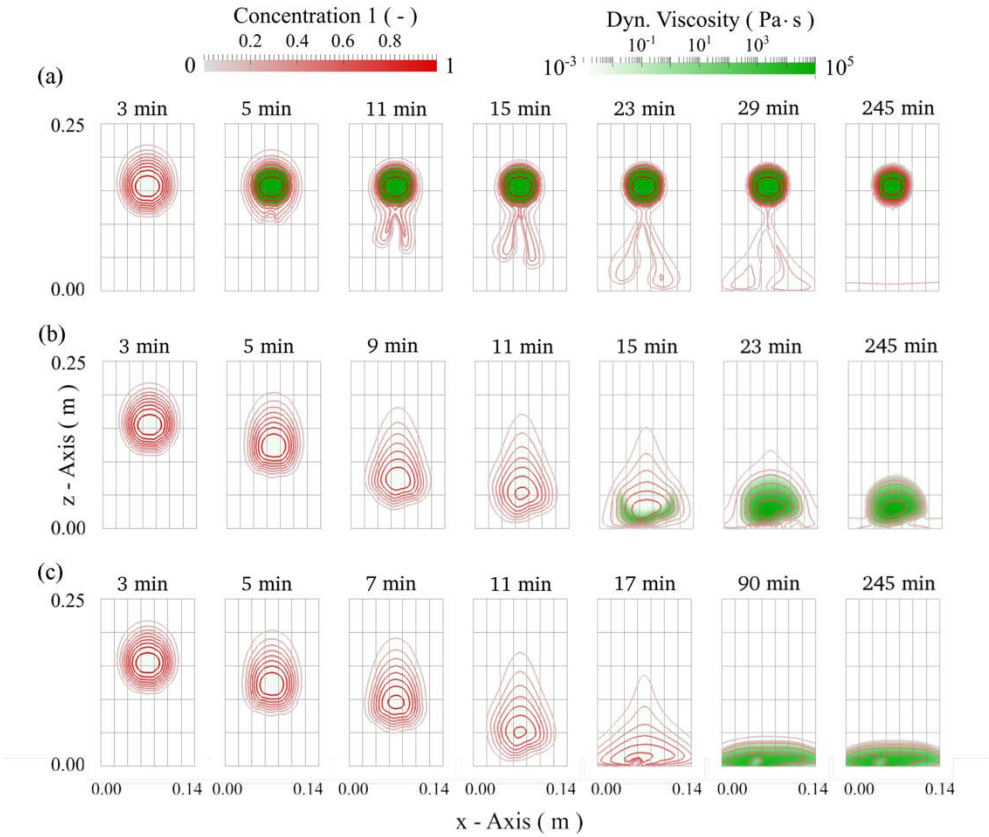

Figure 36. Results of numerical simulation for experimental setups 1 (a), 2 (b), and 3 (c); isolines are concentration 1 $\boldsymbol{\omega_1}$, shading is viscosity $\boldsymbol{\mu}$.

The simulated behavior of the solution resembles the general features of the laboratory experiments, which include:

- density-dependent movement of the solute (including arrival of the solute at the bottom of the domain),

- viscosity change after a given residence time,

- continued movement of non-gelated solute due to too low concentration,

- persistence of solute in gelated area due to high viscosity, and

- fingering as a result of slight heterogeneity of hydraulic conductivity.

One of the objectives of the modeling is to match the gelation times of the solutions as closely as possible to those observed in the experiments. The rate of the gelation of the silicate solutions depends on their concentration and that of the acid causing the solution to gel. Calculated gelation times, defined by the point of sudden increase in viscosity, for experiments 1, 2 and 3 are 3 min, 15 min and 23 min, respectively. The calculated values closely match the observed gelation times. Normally, all of the silicates gel unless they are diluted by transport processes.

The numerical model captures not only the concentration profiles but also the shape of the sinking silicate plumes reasonably well. For instance, a circular gel zone developed in simulation 1 after 5 min and two small instabilities were generated in less concentrated zones (e.g. time steps 11 min and 15 min). Although the generation and flow behavior of instabilities are quite complex, similar fingering was observed in the first experiment. Furthermore, the plumes of the second and the third experiment at time step 11 min are narrow at the top and wider towards the bottom of the flow tank.

Concentration of the silicate solution increases toward the inner parts of the plumes and gelation took place in the zones with relatively higher concentrations of silicates that lie at the bottom of the sinking plumes. Similarly higher concentrations could be observed at the lower and inner zones of the gelled plumes (Figure 36b and c).

As an example, Figure 37 shows concentration ω_1 (isolines), viscosity μ (background coloring), and velocity vectors including magnitude (colored arrows) for a detailed section at the boundary to the gelated solute of experiment 1. Movement within the zone of gelation is very low (flow velocity $v < 3\ mm \cdot a^{-1}$) due to high viscosity ($\mu \approx 106\ Pa \cdot s$), while zones without gelation are associated with density induced velocities of $v < 10\text{-}5\ m \cdot s^{-1}$. The viscosity change is sharp occurring over about 0.5 cm or 3-4 cells. The numerical simulation was very stable showing no sign of oscillation even with these high differences in fluid properties across a sharp interface.

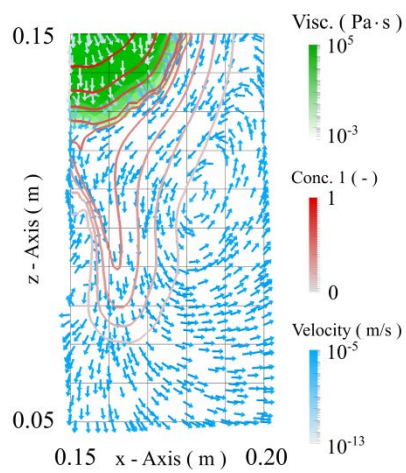

Figure 37. Detailed section at the boundary of the gelated solute for experiment 1 at time $\boldsymbol{t = 9\ min}$, isolines are mass fraction 1 $\boldsymbol{\omega_1}$, shading is viscosity $\boldsymbol{\mu}$, arrows are velocity vectors.

5.5.2. Discussion

During the gelation process a combination of viscosity change and variable density flow alters the concentration profile of the silicate solution. Experiments showed that gelation takes place only in zones with relatively higher solute concentrations. The numerical model generated a concentration profile similar to experiments. For example, in simulation 1, a zone of gelation and a zone of mobile plume formed when silicate concentrations were high and low, respectively. Yet, in the first experiment (Figure 35a), the exact shape of the concentration profile of the sinking zone is different than with simulation 1 due to fingering effects. While care was taken to

provide a homogeneous porous medium in the laboratory setups, slight heterogeneity will always be present, which cannot be exactly replicated in a numerical simulation. However, by creating a small degree of heterogeneity using a random distribution of hydraulic conductivity in the parameterization of the simulated porous medium (see also Table 2), similar fingering behavior can be simulated with the model. In general, fingering strongly depends on the fineness of gridding (see e.g. Park (2004), Johannsen et al. (2006)) and is especially sensitive to homogeneous parameter distributions. By introducing a slight heterogeneity, fingering instabilities will preferably occur in areas of higher conductivity. Any influence of spatial resolution will be of minor importance, and fingering will not be triggered by numerical errors as might be the case with homogeneous setups.

In simulations 2 and 3 (Figure 36b and c), the initial mobile silicate solutions sink to a greater extent and hit the lower boundary of the domain before they gel as in the experiments (Figure 31b and c). Although the shapes of the simulated plumes resemble those observed in the second and third experiment, the experimental plumes are narrower and longer especially at later times. This discrepancy might be due to unknown and not exactly determinable local heterogeneity of material properties, e.g. small variations of (an-)isotropy in the experiment.

When calibrating a numerical model, over-parameterization is a known problem. Essentially, there are too many parameters available for calibration to find a global minimum of deviations between observation and simulation results. Although the approach we present involves many parameters, offering the possibility to adapt to specific solutes, all three simulations used the same material parameter set (Table 2) and gelation specific variables (Table 4). Only two parameters changed in each of the three model runs. However, their values were constrained by experimental observations. The decay coefficient λ was deducted from the time until gelation, and density coefficients were derived from measured non-diluted initial densities of the non-gelated injected solutions (see Tables 2-4). Calibrated parameters were in the line with the typical range of parameters, found in the literature. For example, mechanical dispersivities and diffusion coefficient lie within the expected range for small scale experiments (Oswald and Kinzelbach, 2004). Acker (1970) measured viscosity increases up to a factor of $> 10^7$ similar to our calibrated parameter β_{max}; finally, values of hydraulic conductivity obtained in model calibration are very close to those reported in literature (Schincariol and Schwartz, 1990; Swartz and Schwartz, 1998).

5.6. Geopolymers as slow-release materials for potassium permanganate

5.6.1. Results

5.6.1.1. XRD analysis

Figure 38 shows XRD patterns for the blank and $KMnO_4$ doped geopolymer powders. Broad diffuse halo peaks were observed for both geopolymer powders at 2θ values between 15º and 40º and were attributed to the non-crystalline state of the geopolymer where SiO_4 and AlO_4 tetrahedra share oxygen atoms lacking any long range order (Davidovits, 2002). The lack of a second broad diffuse halo peak located between 7º and 12º was a result of incorporation of aluminium in the silicate gels (Giannopoulou and Panias, 2010). In addition to amorphous components of the geopolymers, the diffraction peaks indicate the presence of crystalline phases such as quartz, halite, sodian sylvite and $KMnO_4$.

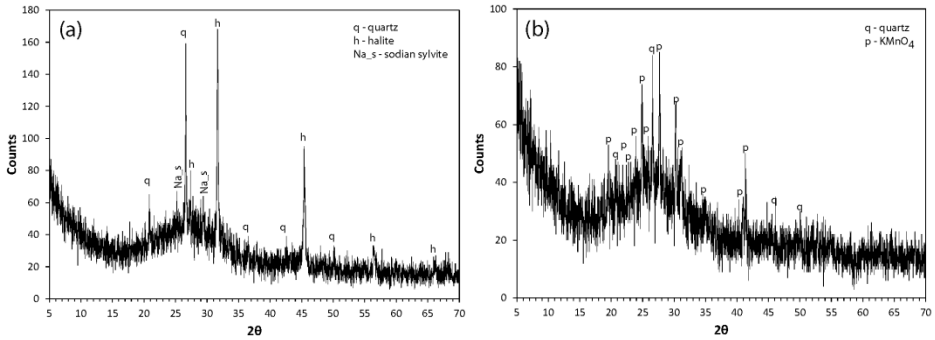

Figure 38. The XRD patterns of the blank (a) and $KMnO_4$ doped (b) geopolymer powders.

5.6.1.2. 1-D column experiment

Neither surface cracks nor surface erosion were observed on any of the samples during the column experiments. Both the geopolymer characteristics mentioned above and the structural stability of samples placed in the glass column during the experiment allow us to assume that the geopolymer is essentially insoluble in water. Figure 39 shows the temporal changes in MnO_4^- concentrations in the column discharge and the % permanganate released over 19 days of testing period. Permanganate concentrations were initially high (up to 800 mg l^{-1}) for all the samples due to high solubility of the $KMnO_4$ (63.8 g/L at 20ºC), but gradually decreased to 56 mg l^{-1}, 96 mg l^{-1} and 127 mg l^{-1} on day 1 for the samples 1, 2 and 3, respectively. Permanganate concentrations declined with time, decreasing below 10 mg l^{-1} on day 8 for the sample 1 and below 15 mg l^{-1} on day 18 for samples 2 and 3. Sample 1 approached exhaustion at the end of the day 7. It took about 19 days for samples 2 and 3 with higher $KMnO_4$ concentrations to approach the end of their life time. Although sample 2 had lower $KMnO_4$ concentrations than sample 3, it had a longer life time than sample 4.

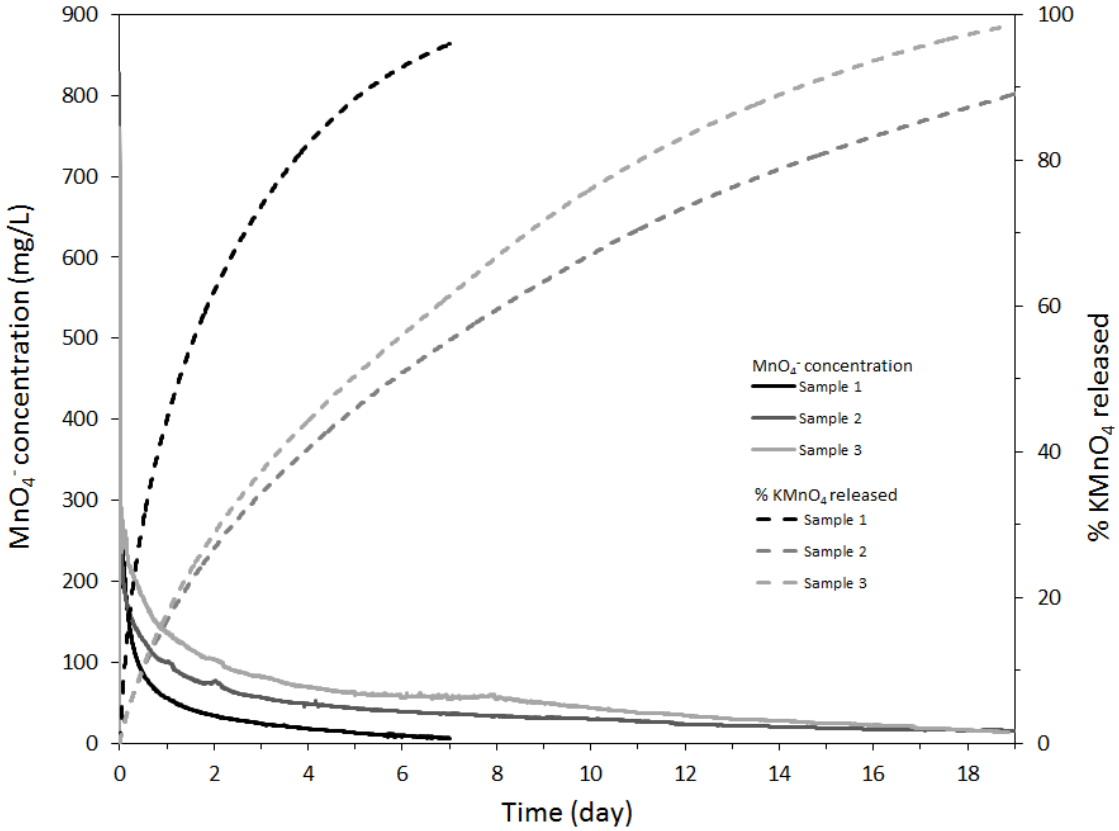

Figure 39. Temporal variations in the MnO_4^- concentrations in the column outflow and the measured amount of release MnO_4^-.

5.6.1.3. SEM imaging

$KMnO_4$ granules of different sizes were dispersed throughout the geopolymer matrix as circular grains and irregular broken fragments (Figure 40a, c, e). $KMnO_4$ grains either touch each other or are packed closely to each other, essentially separated within the geopolymer matrix. The unflushed geopolymer matrices have microscale pores (Figure 40b, d, f). The SEM images of the flushed samples show the porous structure of the geopolymer samples at the micro and macro level (Figure 41). Secondary pores developed by the dissolution of the $KMnO_4$ granules are represented by circular depressions (Figure 41a, c, e). The primary pores of the geopolymers seem to be connected to each other and to secondary pores (Figure 41b, d, f).

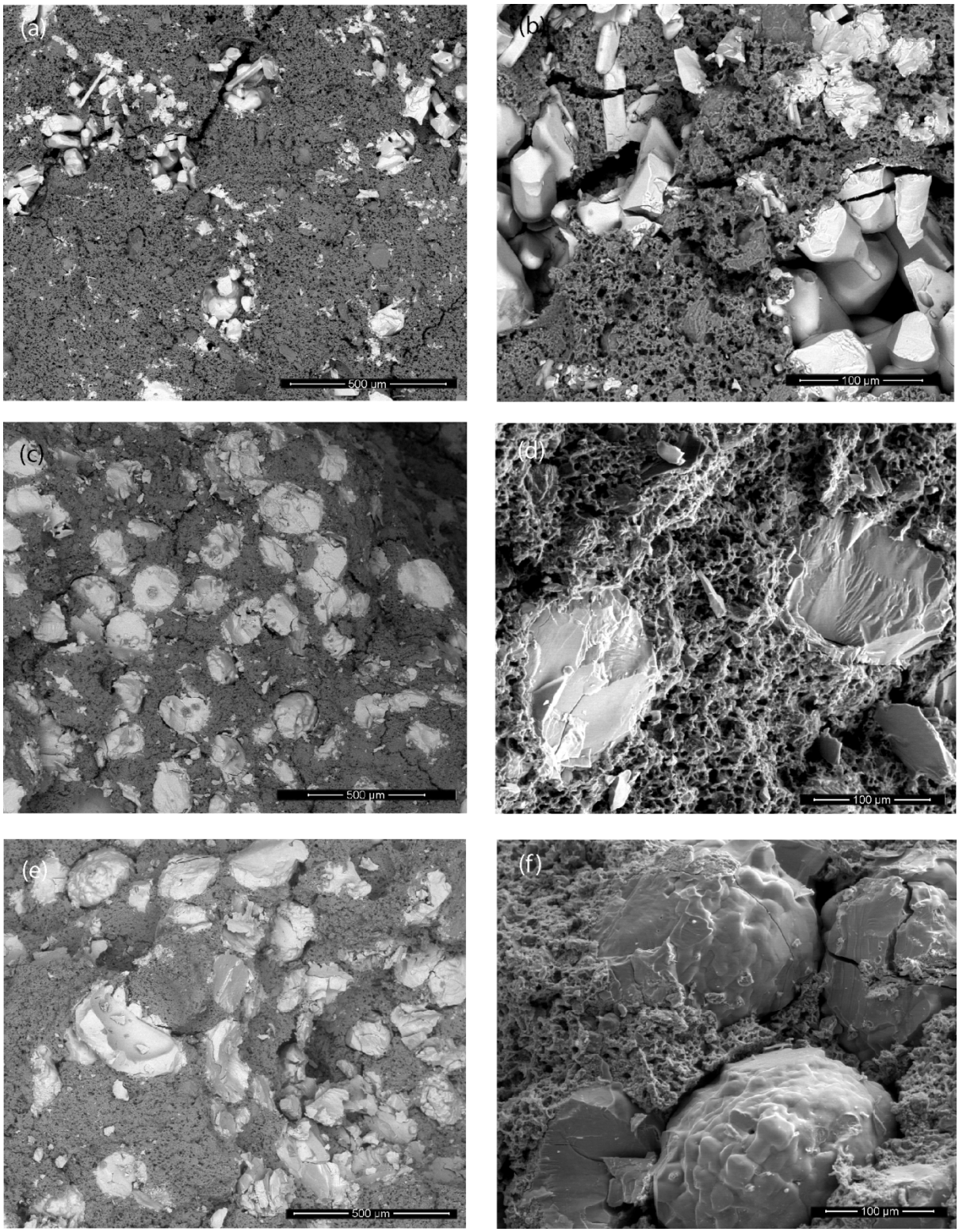

Figure 40. SEM images (back-scattered electron image) of $KMnO_4$ doped geopolymer samples. (a),(b) Sample 1; (c), (d) sample 2; (e), (f) sample 3. (a), (c) and (e) show low magnification images relative to (b), (d) and (f).

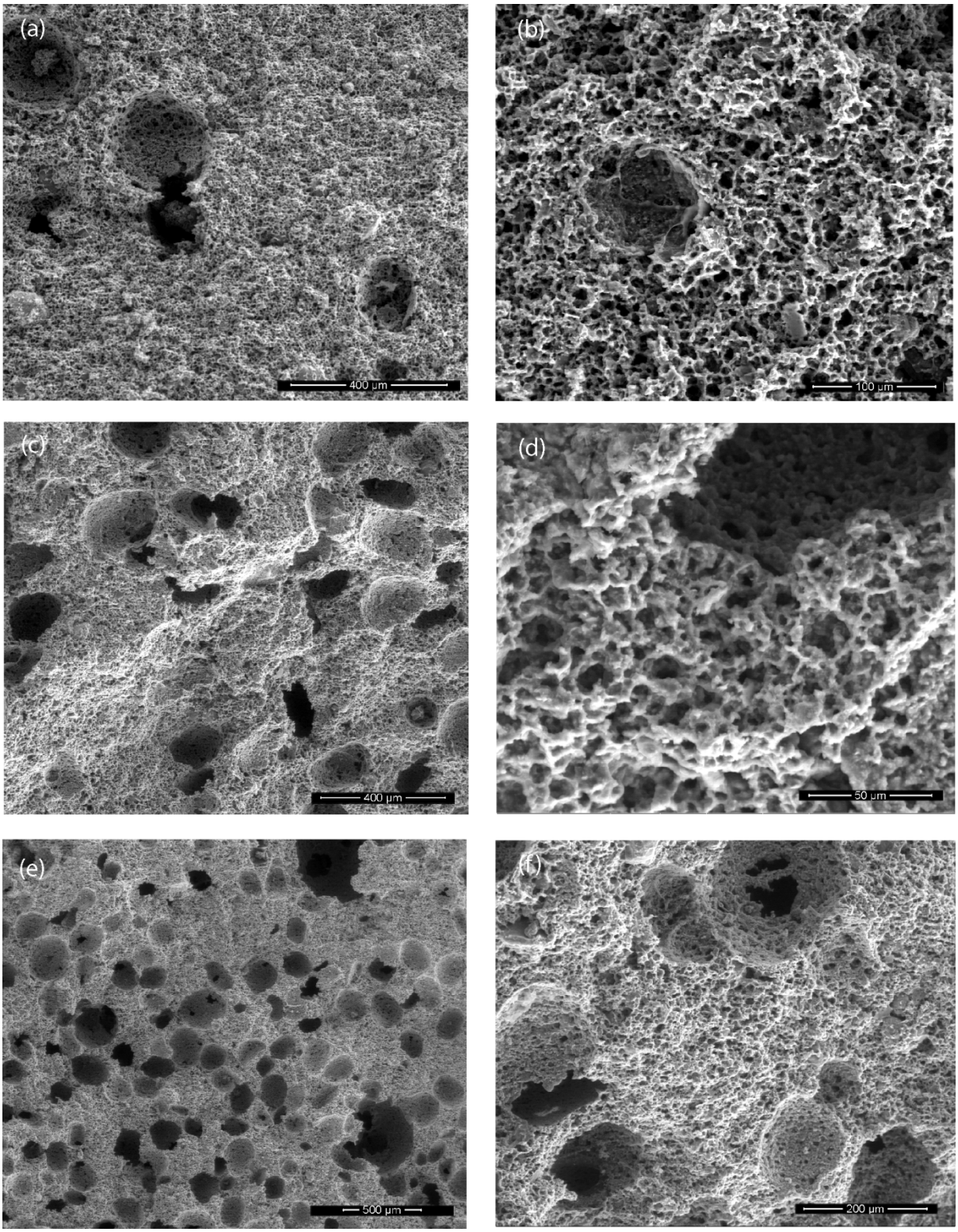

Figure 41. SEM images (large-field detector image) of $KMnO_4$ doped geopolymer samples. (a),(b) Sample 1; (c), (d) sample 2; (e), (f) sample 3. (a), (c) and (e) show low magnification images relative to (b), (d) and (f).

5.6.2. Discussion

The creation of controlled-release pharmaceuticals of necessity requires a clear understanding of processes at work, which control the release rates of active ingredients from slow-release solids. Most conceptual models provide for diffusion as the primary release mechanism. With simple diffusion-controlled transport that follows Fick's first and second laws, releases are controlled by a constant diffusion coefficient (Case I type system) (Crank, 1975; Frisch, 1980).

The polymers used in pharmaceuticals applications can be complex materials providing for exotic patterns of release due to structural or chemical changes in the polymer. Thus, diffusional releases can be non-Fickian, where diffusion is occurring together with changes in the polymer structure (i.e., relaxation). Among these complex cases, is a situation where a release is not Fickian diffusion alone due to some additional contribution from the chemical release of the active ingredient with a rate is independent of time (i.e., zero-order kinetics) (Crank, 1975; Frisch, 1980). This model, referred to as Case II diffusion, assumes that transport diffusion process is very rapid compared with the polymer relaxation process. In other words, diffusion is not complicated by structural changes in the polymer.

One way of sorting out the processes at work in a controlled release material is through the detailed analysis of release experiments. Data from experiments are fitted to a simple, semi-empirical equation to distinguish diffusion and other processes at work under perfect sink conditions (e.g. Korsmeyer and Peppas, 1981). The general form of this equation is:

$$M_t/M_\infty = kt^n \tag{27}$$

where M_t/M_∞ is the fractional release of the chemical, k is a kinetic constant (t^{-n}) characteristic of the chemical/polymer system, t is release time and n is the release exponent (Korsmeyer and Peppas, 1981; Korsmeyer et al., 1983; Peppas, 1985). The development of equation 1 can be found elsewhere (e.g. Peppas, 1985; Ritger and Peppas, 1987). Equation 27 is valid for the early of an experiment ($\frac{M_t}{M_\infty} < 0.6$) where the assumption of perfect sink conditions is valid (Peppas, 1985).

Processes are identified by interpreting the value of the release exponent, n, coming out of the experiments. For example, simple Fickian diffusion from a cylinder is inferred when fractional release when $n = 0.45$ for the early part of the experiment. Anomalous diffusion is implied with$1 > n > 0.45$. When release exponent n takes a value of 1.0, then the chemical release rate is independent of time (Case II). We followed this general approach in interpreting our experimental data to elucidate mechanisms controlling the release $KMnO_4$ from the geopolymers.

The first 60% of the fractional release data from our column experiments were fitted to equation 1 using the MATLAB (R2013b) Curve Fitting Tool. A non-linear least squares optimization provides the best fit between the model system and the measured data. The kinetic constant and the release exponent calculated for each sample were given in Figure 42. The release exponents are higher than 0.45 indicating the mechanism controlling the $KMnO_4$ release from the geopolymers is more than simple diffusion alone (Case I).

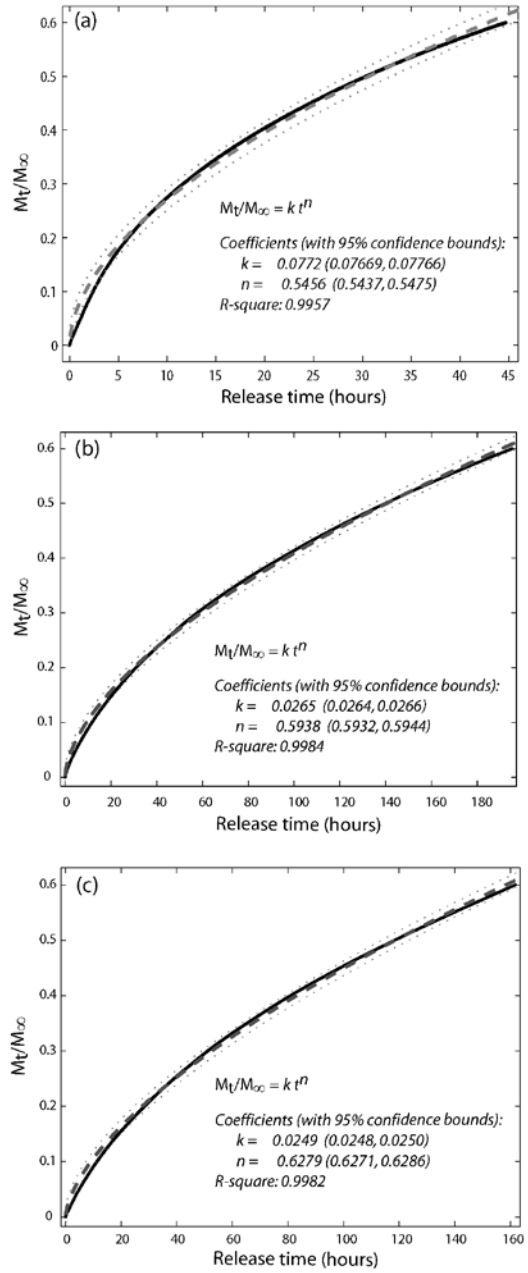

Figure 42. The first 60% of the fractional release of $KMnO_4$ from geopolymers (solid black curves). Dashed gray curves represent the best fit for data calculated by the nonlinear least squares method. (a), (b) and (c) represent the first, second and third sample, respectively.

Careful inspection of the release exponents also shows them to be different for each sample (n = 0.55, 0. 59, and 0. 63; Figure 42 a, b, and c, respectively). Given the differences in initial $KMnO_4$ loading of samples 1 to 3 ($1.40x10^{-1}$ g/cm^3, $4.63x10^{-1}$ g/cm^3 and $6.07x10^{-1}$ g/cm^3, respectively), it is evident higher loading of samples with $KMnO_4$ produced a higher release rate. This behavior suggests that whatever additional process is operative beyond simple diffusion, it becomes magnified through increasing additions of $KMnO_4$.

The most likely explanation is related to the accelerated release of $KMnO_4$ through the secondary porosity created by the dissolution of $KMnO_4$ grains. Comparison of Figures 40a, b, c shows that $KMnO_4$ mostly occurs as large granules surrounded by a connected microporosity provided by the geopolymer. Dissolution of granules promotes the formation of macro pathways both for water penetration into the sample and accelerated releases of MnO_4^- by a second mechanism involving chemical dissolution and fast transport. One outcome of adding this second mechanism is the earlier exhaustion of Sample 3 as compared Sample 2 because the higher loading of $KMnO_4$ in Sample 3 has increased connectivity of these secondary pores. Thus, the two major transport mechanisms in our PDG samples include dissolution-related fast transport coupled with diffusion controlled processes.

We explore relative contribution of each of these components to overall transport by using a model that mathematically represents the two release mechanisms just described. The model itself was developed to describe release behaviour of dynamically swelling hydrogels proposed by Berens and Hofenberg (1978):

$$M_t/M_\infty = k_1 t + k_2 t^{1/2} \tag{28}$$

where the first term describes the dissolution-related, fast transport mechanism and the second term describes the diffusive release. Our implementation assumes that dissolution with fast transport can be represented by the rate-controlling parameter, k_1 and that the exponent ½ on the second term can be modified to 0.45 to mimic account for our cylindrical sample forms.

Values of k_1 and k_2 for each sample were found with the MATLAB (R2013b) Curve Fitting tool by using a non-linear least squares method (Figure 43). The very large values for the coefficients of determination (r-square), > 0.99, between the best fit equation and the experimental results show that equation 28 provides a description of the release rate. The decrease in k_2 from Sample 1 to Sample 3 indicates that the relative importance of diffusion controlled releases relative to the dissolution-related transport mechanism.

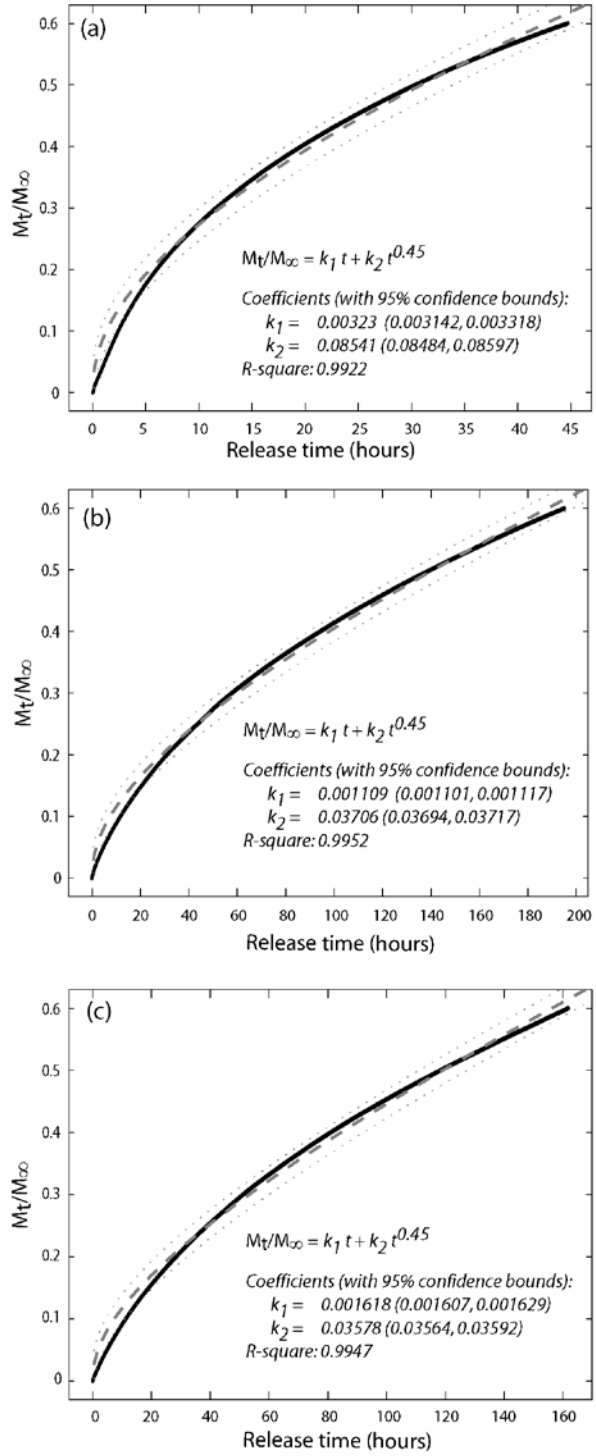

Figure 43. The first 60% of the fractional release of $KMnO_4$ from the geopolymers (solid black curves). Dashed gray curves represent the best fit for data using equation 2 calculated by the nonlinear least squares method. (a), (b) and (c) represent the first, second and third sample, respectively. Dotted curves represent the 95% confidence intervals.

Using the k_1 and $k_2$values from Figure 43 and the individual terms on the right hand side of equation 28, it is possible to represent the relative contribution to the total release provided by each mechanism. It is apparent in Figure 44 that Fickian diffusion is the dominant release mechanism for the three samples. The relative contribution from dissolution-related fast transport increases as the quantity of $KMnO_4$ initially present in increases from Sample 1 to Sample 3 (Figure 44). For Sample 1, the diffusion and dissolution mechanism account for about 78% and 22% of the total release, respectively and thus the diffusion mechanism contributes approximately 3 times more to MnO_4^- than the dissolution-related fast transport mechanism at the end of the 45 hours (Figure 44a). Moving to Sample 2 and Sample 3, diffusion systematically diminishes in importance providing relative contributions of ~66% and ~59%, respectively at the end of the 200 hours and 160 (Figure 44b, c).

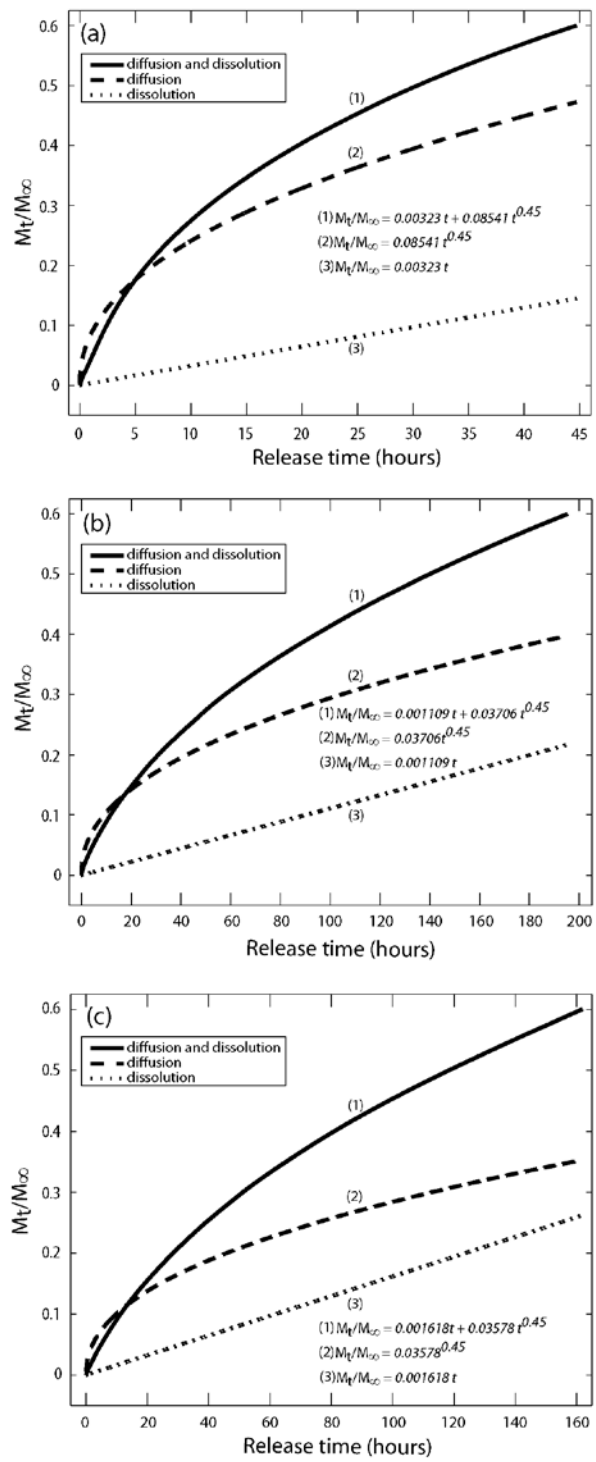

Figure 44. The first 60% of the fractional release of $KMnO_4$ from the geopolymers (solid black curves). Dotted lines and dashed curves represent the dissolution-related, fast transport and Fickian diffusion processes, respectively using k_1 and $k_2$values in Figure 43. (a), (b) and (c) represent the first, second and third sample, respectively.

Through the experiments, as water invaded the samples, the geopolymer transitioned from a hard crystalline solid to a softer, more rubbery material. In conventional pharmaceutical materials, this change in the structure of polymers is known to influence release rates as yet another mechanism. At this stage, given the very good fits that we obtained with a two parameter, mechanistic model, we think the effects are likely much less important than the two key release mechanisms already identified.

6. Conclusions and implications for future research

6.1. Conclusions

Deep, low concentration plumes of chlorinated ethylenes and contaminated less permeable units can be remediated by using the in-situ chemical oxidation (ISCO) using $KMnO_4$. The efficient delivery of the $KMnO_4$ is the key to the success of the ISCO method and it is commonly accomplished by injecting concentrated $KMnO_4$ solutions to the contaminated aquifers or installing $KMnO_4$ doped slow-release solids into deep wells across the path of contaminant plumes. Success in utilizing dense $KMnO_4$ solutions to control the spread of contaminant plumes requires $KMnO_4$ solutions to mix with the contaminated fluid within the aquifer and provide longer contact time with the plume.

In this project, we investigated the behavior of saline solutions in fresh water through numerical modeling and flow tank experiments using different set ups which involved permeable horizontal layers and lenses and less permeable lenses. Numerical modeling of the variable density flow experiments in lenticular media indicate that lenses enhance mixing and high permeability lenses act as conduits for dense solutions to be transported laterally, reducing the efficiency of dense solutions in reaching deeper parts of the aquifer. Fingering appears not to develop in highly heterogeneous systems, under the conditions that we tested. In the flow tank experiment with homogeneous, continuous layers, dense solutions start sinking under the injection zone creating instabilities that grows both vertically and laterally with time. Some of the less saline solutions were carried laterally along the high hydraulic conductivity layer causing small instabilities along this layer. Less permeable layers helped slowing down the vertical and lateral migration of dense fluids. The other flow tank experiment utilized discontinuous lenses of high and very low permeability. The discontinuous high hydraulic conductivity lens created fingers right under the injection zone as expected but furthermore, when less saline solutions reached to the end of the lens, they sank as a big instability instead of creating small and less saline instabilities as in the first case. Hence, better mixing within the aquifer was achieved. Downward sinking of dense solutions is stopped by these discontinuous bentonite bearing lenses. Dense solutions both diffused into the bentonite bearing lenses and moved around these lenses to continue downward migration which caused a lateral migration of the dense fluids and an increase residence time. This shows that clay rich lenses can be utilized as slow-release solids after MnO_4^- rich solutions diffuse into these lenses.

The use of dense viscous silicate solutions aids in delivering oxidants into deeper portions of the aquifers and increasing the residence time of oxidants in the targeted zone due to their higher viscosity. Furthermore, it is possible to take advantage of the time dependent gelling property of the silicate and colloidal silica solutions by using these gels as slow-release mechanisms for the treatment chemicals. This requires the understanding of the processes and parameters that control the flow and gelation of these solutions to predict their behavior after they are injected in groundwater.

The methodology presented here can be seen as an initial step in modeling the complex flow behavior of engineered silicate solutions. We provided a basic approach for simulating a rapid change of fluid viscosity due to gelation of an injected solute. The simulation results compared well to the laboratory experiments. The model simulated the key features of the gelation process

by increasing the viscosity over time with a user-defined rate. Moreover, triggering of the gelation was designed to depend on the concentration. In the simulations, we also show the ability to describe different solutes with a limited number of parameters.

In addition to engineered silicate solutions, other base materials were also tested to develop PG solutions that could provide cost-effective options for treating dissolved DNAPL plumes in groundwater. Among the available materials, chitosan is not chemically compatible with MnO_4^-. Aluminosilicates are compatible, but not miscible with MnO_4^-. When dilute acid solutions were not used, silicate solutions did not show delayed gelling property. Colloidal silica shows great potential as a material for the construction of SRP-Gs due to the control of gelation times that was evidenced in batch tests as well as the asymptotic release that was observed during flow-through tests conducted in porous media. Extended gelation lag times of up to 3 days were achieved. Dilution of SRP-Gs as a result of ionic strength and silica concentration constituted a key constraint on both gelation and release kinetics. Dense SRP-G solutions sink through the pores and form a pool, gelating and releasing MnO_4^- into the over-riding groundwater flow. Release from SRP-G gels emplaced in porous media was observed to last up to 3 days and was characterized by initial rapid, short-term release that was followed by a longer, attenuated asymptotic release phase. The mass flux tended to approach values that were near the desired mass flux (~ 850 $\mu g\ min^{-1}$) and can likely be further reduced by increasing the silica concentration. Increasing the silica concentration may also extend the duration of MnO_4^- release from the emplaced SRP-G.

Finally, geopolymers are low cost $KMnO_4$ compatible materials that can be used as slow-release solids. Cylindrical geopolymers with $KMnO_4$ concentrations up to 0.6 g/cm^3 were prepared. 1-D column release tests showed that MnO_4^- concentrations were initially high but decreased gradually through time. Slow-release solids with high $KMnO_4$ concentrations got exhausted after about 18 days. MnO_4^- release was controlled by anomalous diffusion and not by Fickian diffusion.

6.2. Implications for future research

Further laboratory experiments needed to acquire parameters required for numerical modeling of the gelation process of the silicate solutions. Additionally, the degradation of the gel and a coherent parameterization might be of interest. Finally, an experimental or numerical application on a larger scale (e.g. larger flow tank or field-scale) including a distinct heterogeneous setup (i.e. lenses) is a logical next step to provide insight into the present processes.

The gelation lag time of the silica and colloidal silica solutions and the slow release capacity of the gels need to be increased for a better performance as slow release solids. This requires further laboratory experimentation.

The conditions in the flow tank experiments were clearly not like the real world conditions. Natural oxidant demand (NOD) of the groundwater matrix in aquifers affects the rate and extent of degradation of chlorinated ethylenes at low concentrations because it represents the consumption of permanganate in reactions that are unrelated to oxidation of target contaminants (Siegrist et al., 2001). NOD increases the amount of oxidant required to eliminate the target contaminants. In addition to NOD, there are many environmental factors that could affect both the applicability and the effectiveness of the SRP-G method. Among such factors temperature, pH, ionic

composition, TDS can affect the formation of SRP-G and thus alter the effectiveness of the slow release process. A further study which investigates the impact of such parameters on the applicability and the effectiveness of the SRP-G formulation is therefore required so that site specific SRP-G formulations can be applied.

CO_2, MnO_2, Cl^- are among the products of the target organic contaminant (e.g. TEC) oxidation. It is well known that the MnO_2 precipitation can reduce the permeability of the subsurface and the introduction of a less-permeable grout could locally stop the groundwater flow which causes diversion of the groundwater flow. However, further laboratory experiments are required to investigate how the injection of SRP-G, MnO_2 precipitation and other oxidation products CO_2 and Cl^- impact the efficacy of the SRP-G and impact the groundwater flow.

The process that controls the permanganate release from the SRP-G to groundwater is diffusion. Detailed laboratory experiments are required to determine the expected life of the SRP-G at different conditions. Depending on the size of the target area, the estimated costs of deployment and replenishment can change. Nevertheless, a cost analysis for injection of a unit volume of SRP-G can be a subject of future research.

7. Literature Cited

Abdel-Hamid, M.I., Khairou, K.S. and Hassan, R.M., 2003. Kinetics and mechanism of permanganate oxidation of pectin polysaccharide in acid perchlorate media. Eur. Polym. J. 39, 381-387.

Abichou, T., Benson, C.H. and Edil, T.B., 2002. Micro-structure and hydraulic conductivity of simulated sand-bentonite mixtures. Clays and Clay Minerals, 50, 5, 537-545.

Acker, E., 1970. The characterization of acid-set silica hydrosols, hydrogels, and dried gel. Journal of Colloid and Interface Science 32.

Advanced Cement Technologies, 2013. Metakaolin physical and chemical properties –standard. URL: www.metakaolin.com

Ahmed, G.A.W., Khairou, K.S. and Hassan, R.M., 2003. Kinetics and mechanism of oxidation of chitosan polysaccharide by permanganate ion in aqueous perchlorate solutions. J. Chem. Res., 182-183.

Allen, L.H. and Matjevic, E., 1969. Stability of colloidal silica: effect of simple electrolytes. Journal of Colloid and Interface Science, 31, 287-296

ASTM D445 - 12, 2006. Standard Test Method for Kinematic Viscosity of Transparent and Opaque Liquids (and Calculation of Dynamic Viscosity). ASTM International doi:10.1520/D0445-12.

ASTM D446 - 12, 2008. Standard Speci_cations and operating Instructions for glass Capillary Kinematic Viscometers. ASTM International doi:10.1520/D0446-12.

Aulenta, F., Canosa, A., Leccese, M., Papini, M.P., Majone, M. and Viotti, P, 2007. Field study of in situ anaerobic bioremediation of a chlorinated solvent source zone. Industrial & Engineering Chemistry Research, v. 46, p. 6812-6819.

Baker, R., 1987. Controlled release of biologically active agents, A Wiley-Interscience Publication, John Wiley & Sons, Inc. ISBN 0-471-83724-5, 279 p.

Baird, C. and Cann, M, 2008. Environmental Chemistry: Fourth Edition. W.H. Freeman and Company, New York, NY.

Bear, J., 1972. Dynamics of Fluids in Porous Media. Elsevier, New York.

Bear, J., 1979. Hydraulics of groundwater. McGraw-Hill series in water resources and environmental engineering, McGraw-Hill International Book Co.

Beinhorn, M., Dietrich, P. and Kolditz, O., 2005. 3-D numerical evaluation of density effects on tracer tests. Journal of Contaminant Hydrology 81, 89-105. doi:10.1016/j.jconhyd.2005.08.001.

Berens, A.R. and Hopfenberg, H.B., 1978. Diffusion and relaxation in glassy polymer powders: 2. Separation of diffusion and relaxation parameters. Polymer 19, 489-496.

Blankenship, A., 2002. Catalytic Effect of Trace Excess Water on the Rate of Gel Shrinkage. Technical Report. Grace Columbia, Davison Catalysis Research.

Carman, P.C., 1940. Constitution of colloidal silica. Transactions of the Faraday Society, v. 36, p. 964-973.

Christensen, M.D., Kambhu A. and Comfort, S.D., 2012. Using slow-release permanganate candles to remove TCE from a low permeable aquifer at a former landfill. Chemosphere 89, 680-687.

Crank, J., 1975. The mathematics of diffusion. 2nd ed. Oxford University Press, GB, ISBN 0198533446.

Criado, M., Fernández-Jiménez, A., De la Torre, A.G., Aranda, M.A.G. and Palomo, A., 2007, An XRD study of the effect of the SiO_2/Na_2O ratio on the alkali activation of fly ash. Cement and Concrete Research, 37, 671-679.

Davidovits, J.,1991. Geopolymers Inorganic polymeric new materials, J. Thermal Analysis, 37, 1633-1656.

Davidovits, J., 2002, 30 years of successes and failures in geopolymer applications, Market trends and potential breakthroughs, In: Geopolymer 2002 Conference, Saint-Quentin (France), Melbourne (Australia): Geopolymer Institute.

Davidovits, J., 2008. Geopolymer Chemistry and Applications. Institut Géopolymère, Saint-Quentin, France.

Dimas, D., Giannopoulou, I. and Panias, D., 2009. Polymerization in sodium silicate solutions: a fundamental process in geopolymerization technology, J Material Sci, 44, 3719-3730.

Frisch, H.L., 1980. Sorption and transport in glassy polymers – a review. Polym. Eng. Sci. 20, 1, 2-13.

Gallagher, P. and Finsterle, S., 2004. Physical and numerical model of colloidal silica injection for passive site stabilization. Vadose Zone Journal , 917-925.

Gallagher, P.M., Pamuka, A. and Abdoun, T., 2007a. Stabilization of liquefiable soils using colloidal silica grout. J. Mat. Civil Eng. 19, 33-40.

Gallagher, P.M., Conlee, C.T. and Rollins, K.M., 2007b. Full-scale field testing of colloidal silica grouting for mitigation of liquefaction risk. Journal of Geotechnical and Geoenvironmental Engineering, v. 133, p. 186-196.

Gallagher, P.M. and Lin, Y., 2009. Colloidal silica transport through liquefiable porous media. J. Geotech. Geoenviron. Eng. 135, 1702-1712.

Giannopoulou, I. and Panias, D., 2010, Hydrolytic stability of sodium silicate gels in the presence of aluminium, J. Mater. Sci., 45, 5370-5377.

Good, W.R., 1976. Diffusion of water soluble drugs from initially dry hydrogels, in Polymeric delivery systems, in: Kostelnik, R. (Ed.), Gordon and Breach, New York, 139.

Goode, D.J., 1996. Direct Simulation of Groundwater Age. Water Resources Research 32, 289-296. doi:10.1029/95WR03401.

Grinsted, R.A., Clark, L. and Koenig, J.L., 1992. Study of cyclic sorption-desorption into poly(methymethacrylate) rods using NMR imaging, Macromolecules, 25, 1235-1241.

Gulrez, S.H., Al-Assaf, S. and Phillips, G.O., 2011. Hydrogels: Methods of preparation, characterization and applications, in: Progress in molecular and environmental bioengineering From analysis and modeling to technology applications, In Tech Publisher, Rijeka, Croatia. pp. 117-150.

Hamdine, M., Heuzey, M.C. and Begin, A., 2005. Effect of organic and inorganic acids on concentrated chitosan solutions and gels. Int. J. Biol. Macromol. 37, 134-142.

Heah, C.Y., Kamarudin, H., Mustafa Al Bakri, A.M., Bnhussain, M., Luqman, M., Khairul Nizar, I., Ruzaidi, C.M. and Liew, Y.M., 2012, Study on solids-to-liquid and alkaline activator ratios on kaolin-based geopolymers, Construction and Building Materials, 35, 912-922.

Huang, K.C., Hoag, G.E., Chheda, P., Woody, B.A. and Dobbs, G.M., 1999. Kinetic study of Oxidation of Trichloroethylene by Potassium Permanganate. Env. Eng. Sci. 16, 4, 265-274.

Huang, K.C., Hoag, G.E., Chheda, P., Woody, B.A. and Dobbs, G.M., 2001. Oxidation of chlorinated ethenes by potassium permanganate: A kinetics study. J. Hazard. Mat. 87, 155–169.

Ibaraki, M., 1998. A robust and efficient numerical model for analyses of density-dependent flow in porous media. Journal of Contaminant Hydrology 34, 235-246. doi:10.1016/S0169-7722(98)00092-8.

Ibaraki, M., Schwartz, F.W. and Swartz, C.H., 2000. Modelling instability development in layered systems. J. Contam. Hydrol. 42, 337–352.

Ibaraki, M. and Schwartz, F.W., 2001. Influence of natural heterogeneity on the efficiency of chemical foods in source zones, Groundwater 39(5), 660–666.

Iler, R.K., 1979. Chemistry of Silica: Solubility, Polymerization, Colloid and Surface Properties. John Wiley and Sons Inc., New York, NY.

Johannsen, K., 2003. On the validity of the Boussinesq approximation for the Elder problem. Computational Geosciences .

Johannsen, K., Oswald, S., Held, R. and Kinzelbach, W., 2006. Numerical simulation of three-dimensional saltwater freshwater fingering instabilities observed in a porous medium. Advances in Water Resources 29, 1690-1704. doi:10.1016/j.advwatres.2005.12.008.

Kalbacher, T., Delfs, J.O., Shao, H., Wang, W., Walther, M., Samaniego, L., Schneider, C., Kumar, R., Musolff, A., Centler, F., Sun, F., Hildebrandt, A., Liedl, R., Borchardt, D., Krebs, P. and Kolditz, O., 2011. The IWASToolBox: Software coupling for an integrated water resources management. Environmental Earth Sciences doi:10.1007/s12665-011-1270-y.

Kao, C.M, Huang, K.D, Wang, J.Y, Chen, T.Y. and Chien, H.Y., 2008. Application of potassium permanganate as an oxidant for in situ oxidation of trichloroethylene-contaminated groundwater: a laboratory and kinetic study. J. Hazard. Mater. 153, 919-27.

Karol, R.H., 2003. Chemical Grouting and Soil Stabilization. Marcel Dekker, Inc., Ney York.

Khairou, K.S., 2001. Spectrophotometric evidence for the formation of short-lived Mn(VI) as transient species intermediate during the permanganate oxidation of chitin and chitosan polysaccharides in alkaline solutions. Spectrosc. Lett. 34, 721-728.

Khale, D. and Chaudhary, R., 2007. Mechanism of geopolymerization and factors influencing its development: a review. J. Mater. Sci., 42, 729-746.

Kim, C., 2000. Controlled release dosage form design. Technomic Publishing Company, Inc., Pa, USA, ISBN 1566768101.

Kinzelbach, W., 1988. The random walk method in pollutant transport simulation, in: Groundwater flow and quality modelling. doi:10.1007/978-94-009-2889-3_15.

Kolditz, O., Ratke, R., Diersch, H.J.G. and Zielke, W., 1998. Coupled groundwater flow and transport: 1. Verification of variable density flow and transport models. Advances in Water Resources 21, 27{46. doi:10.1016/S0309-1708(96)00034-6.

Kolditz, O., Bauer, S., Bilke, L., Böttcher, N., Delfs, J.O., Fischer, T., Görke, U.J., Kalbacher, T., Kosakowski, G., McDermott, C.I., Park, C.H., Radu, F., Rink, K., Shao, H., Shao, H.B., Sun, F., Sun, Y.Y., Singh, A.K., Taron, J., Walther, M., Wang, W., Watanabe, N., Wu, Y., Xie, M., Xu, W. and Zehner, B., 2012a. OpenGeoSys: an open-source initiative for numerical simulation of thermo-hydro-mechanical/chemical (THM/C) processes in porous media. Environmental Earth Sciences. doi:10.1007/s12665-012-1546-x.

Kolditz, O., Görke, U.J., Shao, H. and Wang, W., 2012b. Thermo-Hydro-Mechanical-Chemical Processes in Porous Media: Benchmarks and Examples (Lecture Notes in Computational Science and Engineering), Springer.

Kong, D.L.Y., Sanjayan, J.G. and Sagoe-Crentsil, K., 2007. Comparative performance of geopolymers made with metakaolin and fly ash after exposure to elevated temperatures. Cement and Concrete Research, 37, 1583-1589.

Korsmeyer, R.W. and Peppas, N.A., 1981. Effect of the morphology of hydrophilic polymeric matrices on the diffusion and release of water soluble drugs, J. Membrane Science, 9, 211-227.

Korsmeyer, R.W., Gumy, R., Doelker, E., Buri, P. and Peppas, N.A., 1983. Mechanisms of solute release from porous hydrophilic polymers. Int. J. Pharm. 15, 25-35.

Langer, R., 1980, Polymeric delivery systems for controlled drug release, Chem Eng Commun, 6, 1-48.

Larian, M.G., and Mann, C.A., 1936. Drying gel zeolites. Ind.. Eng. Chem. 28, 196-200.

Launer, H.F., 1932. The kinetics of the reaction between potassium permanganate and oxalic acid. J. Am. Chem. Soc. 54, 2597-2610.

Lee, E.S., Seol, Y., Fang, Y.C. and Schwartz, F.W., 2003. Destruction efficiencies and dynamics of reaction fronts associated with the permanganate oxidation of trichloroethylene. Environ. Sci. Technol. 37, 2540-2546.

Lee, E.S. and Schwartz, F.W., 2007a. Characteristics and applications of controlled-release $KMnO_4$ for groundwater remediation. Chemosphere 66, 2058-66. doi:10.1016/j.chemosphere.2006.09.093.

Lee, E.S. and Schwartz, F.W., 2007b. Characterization and optimization of long-term controlled release system for groundwater remediation: A generalized modeling approach. Chemosphere 69, 247-253.

Lee, E.S., Woo, N.C., Schwartz, F.W., Lee, B.S., Lee, K.C., Woo, M.H., Kim, J.H. and Kim, H.K., 2008a. Characterization of controlled-release $KMnO_4$ (CRP) barrier system for groundwater remediation: a pilot-scale flow-tank study. Chemosphere 71, 902-10. doi:10.1016/j.chemosphere.2007.11.037.

Lee, E.S., Liu, G., Schwartz, F.W., Kim, Y. and Ibaraki, M., 2008b. Model-based evaluation of controlled release systems in the remediation of dissolved plumes in groundwater. Chemosphere 72, 165-173.

Lee, E.S., Olson, P., Gupta, N., Solpuker, U., Schwartz, F.W. and Kim, Y., 2013. Permanganate gel (PG) for groundwater remediation: Compatibility, gelation, and release characteristics, under review, Chemosphere.

Li, X.D. and Schwartz, F.W., 2004. DNAPL remediation with in situ chemical oxidation using potassium permanganate: II Increasing removal efficiency by dissolving Mn oxide precipitates. J. Contam. Hydrol. 68, 269-288.

Lidwell, O.M. and Bell, R.P., 1935. The Reaction between Potassium Permanganate and Oxalic Acid. J. Chem. Soc. 1303-1305.

McDade J.M., McGuire, T.M. and Newell, C.J., 2005. Analysis of DNAPL Source-Depletion Costs at 36 Field Sites. Remediation Journal, 15, 2, 9-18.

McNeil, J., Oldenborger, G. and Schincariol, R., 2006. Quantitative imaging of contaminant distributions in heterogeneous porous media laboratory experiments. Journal of Contaminant Hydrology 84, 36-54. doi:10.1016/j.jconhyd.2005.12.005.

Murdoch, L., Slack, W., Siegrist, R., Vesper, S. and Meiggs, T., 1997. Advanced Hydraulic Fracturing Methods to Create In Situ Reactive Barriers, in: International Containment Technology Conference, St. Petersburg, Florida.

Olson, P., 2011. Novel Remediation Schemes for Groundwater and Urban Runoff. unpublished MS thesis, Ohio University, 27-30.

Oswald, S. and Kinzelbach, W., 2004. Three-dimensional physical benchmark experiments to test variable-density flow models. Journal of Hydrology 290, 22-42. doi:10.1016/j.jhydrol.2003.11.037.

Park, C.H., 2004. Saltwater intrusion in coastal aquifers. Ph.D. thesis. Georgia Institute of Technology.

Park, C.H. and Aral, M., 2008. Saltwater intrusion hydrodynamics in a tidal aquifer. Journal of Hydrologic Engineering 13, 863.

Peppas, N.A., 1985. Analysis of Fickian and non-Fickian drug release from polymers. Pharm. Acta Helv. 60, 4, 110-11.

Persoff, P., Apps, J., Moridis, G. and Whang, J. M., 1999. Effect of dilution and contaminants on sand grouted with colloidal silica. Journal of Geotechnical and Geoenvironmental Engineering, 125, 461-469.

Pothamkury, U. R. and Barbosa-Canovas, G. V., 1995. Fundamental aspects of controlled release in foods. Trends in Food Science & Technology, 6, 397-406.

PQ Corporation, 2003. Soluble Silicates in Geotechnical Grouting Applications. Valley Forge PA.

PQ Corporation, 2012. Industrial Chemicals Division. PQ Sodium silicates. URL: www.pqcorp.com.

PQ Corporation, 2011. Soluble Silicates in Geotechnical Grouting Applications. PQ Corporation Literature Bulletin 52–53, URL: www.pqcorp.com.

Ritger, P.L and Peppas, N.A., 1987. A simple equation for description of solute release I.Fickian and non-Fickian release from non-swellable devices in the form of slabs, spheres, cylinders or discs. J. Control Release 5, 23-36.

Ross, C., Murdoch, L., Freedman, D. and Siegrist, R., 2005. Characteristics of potassium permanganate encapsulated in polymer. Journal of Environ. Eng. 131, 1203-1211.

Rowles, M. and O'Connor, B., 2003, Chemical optimisation of the compressive strength of aluminosilicate geopolymers synthesised by sodium silicate activation of metakaolinite, J Materials Chemistry, 13, 1161-1165.

Schincariol, R.A. and Schwartz, F.W., 1990. An experimental investigation of variable density flow and mixing in homogeneous and heterogeneous media. Water Resources Research 26, 2317. doi:10.1029/WR026i010p02317.

Schincariol, R. A., Herderick, E. E. and Schwartz, F. W., 1993. On the application of image analysis to determine the concentration distributions in laboratory experiments. J. Contam. Hydrol. 12, 197–215.

Schincariol, R. A., Schwartz, F. W. and Mendoza, C. A., 1994. On the generation of instabilities in variable density flow. Water Resour. Res. 30(4), 913–927.

Schincariol, R., 1998. Dispersive mixing dynamics of dense miscible plumes: natural perturbation initiation by local-scale heterogeneities. J. Contam. Hydrol., 34, 247-271.

Schnarr, M., Truax, C., Farquhar, G., Hood, E., Gonullu, T. and Stickney, B., 1998. Laboratory and controlled field experiments using potassium permanganate to remediate trichloroethylene and perchloroethylene DNAPLs in porous media. J. Contam. Hydrol. 29, 205-224.

Schwartz, F.W. and Zhang, H., 2003. Fundamentals of Ground Water, John Wiley, New York.

Siegrist, R., Lowe, K., Murdoch, L., Case, T. and Pickering, D., 1999. In situ oxidation by fracture emplaced reactive solids. Journal of Environ. Eng.125, 429-440.

Siegrist, R. L., Urynowicz, M. A., West, O. A., Crimi, M. L. and Lowe, K. S., 2001. Principles

and Practices of In Situ Chemical Oxidation Using Permanganate. Battelle Press, Columbus, Ohio, USA.
Sinclair, G.W. and Peppas, N.A., 1984. Analysis of non-Fickian transport in polymers using simplified exponential expressions. J. Membr. Sci. 17, 329-331.
Smith, M.M., Silva, J.A.K., Munakata-Marr, J., and McCray, J.E., 2008. Compatibility of polymers and chemical oxidants for enhanced groundwater remediation. Environ. Sci. Technol. 42, 9296-9301.
Solpuker, U., Hawkins, J., Schincariol, R., Ibaraki, M. and Schwartz, F.W., 2012. Harnessing the complex behavior of ultra-dense and viscous treatment fluids as a strategy for aquifer remediation, in: Models Repositories of Knowledge, Leipzig.
Stewart, R., 1965. Oxidation in Organic Chemistry, Academic Press, New York.
Subhash B., 1990. Zeolite Catalysis: Principles and Applications, CRC Press, Inc., Boca Raton, Florida.
Swartz, C.H. and Schwartz, F.W., 1998. An experimental study of mixing and instability development in variable-density systems. Journal of Contaminant Hydrology 34, 169-189. doi:10.1016/S0169-7722(98)00088-6.
Todd, B., Willhite, G. and Green, D., 1993. Mathematical model of in-situ gelation of polyacrylamide by a redox process. SPE reservoir engineering, 51-58.
Urynowicz, M.A., 2000, Reaction kinetics and mass transfer during in situ oxidation of dissolved and DNAPL trichloroethene with permanganate. Ph.D. dissertation, Environmental Science & Engineering Division, Colorado School of Mines, May.
U.S. Department of Health and Human Services, 1997. Toxicological Profile for Trichloroethylene. Atlanta GA.
U.S. EPA. 1987. Trichloroethylene: Health Advisory. Office of Drinking Water. United States Environmental Protection Agency, Washington, D.C.
Vanýsek, P., 2014. Ionic conductivity and diffusion at infinite dilution. Handbook of Chemistry and Chemistry (editor in chief Haynes, W.M.) 94th edition, 5, 77-79.
Voss, C.I., 1984. A finite-element simulation model for saturated unsaturated, fluid-density-dependent ground-water flow with energy transport or chemically-reactive single-species solute transport. Technical Report. U.S. Geological Survey Water Resources Investigations Report 84-4369. Tyndall.
Walther, M., Delfs, J.O., Grundmann, J., Kolditz, O. and Liedl, R., 2012. Saltwater intrusion modeling: Verification and application to an agricultural coastal arid region in Oman. Journal of Computational and Applied Mathematics 236, 4798-4809. doi:10.1016/j.cam.2012.02.008.
Ward, D. S., Reeves M. J. and Duda, L. E., 1984. Verification and validation of the SWIFT model. In: Scientific Basis for Nuclear Waste Management VII, Materials Research Society Symposia Proceedings (ed. by G. L. McVay), 26, 927–933. Mater. Res. Soc. North-Holland, New York, USA.
Yan, Y. E. and Schwartz, F. W., 1998. Oxidation of chlorinated solvents by permanganate. Proc. Intern. Conf. on Remediation of Chlorinated and Recalcitrant Compunds, Batelle Press, Columbus, Ohio, 403-408.
Yan, Y. E. and Schwartz, F. W., 1999. Oxidative degradation and kinetics of chlorinated ethylenes by potassium permanganate. J. Contam. Hydrol. 37, 343–365.
Yan, Y.E. and Schwartz, F.W., 2000. Kinetics and mechanisms for TCE oxidation by permanganate. Environ. Sci. Technol. 34, 2535-2541.

Yang, X., Zhu, W. and Yang, Q., 2007. The Viscosity Properties of Sodium Silicate Solutions. Journal of Solution Chemistry 37, 73-83. doi:10.1007/s10953-007-9214-6.
Zhang, H. and Schwartz, F.W., 2000. Simulating the in situ oxidative treatment of chlorinated ethylenes by potassium permanganate.Water Resour. Res. 36, 3031-3042.

Appendix A Supporting data

The following supporting digital data is given as a summary of the three experiments mentioned in the report as a means to aid in the interpretation of the experiments.

-Appendix A-1 includes 15 time snapshots (1-15.JPEG) and the video (Experiment #1.wmv) of the first experiment.

-Appendix A-2 includes 20 time snapshots (1-20.JPEG) and the video (Experiment #2.wmv) of the second experiment.

-Appendix A-3 includes 12 time snapshots (1-12.JPEG) and the video (Experiment #3.wmv) of the third experiment.

Appendix B Publications

-Walther, M., Solpuker, U., Böttcher, N., Kolditz,O., Liedl, R., and Schwartz, F.W., 2013, Description and Verification of a Novel Flow and Transport Model for Silicate-Gel Emplacement, J Contam Hydrol, accepted DOI: 10.1016/j.jconhyd.2013.10.007

-Solpuker, U, Cotter, Z, Kim, Y and Schwartz, F.W., 2013, $KMnO_4$ doped geopolymers as controlled-release materials for reactive barriers in groundwater remediation, submitted to Chemosphere.

-Lee ES, Olson PR, Gupta N, Solpuker U, Schwartz FW, Kim Y., 2013, Permanganate gel (PG) for groundwater remediation: Compatibility, gelation, and release characteristics. Chemosphere, 1577-4. doi: 10.1016/j.chemosphere.2013.11.008.

-Solpuker, U., Hawkins, J., Schincariol, R., Ibaraki, M., & Schwartz, F. W, 2012, Harnessing the complex behavior of ultra-dense and viscous treatment fluids as a strategy for aquifer remediation, Models – Repositories of Knowledge, ModelCare2011, Leipzig, Germany.